Control-oriented Modeling and Multirate Feedback Control in Laser Powder Bed Fusion Additive Manufacturing

Dan Wang

A dissertation
submitted in partial fulfillment of the
requirements for the degree of

Doctor of Philosophy

University of Washington

2020

Reading Committee:

Xu Chen, Chair

Santosh Devasia

Ramulu Mamidala

Program Authorized to Offer Degree:
Mechanical Engineering

University of Washington

Abstract

Control-oriented Modeling and Multirate Feedback Control in Laser Powder Bed Fusion Additive Manufacturing

Dan Wang

Chair of the Supervisory Committee:
Assistant Professor Xu Chen
Department of Mechanical Engineering

A high-precision additive manufacturing process, laser powder bed fusion (LPBF) has enabled unmatched agile manufacturing of a wide range of products from engine components to medical implants. While finite element modeling and closed-loop control have been identified key for predicting and engineering part qualities in LPBF, existing results in each realm are developed in opposite computational architectures wildly different in time scale.

This dissertation builds a first-instance closed-loop simulation framework by integrating high-fidelity finite element modeling with feedback controls originally developed for general mechatronics systems. By utilizing the output signals (e.g., melt pool width) retrieved from the finite element model (FEM) to directly update the control signals (e.g., laser power) sent to the model, the proposed closed-loop framework enables testing the limits of advanced controls in LPBF and surveying the parameter space fully to generate more predictable part qualities.

Along the course of formulating the framework, we build and refine an FEM of the thermal response in LPBF and verify the FEM by comparing its results with experimental and analytical solutions. Thereafter, we use the FEM to understand the melt-pool evolution induced by the thermomechanical interactions in LPBF. In addition, we build a new Hammerstein mixed-fidelity model to capture more of the complex spatiotemporal thermal dynamics.

Under the architecture of the closed-loop simulation, we discuss general loop-shaping algorithms and specifically develop a multirate fractional-order repetitive control (RC) algorithm that addresses an intrinsic RC limitation when the exogenous signal frequency cannot divide the sampling frequency of the sensor. We also investigate the model inversion techniques—an important piece of the loop-shaping control—and build an H_∞-based optimal inversion that attains model accuracy at the frequency regions of interest while constraining noise amplification elsewhere to guarantee system

robustness. Besides, we analyze spectral properties of the closed-loop signals under sample-data control and show that the single-rate high-gain feedback cannot reject disturbances near and beyond the Nyquist frequency. From there, we provide a case study on applying an RC algorithm to greatly attenuate periodic thermal variations in LPBF.

TABLE OF CONTENTS

LIST OF FIGURES

Figure Number Page

LIST OF TABLES

Table Number Page

NOMENCLATURE

AM: additive manufacturing

DOB: disturbance observer

FEM: finite element model

FFT: fast Fourier transform

FTF: fundamental transfer function

GCD: greatest common divisor

HDD: hard disk drive

ILC: iterative learning control

LCM: least common multiple

LMD: laser metal deposition

LPBF: laser powder bed fusion

NMP: nonminimum-phase

PDE: partial differential equation

PFG: performance frequency gain

PID: proportional–integral–derivative

RC: repetitive control

RFG: robust frequency gain

YK: Youla-Kucera

ZOH: zero-order-hold

ACKNOWLEDGMENTS

Along my Ph.D. journey, I have received a lot of support, help, and guidance.

My deepest appreciation first goes to my advisor Prof. Xu Chen for the extraordinary guidance, support, and feedback on this dissertation. With every commented manuscript, every sharp research insight, and every timely discussion comes my sincerest gratitude. I have learned from Prof. Chen not only about profound knowledge of control theory but also about systematic research methodology, positive attitude, and perseverance. There were countless moments when I felt the icing of wisdom be sprinkled on my head. I am also extremely grateful to Prof. Chen for always being supportive and believing in me. Besides, a lot of thanks to Prof. Chen and Prof. Zhanzha Jia for hosting the group gatherings and making me feel welcome, comfy, and at home.

I am greatly thankful to have Prof. Santosh Devasia, Prof. Ramulu Mamidala, and Prof. Behçet Açikmeşe as my committee members. I truly appreciate the time and effort they have put into this dissertation. I have learned a lot from Prof. Santosh Devasi and Prof. Ramulu Mamidala about their studies and research attitude. Prof. Behçet Açikmeşe gave me great lectures about nonlinear control. I am so thankful for Prof. Xinyu Zhao's insight in building the finite element model. My sincere thanks also go to Prof. Jiong Tang, Prof. Horea Ilies, and Prof. Chengyu Cao for their great suggestions on this dissertation. I would like to acknowledge the National Science Foundation and the UTC Institute for Advanced Systems Engineering for generously supporting this study.

I would also like to thank the current members of the Mechatronics, Automation, and Control Systems Laboratory: Tianyu Jiang, Hui Xiao, Feifei Yang, and Hanah Choice. Many thanks to Tianyu for the experimental demonstration and to Hui for sharing the career development plan. Special thanks to Tianyu and Hui for all the help in life and for always having my back. Thanks to Feifei for updating the lab website for me. And thanks to Hanah for the power of positive emotions. Also, I'm enjoying mentoring and working with MS student Ruiwei Sui and UG student John Shim. They are wonderful.

Last but not least, I would like to thank my parents Meiyan Sun and Mingzhang Wang

for all the endless unconditional love and for teaching me to be brave and strong. Also, enormous thanks to my dearest friends Holly Xu, Maggie Wang, Dr. Jing Zhang, Prof. Zhanzhan Jia, Prof. Xin Xue, Leo Liu, Roger Fang, Dr. Xiao Ren, and Dr. Yuan Yuan and my sister Xiaohuan Lv for lifting my heart, lightening up my life, caring for me, and always being there for me. Without them, I would not have made it through my doctoral degree.

DEDICATION

To my family and friends

Chapter 1

INTRODUCTION

Distinct from conventional subtractive machining, additive manufacturing (AM) builds a part directly from its digital model by joining materials layer by layer. In particular, applying high-precision lasers as the energy source, laser powder bed fusion (LPBF) AM has enabled unprecedented fabrication of complex parts from polymeric and metallic powder materials. LPBF builds a typical part from many thousands of thin layers. Within each layer (Fig. 1.1), the laser beam is reflected by mirrors driven by periodic or near-periodic reference signals in a beam deflection mechanism (e.g., a dual-axis galvo scanner) to follow trajectories predefined by the part geometry in a "slicing" process (see, e.g., Fig. 1.2). After the printing of one layer, a recoater will spread a new thin layer of powder over the just-fused layer, and then another cycle will begin.

Despite the advantages and emerging applications, broader adoption of the LPBF technology remains challenged by insufficient reliability and in-process variations. These variations are induced by, for example, uncertain laser-material interactions, environmental vibrations, powder recycling, imperfect interactions of mechanical components, and complex thermal histories of materials [1–3]. Current researches employ finite element modeling and feedback controls to understand the energy-deposition mechanisms and to regulate the in-process variations in LPBF. For instance, [4–7] adopt finite element modeling to investigate how various scan patterns, scan speeds, number of lasers, overhanging structures, and underlying physics affect the thermal fields of the powder bed, the geometries of the melt pool, and the mechanical properties of the printed parts. Specially, [8] brings up the idea of building digital twins of AM machines by integrating various high-fidelity multiphysics models. Existing feedback control strategies usually implement low-order system models obtained from system identification techniques, such as [2,9,10] in LPBF and [11–13] in laser metal deposition (LMD), an AM technology analogous to LPBF. A nonlinear memoryless submodel [12, 14] and a spatial-domain Hammerstein model [13] are further built in LMD to cover more complicated process dynamics. From there, PID control, sliding mode control, predictive control, and iterative learning control (ILC) have proved their efficiencies in improving the dimensional accuracy of the printed parts in LPBF [2, 9, 15, 16] and in LMD [11, 14, 17–20].

Although finite element model (FEM) and feedback control have been identified key for predicting and engineering part qualities in LPBF, existing results in each realm are developed

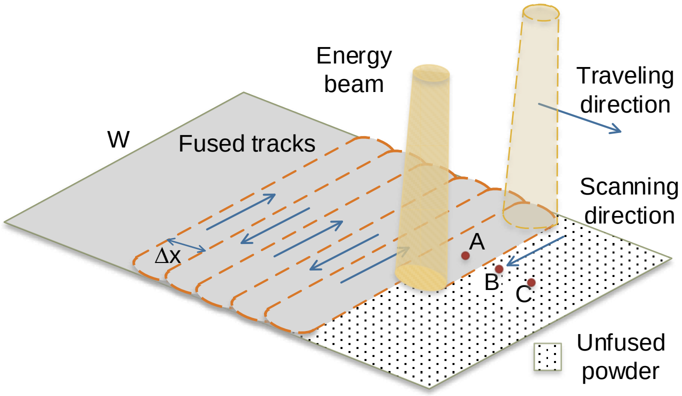

Figure 1.1: Schematic of in-layer LPBF processes.

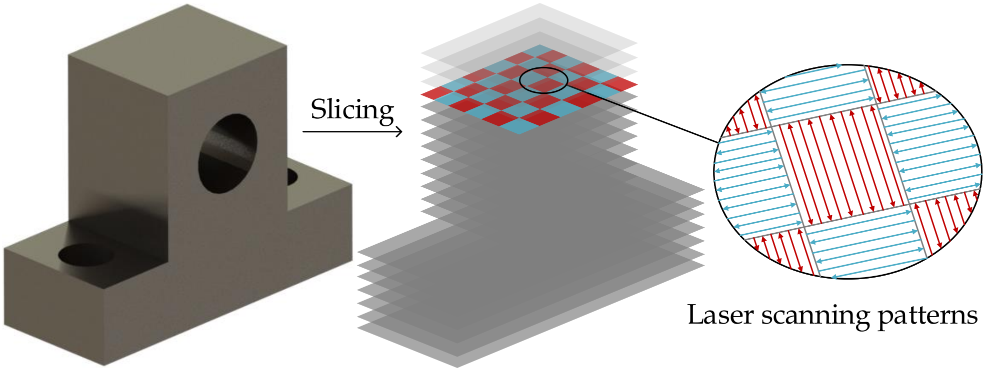

Figure 1.2: Schematic of laser scanning patterns in LPBF. The example shows the most common "island" pattern in LPBF of metallic objects.

in separate computational architectures due to their different time scales. Feedback controls are implemented in real time, while FEM takes hours or even days to simulate the printing of a few layers that finishes in seconds in reality. If we can integrate FEM with feedback controls directly in a closed loop, however, we can 1) combine aforementioned knowledge from each realm, 2) test the limit of advanced control in LPBF, 3) survey the parameter space fully to generate more predictable part qualities, and 4) quickly design controllers and update parameters for novel materials and printer settings. These benefits are more prominent when the experiments are costly and time-consuming.

In pursuit of the above benefits, this dissertation builds, in the first instance to our best knowledge, a closed-loop high-fidelity simulation framework that leverages modern architectures of finite-element-modeling tools and the power of data processing and advanced controls. In particular, we build a bidirectional architecture so that the output signals (e.g., melt pool width or peak temperature) retrieved from the FEM can be utilized to directly update the FEM process parameters (e.g., laser power or scan speed) in external control toolboxes (e.g., MATLAB). In this way, we design an interface that enables implementing and testing out feedback control strategies for LPBF thermal processes. Along the course of formulating the framework, we explore control-oriented modeling of the LPBF process and advanced feedback control algorithms to mitigate in-process variations and improve part quality in LPBF.

In control-oriented modeling, we build and refine an FEM of the temperature response in LPBF, which serves as an essential component of the proposed closed-loop simulation. Implementing the developed FEM, we investigate the periodic melt pool evolution and identify a nonlinear physics-based Hammerstein model to represent the complex thermal dynamics in LPBF. In the other essential component of the closed-loop simulation, namely, feedback control, starting from a loop-shaping control method, this dissertation focuses on its RC implementation. In particular, we propose a multirate fractional-order RC to tackle disturbances with fractional-order periods. Furthermore, we explore model inversion that is fundamental to the loop-shaping control method and build an H_∞-based inversion to automatically search for an optimal inverse model that fits selective frequency regions. Besides, we look into the spectral analysis in sample-data loop-shaping control to uncover the fundamental limitation of single-rate high-gain control near and beyond the Nyquist frequency.

Major Contributions of This Dissertation

Closed-loop Simulation Integrating FEM with Feedback Control

One major contribution of the dissertation is building a first-instance closed-loop simulation framework by integrating high-fidelity finite element modeling with feedback controls originally developed for general mechatronics systems. We build and refine the FEM of the temperature response in LPBF, which serves as an essential component of the proposed closed-loop simulation. We verify the FEM by comparing its results with experimental and analytical solutions and then use the FEM to understand the melt-pool evolution induced by the in- and cross-layer thermomechanical interactions. From there, we build a repetitive control (RC) algorithm to attenuate variations of the melt pool width.

New Hammerstein Mixed-fidelity Modeling

Control-oriented modeling is a fundamental tool for predicting and engineering part qualities in LPBF. Using the FEM data, we identify a novel surrogate system model from the laser power to the melt pool width. Linking a linearized model with a memoryless nonlinear submodel, we develop a physics-based Hammerstein mixed-fidelity model that captures the complex spatiotemporal thermomechanical dynamics. We verify the accuracy of the Hammerstein model using the FEM and prove that the linearized model is only a representation of the Hammerstein model around the equilibrium point. Along the way, we conduct the stability and robustness analyses and formalize the Hammerstein model to facilitate the subsequent control designs.

Loop-shaping Control

Many servo systems including LPBF systems require micro/nano level positioning accuracy. This requirement sets a number of challenges from the viewpoint of sensing, actuation, and control algorithms. This dissertation considers control algorithms for precision positioning. We examine how to use prior knowledge about the parameterization of control structure and the disturbance spectrum to the design of control algorithms. An outer-loop inverse-based Youla-Kucera (YK) parameterization is built in the dissertation. The presented algorithms are evaluated on a precision galvo scanner system in LPBF.

Fractional-order Repetitive control

This dissertation discusses fractional-order RC to advance the quality of periodic energy deposition in LPBF. It addresses an intrinsic RC limitation when the exogenous signal frequency cannot divide the sampling frequency of the sensor, e.g., in imaging-based control of fast laser-material interaction in LPBF. Three RC designs are proposed to address such fractional-order repetitive processes. In particular, a new multirate RC provides superior performance gains by generating high-gain control exactly at the fundamental and harmonic frequencies of exogenous signals. Experimentation on the galvo laser scanner validates effectiveness of the designs.

H_∞-based Model Inversion

Stably inverting a dynamic system model is fundamental to subsequent servo designs, such as the RC design. Current inversion techniques have provided effective model matching for feedforward controls. However, when the inverse models are to be implemented in feedback systems, additional considerations are demanded for assuring causality, robustness, and stability under closed-loop constraints. To bridge the gap between accurate model approximations and robust feedback performances, this dissertation provides a new treatment of unstable zeros in inverse design. We provide first an intuitive pole-zero-map-based inverse tuning to verify the basic principle of the unstable-zero treatment. From there, for general nonminimum-phase and unstable systems, we propose an H_∞-based optimal inversion algorithm that can attain model accuracy at the frequency regions of interest while constraining noise amplification elsewhere to guarantee system robustness. Along the way, we also provide a modern review of model inversion techniques. The proposed algorithm is validated on motion control systems and complex high-order systems.

Multirate Spectral Analysis near and Beyond Nyquist Frequency

A fundamental challenge in sampled-data control arises when a continuous-time plant is subject to disturbances that possess significant frequency components beyond the Nyquist frequency of the feedback sensor. Such intrinsic difficulties create formidable barriers for fast high-performance controls in modern and emerging technologies such as LPBF AM and vision servo, where the update speed of sensors is low compared to the dynamics of the plant. This dissertation analyzes spectral properties of closed-loop signals under such scenarios, with a focus on mechatronic systems. We propose a spectral analysis method that provides new understanding of the time- and frequency-domain sampled-data performance. Along the course of uncovering spectral details in such beyond-Nyquist controls, we also report a fundamental understanding on the infeasibility of single-rate high-gain feedback to reject disturbances not only beyond but also below the Nyquist frequency. New metrics and tools are then proposed to systematically quantify the limit of performance. Validation and practical implications of the limitations are provided with experimental case studies performed on the galvo scanner platform.

The rest of the dissertation is structured as follows:

In Part I, we build the architecture of the proposed closed-loop high-fidelity simulation with bidirectional communication between FEM and feedback control in LPBF. We look into one essential component of the proposed closed-loop simulation, that is, the control-oriented modeling. In Chapter 3, we build and refine the FEM of the temperature response in LPBF. Besides, from underlying physics, we develop in Chapter 4 a new Hammerstein mixed-fidelity model that captures more of the complicated spatiotemporal thermomechanical dynamics in LPBF.

In Part II, we investigate model-based multirate feedback control algorithms, which serves as the other key component of the proposed closed-loop simulation. In detail, Chapter 5 introduces the general loop-shaping control methodologies. Chapter 6 builds a specific multirate fractional-order RC algorithm. Chapter 7 looks into the model inversion techniques—an important piece of the loop-shaping control. Chapter 8 analyzes spectral properties of the closed-loop signals under multirate sample-data control.

Under the infrastructure of the closed-loop simulation, integrating control-oriented modeling with feedback control, in Part III, Chapter 9 provides a case study on applying RC to regulate the periodic thermal interactions in LPBF. Chapter 10 concludes this dissertation and discusses potential future work.

Part I

CLOSED-LOOP HIGH-FIDELITY SIMULATION AND CONTROL-ORIENTED MODELING

Chapter 2

ARCHITECTURE OF CLOSED-LOOP HIGH-FIDELITY SIMULATION

We propose in this chapter the main closed-loop simulation that integrates FEM with feedback controls directly in a closed loop. The key idea is to use the output signals (e.g., melt pool width) retrieved from the FEM to update through the controller the control signals (e.g., laser power) sent back to the FEM. The core of the FEM is the numerical simulation of a partial differential equation (PDE) of the general form:

$$f(x_1,\ldots,x_n;u,\frac{\partial u}{\partial x_1},\ldots,\frac{\partial u}{\partial x_n};\frac{\partial^2 u}{\partial x_1 \partial x_1},\ldots,\frac{\partial^2 u}{\partial x_1 \partial x_n};\ldots)=0,$$

where u is the output signal predicted by the FEM and $x_1,\ldots,x_n$ are the independent variables. Examples of PDEs in LPBF include the governing equations for heat transfer, thermal stress, and fluid flow; the output signals are hence the temperature, stress, and melt pool velocity, respectively [21,22]. On the other hand, in feedback control, an output signal is compared with a reference signal to generate an error signal, which is then filtered by a controller to produce a control signal. By reacting to the in-process change of the output signal, feedback control compensates for model inaccuracies and unmeasured disturbances.

Leveraging the power of FEM and feedback controls, we develop the closed-loop simulation algorithm and outline its workflow as follows:

1. Designing and initializing the FEM in an FEM software (e.g., COMSOL) and the controller in a control-oriented scripting programming environment (abbreviated as programming environment, e.g., MATLAB). For the focused closed-loop FEM in this dissertation, we set the computation time of the FEM as T_s, where T_s is the sampling time of the discrete-time feedback loop;

2. Building an interface to connect the FEM software with the programming environment. This interface enables simulating closed-loop controllers for FEM and taking advantage of the programming environment in preprocessing, model manipulation, statistical analysis, and post-processing;

3. Through the interface, the programming environment retrieves the output signal from the FEM software. Thereafter, the controller processes the output signal to get the new control signal, which is then sent back to the FEM. With the updated control signal, a new FEM computation begins;

4. Repeating step 3 until the whole simulation ends.

With the bidirectional architecture between the FEM and controller, the closed-loop simulation enables updating directly the control signals of the FEM, retrieving signals hard to reach by experiments, and surveying the parameter space fully before real LPBF experiments. Moreover, the proposed architecture is agnostic to the types of programming environment and FEM software, facilitating incorporating various control methods into different multiphysics simulations (e.g., heat transfer and fluid flow studies). As application examples, we choose COMSOL Multiphysics, MATLAB, and *LiveLink for MATLAB* to build the FEM, controller, and interface, respectively. We provide in this chapter the skeletons of an FEM of the thermal fields and a generic feedback control design. We will build the detailed FEM and controller in Chapter 3 and Part II, respectively.

1) The governing equation for the conduction heat flow in LPBF is

$$\rho c_p \frac{dT(x,y,z,t)}{dt} = \nabla \cdot (k \nabla T(x,y,z,t)) + q_s, \tag{2.1}$$

where k is the thermal conductivity, c_p the specific heat capacity, ρ the effective density, t the time, T the temperature, and q_s the rate of local internal energy generated per unit volume [23]. When no confusion would arise in the context, we abbreviate $T(x,y,z,t)$ to T in the rest of this dissertation.

The initial condition is defined by setting $T(x,y,z,0)$ as the ambient temperature T_0. When the substrate (Fig. 3.2) is designed to be large enough compared to the heat-affected zone, one boundary condition is established by assuming the bottom ($z = h$) of the substrate has no heat loss [4–6]: $-k\frac{\partial T}{\partial z}\Big|_{z=h} = 0$. A quantitative way to test and validate the size of the substrate is that from the FEM results, the bottom of the substrate should maintain the temperature of T_0. The other boundary condition is established by considering the top surface ($z = 0$) of the powder bed with input heat flux, convection heat loss, and radiation heat loss:

$$-k\frac{\partial T}{\partial z}\Big|_{z=0} = -Q + h_c(T - T_0) + \varepsilon\sigma_B(T^4 - T_0^4), \tag{2.2}$$

where Q is the input heat flux, h_c the convection heat transfer coefficient, ε the emissivity, and σ_B the Stefan-Boltzmann constant. Here, we assume Q has a Gaussian laser beam profile: $Q \approx \frac{2q}{\pi R^2} \mathrm{e}^{-\frac{2r^2}{R^2}}$, where q is the laser power, R the effective laser beam radius, and r the radial distance from a certain point to the center of the laser spot. From the temperature distribution predicted by the FEM, melt pool width can be further calculated, as will be elaborated in Chapter 3. From here on, we select melt pool width w as the output signal and laser power q as the control signal for the subsequent feedback control design.

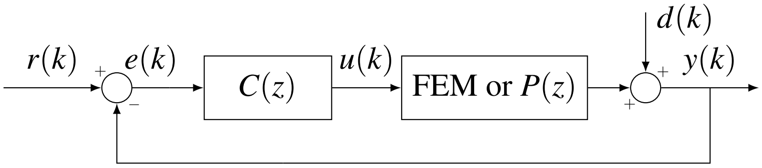

Figure 2.1: Block diagram of general feedback control.

2) A generic feedback system consists of a plant $P(z)$ and a controller $C(z)$ (Fig. 2.1). In the closed-loop simulation, $P(z)$ is the plant model identified from the FEM simulation. The signal $r(k)$ represents the system reference, which here is a desired melt pool width; $u(k)$ represents the control signal, which here is the laser power; $y(k)$ represents the system output, which here is the melt pool width as calculated from FEM-predicted temperature fields; $d(k)$ represents the input disturbance, which here is the in-process melt-pool-width variations.

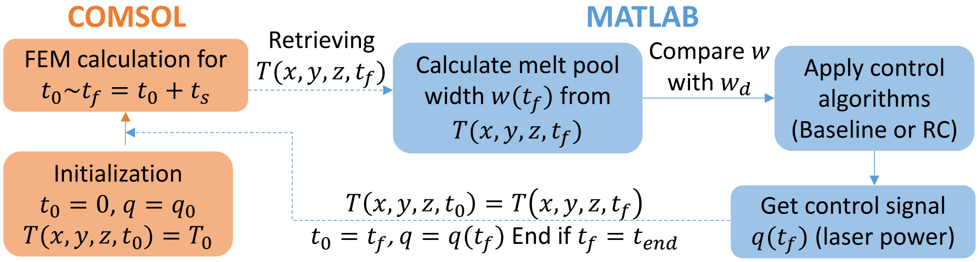

Figure 2.2: Schematic of the proposed closed-loop simulation.

Fig. 2.2 demonstrates the operating procedures of the closed-loop simulation architecture, taking as examples the FEM of the LPBF thermal process and generic feedback control. We design and initialize the FEM in COMSOL while programming in MATLAB the main file of the architecture that includes the interface establishment, the controller design, and the recursive calls for COMSOL. First, we initialize the FEM by setting the start time t_0 as 0, the laser power q as an initial value q_0, and the temperature distribution $T(x, y, z, t_0)$ as the ambient temperature T_0. The computation time of the FEM is set as one time step from t_0 to $t_f = t_0 + T_s$. After the initialization, MATLAB will call COMSOL to start the FEM computation. After retrieving the FEM-predicted temperature distribution $T(x, y, z, t_f)$, the main file in MATLAB calculates the melt pool width $w(t_f)$ from $T(x, y, z, t_f)$ and, based on the control algorithms, processes $w(t_f)$ and its historical values to obtain the control signal $q(t_f)$. After that, the FEM is updated by assigning the iterative variables t_0 as t_f, $T(x, y, z, t_0)$ as $T(x, y, z, t_f)$, and the laser power as $q(t_f)$. After passing all closed-loop computed information, MATLAB will call COMSOL to start the FEM computation with the updated variables, and a new cycle will begin. The closed-loop simulation will stop when t_f reaches to the whole simulation time t_{end} ($\gg t_f$ in general).

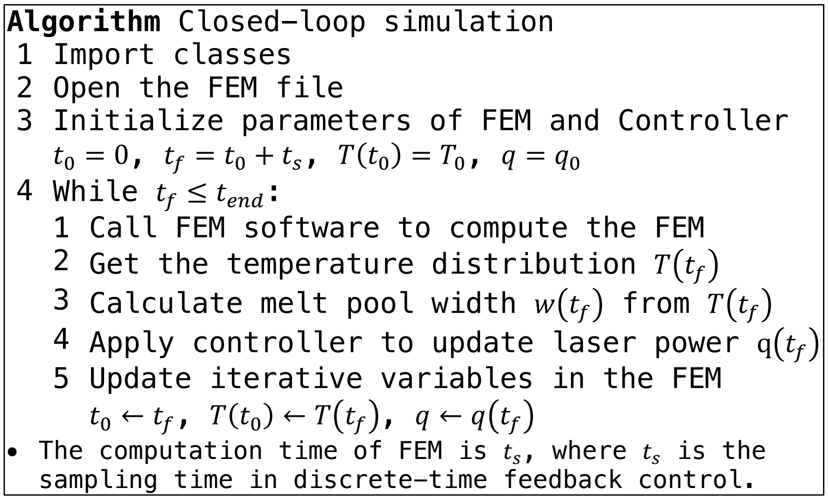

```
Algorithm Closed-loop simulation
1 Import classes
2 Open the FEM file
3 Initialize parameters of FEM and Controller
  $t_0 = 0$, $t_f = t_0 + t_s$, $T(t_0) = T_0$, $q = q_0$
4 While $t_f \leq t_{end}$:
  1 Call FEM software to compute the FEM
  2 Get the temperature distribution $T(t_f)$
  3 Calculate melt pool width $w(t_f)$ from $T(t_f)$
  4 Apply controller to update laser power $q(t_f)$
  5 Update iterative variables in the FEM
    $t_0 \leftarrow t_f$, $T(t_0) \leftarrow T(t_f)$, $q \leftarrow q(t_f)$
• The computation time of FEM is $t_s$, where $t_s$ is the
  sampling time in discrete-time feedback control.
```

Figure 2.3: Pseudocode of the proposed closed-loop simulation algorithm.

We provide in Fig. 2.3 the pseudocode of the main file in the closed-loop simulation algorithm. After importing the necessary classes for building the FEM, controller, and interface, the algorithm opens the FEM file and initializes the parameters of the FEM and controller. Inside the *while* loop, the main file calls the FEM software to compute the FEM simulation and then retrieves the predicted temperature distribution $T(x, y, z, t_f)$. Based on $T(x, y, z, t_f)$, the algorithm calculates the melt pool width $w(t_f)$ and thereafter processes $w(t_f)$ and its historical values through the controller to get the new laser power. At last, the algorithm updates the iterative variables of the start time, the initial temperature, and the laser power to get prepared for a new iteration. Appendix A.1 provides the main MATLAB commands used in the closed-loop simulation.

The proposed closed-loop simulation establishes not only a bidirectional communication between FEM software and programming environment but also an interface specifically for the purpose of simulating feedback controllers in FEM. The built architecture will benefit and guide experiments by validating beforehand the effectiveness of the servo designs. Next we will present the detailed FEM and controller designs in Chapter 3 and Part II, respectively.

Chapter 3

FINITE ELEMENT MODELING

In this chapter, we use the COMSOL Multiphysics 5.3a software to build and refine the FEM of the temperature response in LPBF, which serves as an essential component of the proposed closed-loop simulation. We verify the FEM configuration by comparing the numerical results with the experimental and analytical solutions and then use the verified FEM to investigate the periodic in- and cross-layer thermal interactions. The FEM developed in this dissertation considers conduction, latent heat of fusion, surface convection, and surface radiation. The principal objective of this dissertation is not to create a new high-fidelity FEM at microscopic fluid flow level but to develop and test the closed-loop simulation architecture. Therefore, we omit the effects of evaporation, fluid flow, and Marangoni force for easier testing in the general control community. The FEM built in this dissertation is intended as one application example of the proposed architecture between FEM and controller. However, the physics of complex melt flow (e.g., Marangoni and surface tension effects) can be readily added to increase the model accuracy and provide more microscopic details of the melt pool that are beyond the focus of this dissertation.

3.1 Governing Physics and Model Development

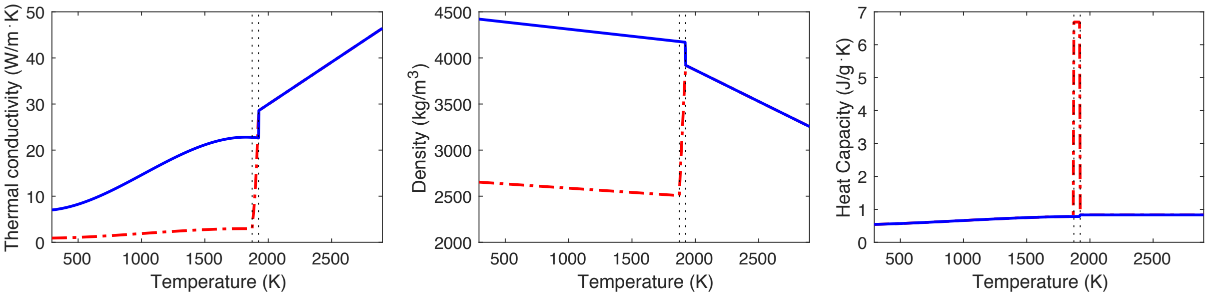

Figure 3.1: Temperature-dependent thermal properties of Ti6Al4V. Solid line: solid and liquid materials. Dash-dotted line: powder material. The two vertical dotted lines respectively indicate T_{sol} and T_m.

Table 3.1: Parameters of the FEM. Note that the laser spot diameter of 70 μm is for model verification in Section 3.2.

Parameters	Value
Size of powder bed	$5\,\mathrm{mm} \times 10\,\mathrm{mm} \times 50\,\mu\mathrm{m}$
Size of substrate	$5\,\mathrm{mm} \times 10\,\mathrm{mm} \times 2\,\mathrm{mm}$
Powder/substrate material	Ti6Al4V
Laser power q	60 W or varying [24]
Scan speed u_x	100 mm/s [24]
Track length L	5 mm
Laser spot diameter $2R$	220 μm (or 70 μm [24])
Ambient/initial temp.	293.15 K
Initial porosity ϕ_0	0.4 [4,25]
Emissivity	0.35 [4]
Powder bed absorptance	0.25 [4]
Time step T_s	0.5 ms
Melting point T_m	1923.15 K [26]
Solidus temperature T_{sol}	1873 K [26]
Latent heat of fusion L_f	295 kJ/kg [26]
Convection h.t. coeff. h_c	$12.7\,\mathrm{W/(m^2 \cdot K)}$ [4]
k, c_p, and ρ	See Fig. 3.1 [4,25,27,28]
Shielding gas type	Argon [24]
Shielding gas temperature	293.15 K [4]
Shielding gas flow rate	$167\,\mathrm{cm^3/K}$ [4]

We have elaborated the governing equation, initial condition, and boundary conditions in Chapter 2. For the temperature-dependent thermal properties in (2.1), we adopt k, c_p, and ρ in [4,25] for the solid and liquid materials, as shown in Fig. 3.1. We generate the thermal properties of the powder material from those of the solid material by considering the powder-bed porosity ϕ [27,28]:

$$k_{powder} = k_{solid}(1-\phi)^4 \quad \text{and} \quad \rho_{powder} = \rho_{solid}(1-\phi),$$

where ϕ is expressed as

$$\phi(T) = \begin{cases} \phi_0 & T_0 < T \le T_{sol} \\ \frac{\phi_0}{T_{sol}-T_m}(T - T_m) & T_{sol} < T < T_m \\ 0 & T \ge T_m \end{cases},$$

with ϕ_0 denoting the initial porosity. Here, the heat capacity is assumed to be the same for the powder and solid materials [27]. Especially, we account for the latent heat of fusion L_f by introducing the effective heat capacity to the powder material [29]:

$$c_{p,eff}(T) = \begin{cases} c_{p1}(T) & T_0 < T \le T_{sol} \\ \frac{L_f}{T_m-T_{sol}} + \frac{c_{p1}(T_{sol})+c_{p2}(T_m)}{2} & T_{sol} < T < T_m \\ c_{p2}(T) & T \ge T_m \end{cases}, \tag{3.1}$$

where T_0 is the ambient temperature, T_{sol} the solidus temperature, T_m the melting point, c_{p1} the heat capacity of the powder, and c_{p2} the heat capacity of the liquid. Table 3.1 lists the process parameters used in this dissertation unless otherwise specified. To justify the parameter values, we introduce here the volumetric energy density E_v, which is a key factor in the LPBF process and directly impacts on the properties of as-built parts. E_v is defined as: $E_v = P/(vth)$, where P is the laser power, v the laser scan speed, t the layer thickness, and h the hatch spacing [30]. During the in-layer multitrack printing (Sections 3.3.2), $P = 60\,\mathrm{W}$, $v = 100\,\mathrm{mm/s}$, $t = 50\,\mu\mathrm{m}$, and $h = 60\,\mu\mathrm{m}$, which gives $E_v = 200\,\mathrm{J/mm^3}$. This volumetric energy density is, for example, in the ranges of $71 \sim 373\,\mathrm{J/mm^3}$ as studied in [31] and $15 \sim 240\,\mathrm{J/mm^3}$ as in [32].

Fig. 3.2a shows the bidirectional scan scheme used in this study and the whole build with a substrate and a thin layer of powder bed. Here, we use a selective meshing scheme to balance model accuracy with computation time: a fine quad-and-swept mesh with a maximum element size of $60\,\mu\mathrm{m}$ is applied to the central powder bed region that directly interacts with the energy beam, whereas less fine tetrahedral mesh (3.5 mm) and triangular-and-swept mesh (2 mm) are applied to the substrate and the peripheral powder bed, respectively. Fig. 3.2b showcases a surface temperature distribution, where the isotherm of $T = T_m$ indicates the melt pool geometry.

From the FEM-predicted temperature distribution, Fig. 3.3 shows the pseudocode of how to calculate the melt pool width. The basic principle is to search around the position of the laser beam to find the maximum width of the melt pool bounded by T_m. The first step is to locate the position of the laser beam (x_{laser}, y_{laser}), as shown in Fig. 3.2b. Then we identify the points to traverse by testing and ensuring that the rectangle $2c_x \times 2c_y$ be inclusive of anticipated melt pool widths (Fig.

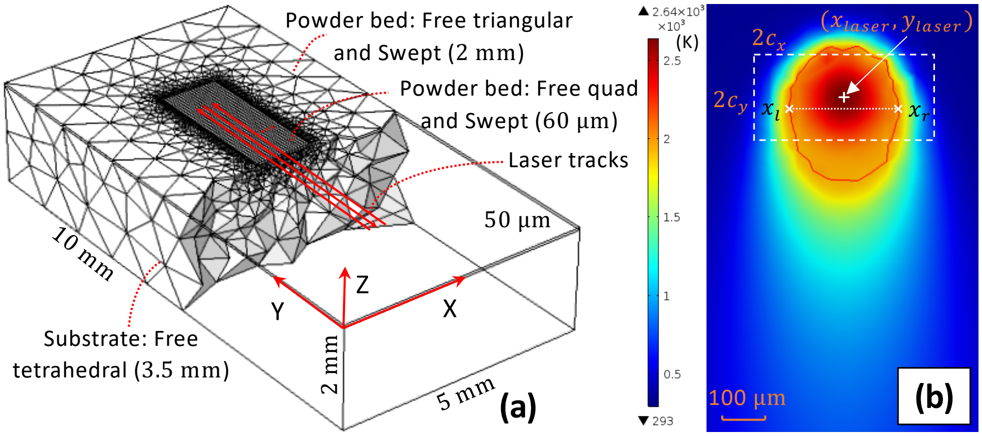

Figure 3.2: (a): a thin layer of powder bed and the substrate with selective meshing scheme. (b): surface temperature distribution at $t = 0.14\,\mathrm{s}$. The lined isotherm indicates $T = T_m$.

3.2b). A set X stores the x coordinates of these points with an increment Δx, and a set Y stores the y coordinates with Δy. For each y in Y, we search in X to find the left boundary x_l and right boundary x_r that have the temperature of T_m. A width w_y for a certain y is given by $x_r - x_l$. After going over all the points, we identify the melt pool width as the maximum w_y. In this study, we choose $\Delta x = \Delta y = 1\,\mu\mathrm{m}$, $c_x = 150\,\mu\mathrm{m}$, and $c_y = 100\,\mu\mathrm{m}$.

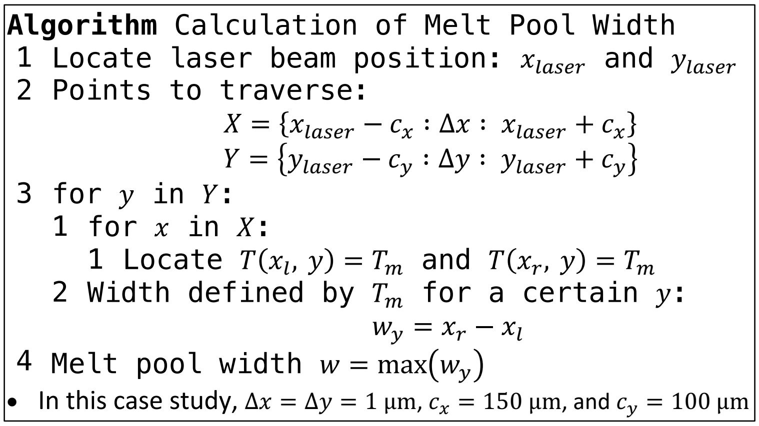

```
Algorithm Calculation of Melt Pool Width
 1 Locate laser beam position: $x_{laser}$ and $y_{laser}$
 2 Points to traverse:
                 $X = \{x_{laser} - c_x : \Delta x : x_{laser} + c_x\}$
                 $Y = \{y_{laser} - c_y : \Delta y : y_{laser} + c_y\}$
 3 for $y$ in $Y$:
    1 for $x$ in $X$:
       1 Locate $T(x_l, y) = T_m$ and $T(x_r, y) = T_m$
    2 Width defined by $T_m$ for a certain $y$:
                             $w_y = x_r - x_l$
 4 Melt pool width $w = \max(w_y)$
• In this case study, $\Delta x = \Delta y = 1$ µm, $c_x = 150$ µm, and $c_y = 100$ µm
```

Figure 3.3: Pseudocode for calculating the melt pool width.

3.2 Model Verification

Table 3.2: Melt pool widths from FEM and experimental results with a fixed laser power of 50 W and different scan speeds. Difference (Diff.)=FEM-Experiments (Exper.). Error=|FEM-Exper.|/FEM.

Scan speed	FEM(µm)	Exper. (µm)	Diff. (µm)	Error (%)
100 mm/s	182	165.7∼175.4	6.6∼16.3	3.6∼9.0
200 mm/s	152.6	140.7∼142.9	9.7∼11.9	6.4∼7.8
300 mm/s	132.6	120.7∼125.4	7.2∼11.9	5.4∼9.0

This section verifies the developed FEM by comparing the numerical melt pool widths with the experimental and analytical solutions. Table 3.2 first compares the melt pool widths obtained from the developed FEM with the experimental results in [24]. The laser power is fixed to be 50 W, the laser spot diameter is 70 µm, and the scan speed is 100, 200, or 300 mm/s. The FEM gives reasonable predictions of the melt pool widths with errors less than 10%.

Then we compare the numerical melt pool widths with the analytical solutions. When a moving point laser source is acting on a thick plate and the thermal properties of the plate are constant, the analytical solution of (2.1) in the steady state is the Rosenthal equation [23]:

$$T(\xi, y, z) - T_0 = \frac{q}{2\pi k r} \mathrm{e}^{-\frac{u_x(r+\xi)}{2\kappa}}, \tag{3.2}$$

where (ξ, y, z) is a coordinate system attached to the moving laser source, $r = \sqrt{\xi^2 + y^2 + z^2}$, and $\kappa = k/(\rho c_p)$. For comparison, we adapt the FEM to accommodate the assumptions of the Rosenthal equation, such as constant thermal properties ($k = 5$ W/(m· K), $c_p = 1.1$ J/(g· K), and $\rho = 4300\,\mathrm{kg/m^3}$) and point heat source. Fig. 3.4 compares the numerical and analytical solutions. From Fig. 3.4a, we can tell that the melt pool widths obtained from the FEM and the Rosenthal equation match well with each other under different combinations of scan speeds and laser powers. Also, as shown in Figs. 3.4b and 3.4c, after 27 samples, the numerical melt pool geometry reaches to the steady state and matches with the Rosenthal solution (the outline).

3.3 Periodic Thermal Interactions

We adopt the verified FEM in Section 3.1 to investigate the periodic LPBF thermal cycles and will then design a repetitive controller to regulate these cycles in Chapter 9.

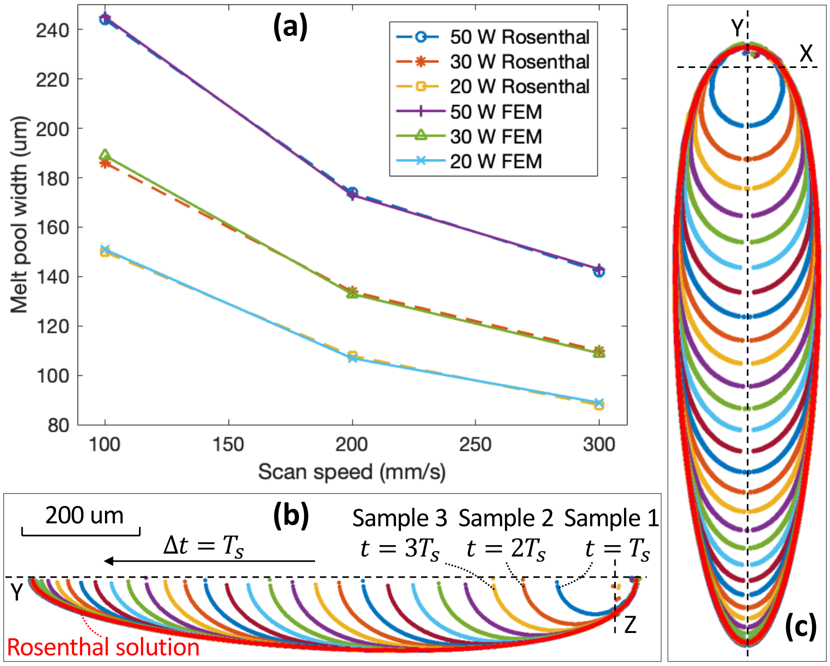

Figure 3.4: Melt pool widths from the FEM and analytical solutions. (b) and (c) share the same scale and legend.

3.3.1 Periodic Thermal Interactions: Hatch Spacing

We first examine how hatch spacing affects the melt pool variation, especially during the transition from the end of one track (named P1) to the start of the adjacent track to be sintered (P2). Here, hatch spacing is defined as the distance between two adjacent scan vectors and denoted as Δx in Fig. 1.1. When the hatch spacing (e.g., 47 µm in (a1)-(a4) of Fig. 3.5) is much less than half of the melt pool width (around the laser spot radius 110 µm), the laser spot at P2 will be centered inside the melt pool region of P1 and thus can take advantage of the accumulated heat, yielding a well-developed melt pool at 50.5 ms. When the hatch spacing (e.g., 100 µm in (b1)-(b4) of Fig. 3.5) is close to or larger than half of the melt pool width, the laser spot at P2 will be centered out of the melt pool region of P1, yielding a lower initial temperature at P2. Besides, since the laser is turned off during the transition, a larger hatch spacing (100 µm) gives a longer dwell time (1 ms) with the same scan speed (100 mm/s). Hence, previously fused tracks would have more time to cool down, which also yields a lower initial temperature at P2. Therefore, the melt pool evolves slower at P2, and two immature states show up at 550.5 ms and 551 ms, which will cause more porosity in the printed part.

To get consistent part quality in LPBF, a stable melt pool is desired during the transition. The immature melt pool states can be eliminated by decreasing the hatch spacing. However, there is a trade-off between melt pool stability and printing efficiency since simply shortening the hatch spacing increases printing time. Next we will study periodic melt pool variations that are intrinsic in the LPBF process and demand much more involved solutions, such as advanced control algorithms.

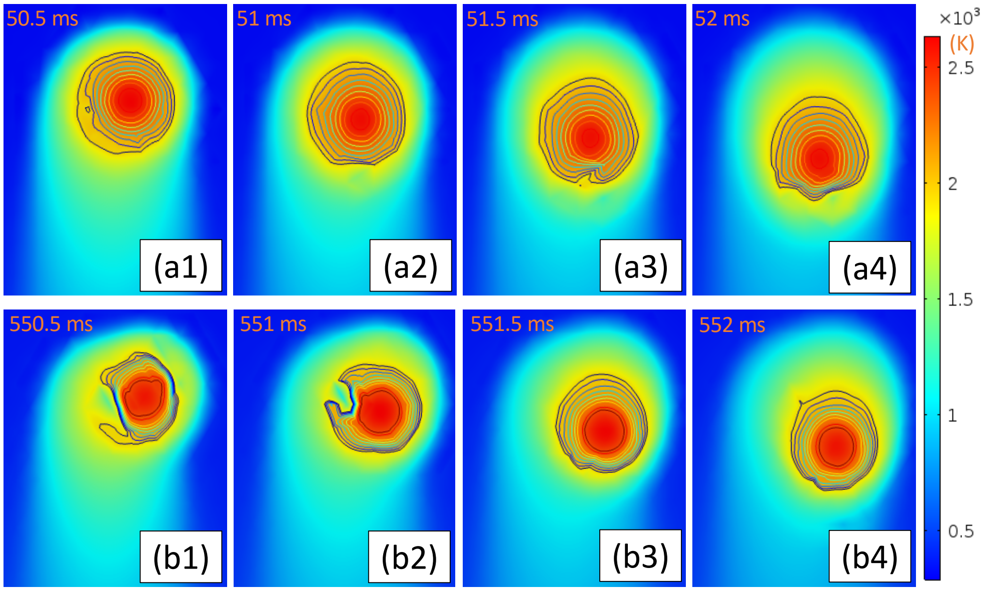

Figure 3.5: Melt pool variations at the start of the 2nd track with hatch spacing of 47 µm (i.e., dwell time of 0.47 ms) in (a1)-(a4) and the start of the 12th track with hatch spacing of 100 µm (i.e., dwell time of 1 ms) in (b1)-(b4).

3.3.2 Periodic Thermal Interactions: In-layer Effects

To investigate the in-layer thermal cycles, we bidirectionally print 10 tracks in the first layer with a hatch spacing of 60 µm (Fig. 3.2a). From Fig. 3.6a, we observe that the melt pool width changes over time and structurally deviates from the steady-state value 246 µm as extracted from the first track. Most importantly, the start of each track has larger melt pool widths than the rest of the track. This is because in bidirectional scanning, when the energy beam approaches the end of one track, the large latent heat does not have enough time to dissipate out before the next track starts. The resulting increased melt pool widths at the beginning of each track form a periodic disturbance with a repetitive spectrum in the frequency domain (Fig. 3.6b). The fundamental frequency f_0 of the disturbance is determined by the duration of scanning one track t_0, that is, $f_0 = 1/t_0 = u_x/L$, where

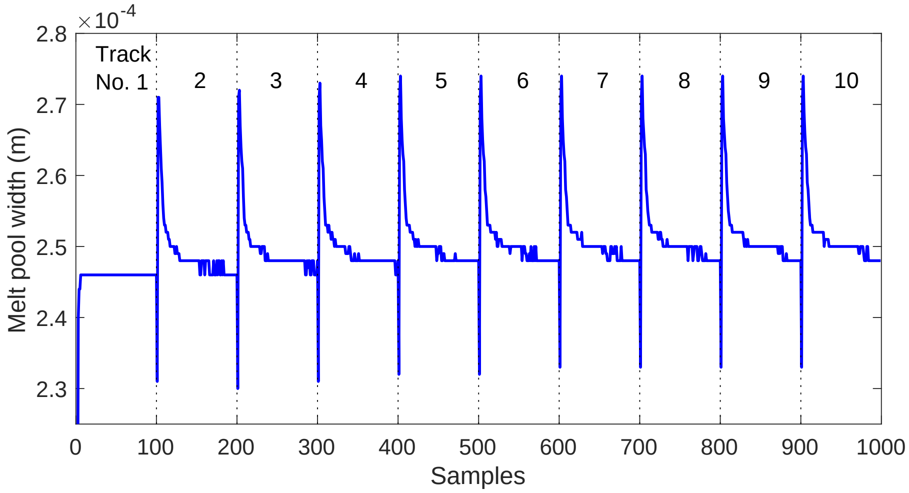

(a) Evolution of melt pool width (time-domain)

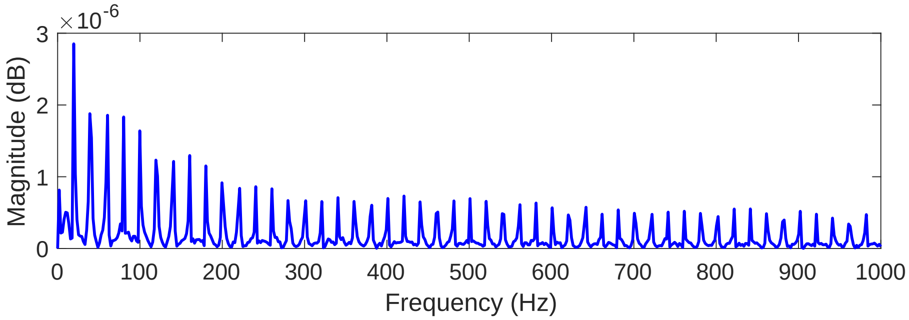

(b) FFT of melt-pool-width evolution (frequency-domain)

Figure 3.6: In-layer thermal disturbance with constant laser power.

u_x is the scan speed and L is the track length. In this example, $f_0 = 100/5 = 20\,\text{Hz}$, and frequency spikes at $nf_0\,(n \in \mathbb{Z}^+$, the set of positive integers) appear in the fast Fourier transform (FFT) of the disturbance.

The disturbance periodicity is closely related to the recurring laser scanning trajectories and the repetitive in-layer thermomechanical interactions. Besides the proof-of-concept bidirectional scan, other scan patterns yield repetitive disturbance components in a similar fashion (see, e.g., experimental results in [33]). To deal with these undesired repetitive spectra, we develop the closed-loop simulation in Chapter 2 to bring automatic control algorithms [1, 34] into FEM. More results and analyses will be elaborated in Part II.

3.3.3 Periodic Thermal Interactions: Combined In- and Cross-layer Effect

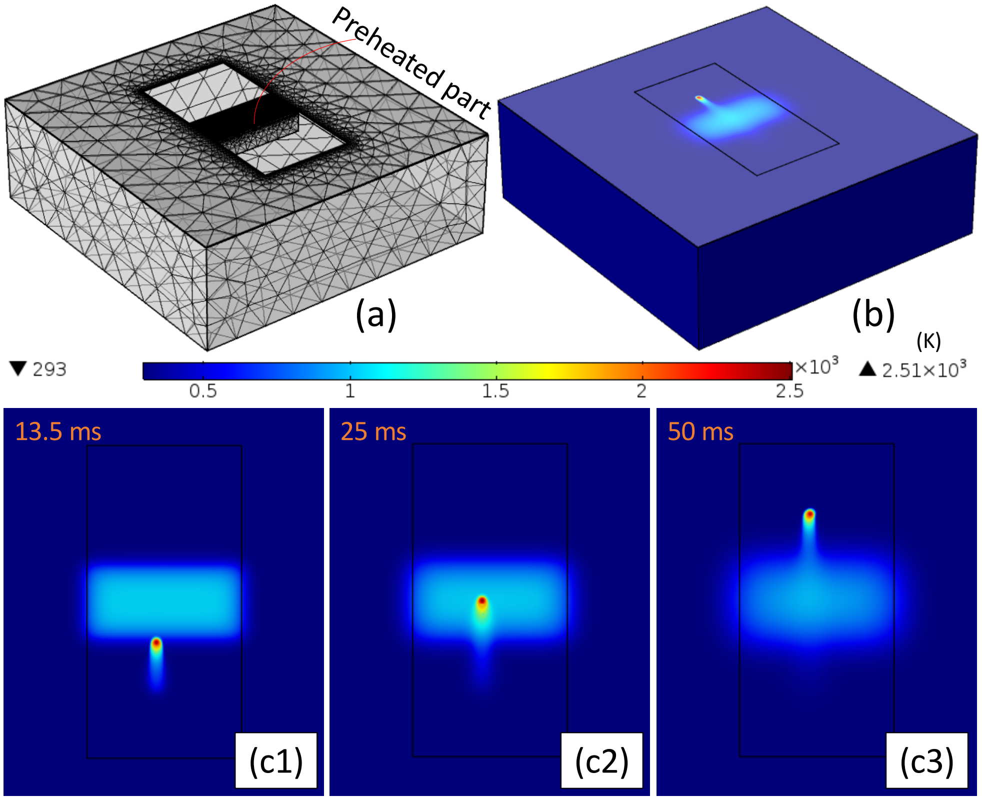

Figure 3.7: (a): mesh with added preheated part. (The thin layer of powder bed is hidden to unveil the added part.) (b): surface temperature distribution at $t = 49\,\mathrm{ms}$. (c1)-(c3): surface temperature distributions (top view) during the printing of the first track.

This section demonstrates the combined effect of periodic in- and cross-layer thermal interactions. As shown in Fig. 3.7, we put under the powder bed a Ti6Al4V part ($4.45 \times 1 \times 1\,\mathrm{mm}^3$) that is preheated to 1200 K [35]. Due to the high initial temperature of the added part, the powder on top of the part has a higher initial temperature than the powder elsewhere. The scan strategy is the same as that in Fig. 3.2a. Eight tracks are scanned bidirectionally with the hatch spacing of $50\,\mu\mathrm{m}$. The length of the laser track (5 mm) is greater than that of the added part (1 mm). This configuration imitates the printing process of parts with overhang structures, where the preheated Ti6Al4V part corresponds to the previously fused layers. As in Fig. 3.2, we also use the selective mesh scheme (Fig. 3.7a): triangular-and-swept ($72.6\,\mu\mathrm{m}$) for the central powder bed, triangular-and-swept (1.5 mm) for the peripheral powder bed, and free tetrahedra (2 mm) for the substrate and the added part.

In Fig. 3.7, plots (c1)-(c3) illustrate the top views of the surface temperature profiles during the first-track printing from 0 to 50 ms. When the laser is passing over the preheated powder at 25 ms, we get a larger melt pool width, compared to when the laser is approaching ($t = 13.5\,\mathrm{ms}$) or leaving ($t = 50\,\mathrm{ms}$) the preheated region. The larger melt pool width is generated due to the higher initial temperature of powder on top of the preheated part.

During the evolution of the melt pool width in Fig. 3.8a, at the beginning of each track, there is a large increase of the melt pool width caused by the in-layer thermal interaction, as explained in Section 3.3.2. Besides, as indicated by the arrows in Fig. 3.8a, larger melt pool widths appear every time the laser passes over the powder on top of the preheated part. These arrowed peaks caused by the cross-layer thermal interaction get smaller as the heat accumulated by the preheated part dissipates out (Tracks 7 and 8 in Fig. 3.8a). This phenomenon can also be seen from the blurrier border of the preheated region at $t = 50\,\mathrm{ms}$ in Fig. 3.7 (c3).

We have demonstrated that the periodic evolution of the melt pool width is a lumped output of the repetitive in- and cross-layer heat transfer dynamics. When comparing the frequency spectra in Figs. 3.6b and 3.8b, we can tell that the cross-layer thermal interaction changes the magnitudes of the spectral peaks but not the harmonic frequency values. These variations can thus be attenuated by the same feedback control algorithms, such as the RC algorithm to be introduced in Part II.

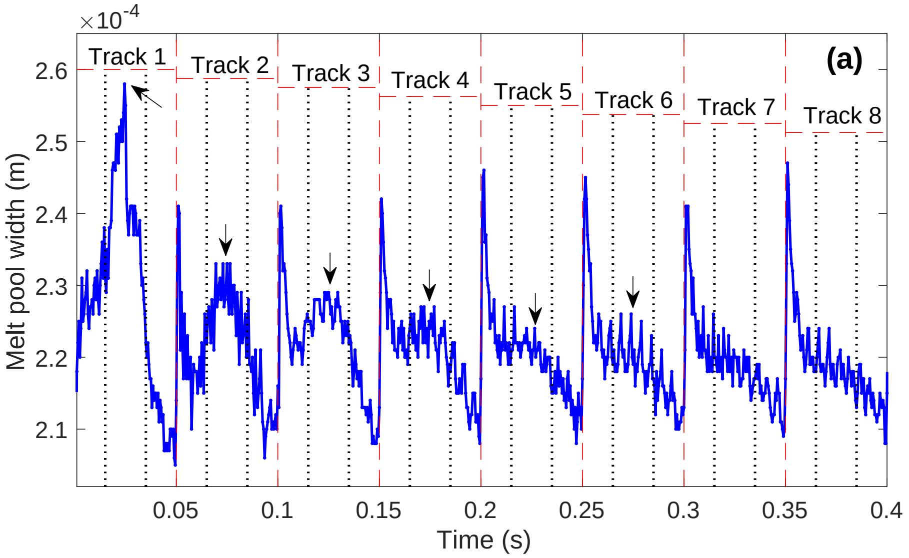

(a) Evolution of melt pool width (time-domain). An interval between two adjacent dashed lines indicates the printing of one track, whereas inside one track, the interval between two adjacent dotted lines denotes when the laser is passing over the preheated part.

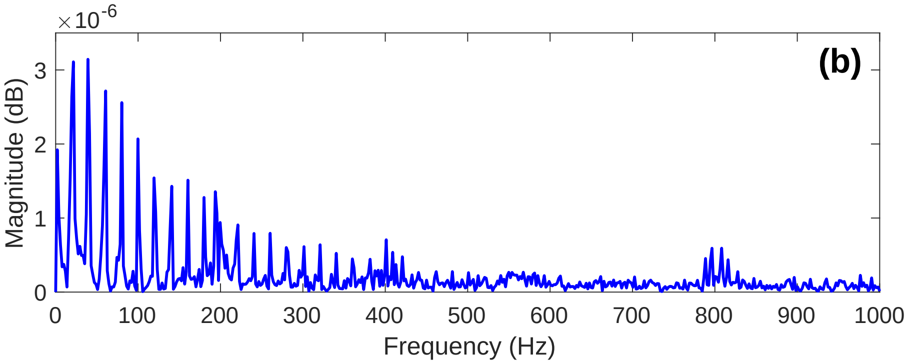

(b) FFT of melt-pool-width evolution (frequency-domain)

Figure 3.8: Combined in- and cross-layer thermal disturbance.

Chapter 4

NEW HAMMERSTEIN MIXED-FIDELITY MODELING

4.1 Introduction

Appropriate modeling of the sophisticated dynamic LPBF system plays a fundamental role in understanding and regulating the LPBF process and LPBF-related techniques such as the laser metal deposition (LMD). This chapter establishes a new modeling and understanding of LPBF by taking advantage of the FEM and control-oriented modeling. The FEM developed in Chapter 3 serves as a simulation platform to provide data for verifying and identifying parameters of the proposed modeling schemes. In the control-oriented modeling of LPBF, stepping beyond commonly used low-order system models [2, 9–13], this chapter develops a physics-based Hammerstein mixed-fidelity model that accommodates more of the convoluted spatiotemporal thermomechanical dynamics. The Hammerstein model is formulated by concatenating a memoryless nonlinear submodel derived from the Rosenthal equation to a linear model obtained from standard system identification techniques with laser power as the input and melt pool width as the output. We verify the accuracy of the Hammerstein model using the FEM and prove that the identified model is only a linear representation of the Hammerstein model around the equilibrium point. Along the way, we analyze the stability and robustness properties of the models and present a generic control scheme of the Hammerstein model.

In the remainder of this chapter, Section 4.2 identifies the linear plant model from the FEM. Section 4.3 derives the closed-form expressions of the steady-state melt pool width and furthermore develops and analyzes the main Hammerstein model.

4.2 Linear Model Around a Quasi-steady Equilibrium

From the FEM developed in Chapter 3, we identify the linear plant model as $P(s) = 0.001671/(s+1055)$ from laser power changes δq to melt pool width changes δw around the equilibrium point at $(q_0 = 60\,\mathrm{W}, w_0 = 248.41\,\mu\mathrm{m})$. Here, $q = q_0 + \delta q$ and $w = w_0 + \delta w$ are the actual laser power fed to the FEM and the melt pool width generated from the FEM, respectively. The input signals fed to the FEM include a pseudorandom binary sequence (PRBS) signal and multiple sinusoidal signals (10$\sim$300 Hz), with a magnitude of 20 W and an add-on DC component of $q_0 = 60\,\mathrm{W}$. The

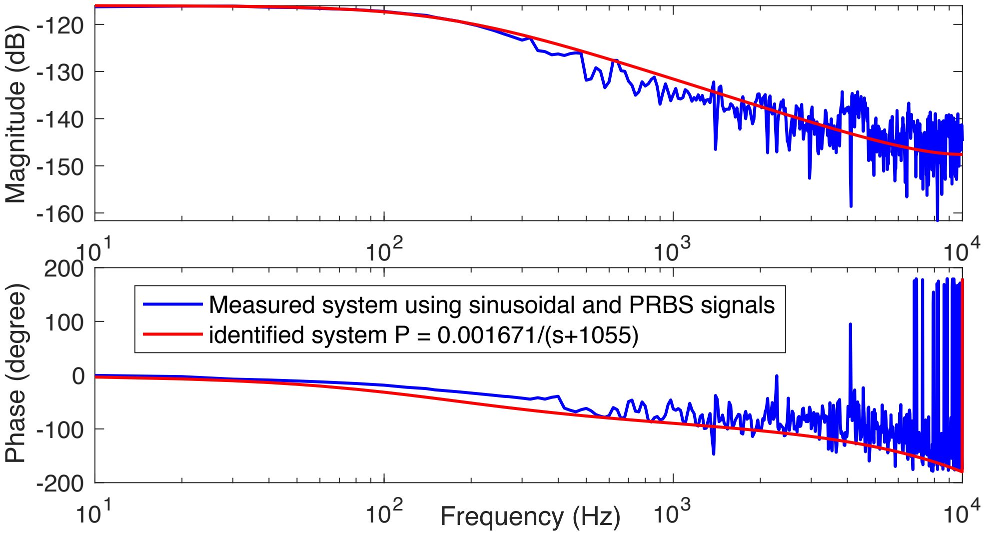

Figure 4.1: Measured and identified system responses.

frequency responses of the measured and identified systems match well with each other (Fig. 4.1). Under the sampling time T_s of 0.5 ms, the zero-order-hold (ZOH) equivalent of the plant model is $P_d(z) = 6.493 \times 10^{-7}/(z-0.5901)$. As shown in the bottom plot of Fig. 4.2, $P_d(z)$ is further normalized to $P(z) = P_d(z)/c = 0.4099/(z-0.5901)$ that has unit DC gain, where c is the DC gain of $P_d(z)$.

4.3 Nonlinear Hammerstein Model

In this section, we show the limit of the linear model subject to the complicated nonlinear thermomechanical dynamics of LPBF and build a new physics-based Hammerstein mixed-fidelity model to address the limitations. After that, we analyze the stability and robustness of the models. The Hammerstein model is conventionally employed in system identification for nonlinear systems, consisting of a nonlinear static element followed by a linear dynamic element. Recent studies of the Hammerstein model target at parameter estimation and neural network based solutions [36–38]. Here, we repurpose the method for identifying a nonlinear model for LPBF.

4.3.1 Core Physics of Melt Pool at Quasi-Steady State

When a moving point laser source is acting on a large thick plate, the analytical solution of (2.1) in the steady state is the Rosenthal equation in (3.2).

Some assumptions and simplifications in deriving the Rosenthal equation are:

1. *The material's physical coefficients such as k, ρ, and c_p are independent of temperature. Using an average value provides a reasonable approximation and enables a closed-form solution to be obtained.*

2. The internal heat generation is neglected, i.e., $q_s = 0$.

3. The workpiece material is homogeneous and isotropic.

4. When the powder bed is processed long enough, a Quasistationary state is reached, that is, the temperature undergoes no change with time with respect to the coordinate system attached to the heat source, i.e., (ξ, y, z).

5. A point heat source rather than Gaussian distribution is used.

6. The effect of latent heat of fusion is negligible since the absorbed latent heat evolves later on.

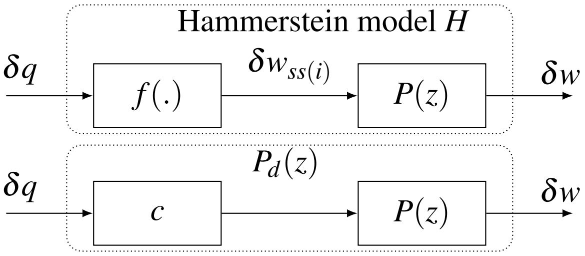

Figure 4.2: Block diagrams of the Hammerstein model and the identified linear model.

From the Rosenthal equation in (3.2), the closed-form equation relating the steady-state melt pool width (w_{ssi} or w_{ss}) with the laser power q is [39]:

$$q = \pi k(T_m - T_0)w_{ssi} + \mathrm{e}\pi\rho c_p(T_m - T_0)u_x w_{ssi}^2/8. \tag{4.1}$$

Assumptions in deriving (4.1) are:

1. $-\frac{\ln(r^*N)}{r^*M} \approx 0$, that is, $r^* \approx \frac{1}{\mathrm{e}N}$, where r^* is the values of r at the melt pool width, $M = \frac{u_x}{2\kappa}$, and $N = \frac{2\pi k(T_m - T_0)}{q}$.

2. $r^*M \gg 1$.

3. The approximation of q is found to be improved by accounting for the zero-speed power in (3.2), that is, the first term on the right hand side of (4.1).

The first two assumptions are reasonably valid for all alloys except AlSi10Mg under typical LPBF configurations.

4.3.2 Structure of the Hammerstein Model

We start to build the Hammerstein model by lumping the memoryless nonlinear submodel in (4.1) with the identified linear dynamics $P(z)$ that has unit DC gain (see Section 4.2). As shown in Fig. 4.2, the Hammerstein model upgrades $P_d(z)$ by replacing the constant c with the nonlinear closed-form expression of the steady-state melt pool width $f(\cdot)$. In (4.1), the values of parameters k, ρ, and c_p are to be determined. Substituting the equilibrium point (q_0, w_0) to (4.1) gives $q_0 = \pi k(T_m - T_0)w_0 + \mathrm{e}\pi\rho c_p(T_m - T_0)u_x w_0^2/8$, that is,

$$\mathrm{e}\rho c_p u_x = 8(Bq_0 - k)/w_0 > 0, \tag{4.2}$$

where $B = 1/[\pi(T_m - T_0)w_0]$ is a constant. In (4.1) and (4.2), ρ and c_p are multiplied together and related to k. Based on the first assumption in Section 4.3.1, we choose $k = 40\,\mathrm{W/(m\cdot k)}$ from Fig. 3.1. Substituting (4.2) to (4.1) yields

$$(Bq_0 - k)w_{ssi}^2 + kw_0 w_{ssi} - Bw_0^2 q = 0. \tag{4.3}$$

Omitting the negative root, we get

$$w_{ssi} = \frac{\sqrt{k^2 + 4(Bq_0 - k)Bq} - k}{2(Bq_0 - k)} w_0. \tag{4.4}$$

With all parameters determined, the Hammerstein model in Fig. 4.2 is thus formalized around the equilibrium point by connecting (4.4) with $P(z)$ and letting $\delta w_{ssi} = w_{ssi} - w_0$ and $\delta q = q - q_0$. Certainly, due to simplifications in deriving (4.1), its direct solution (4.4) only works at specific input conditions. Under the input signal of $\delta q_{10} = 20\mathrm{W}\sin(2\pi f T_s t)$, where $f = 10\mathrm{Hz}$ and T_s is the sampling time, we can tell from Fig. 4.3 that the output of the Hammerstein model (dashed line) deviates greatly from the FEM result (solid line).

To add more flexibility to the nonlinear block, we multiply w_{ssi} in (4.4) with a compensation factor $\alpha(q)$:

$$w_{ss} = \frac{\sqrt{k^2 + 4(Bq_0 - k)Bq} - k}{2(Bq_0 - k)} w_0 \alpha(q), \tag{4.5}$$

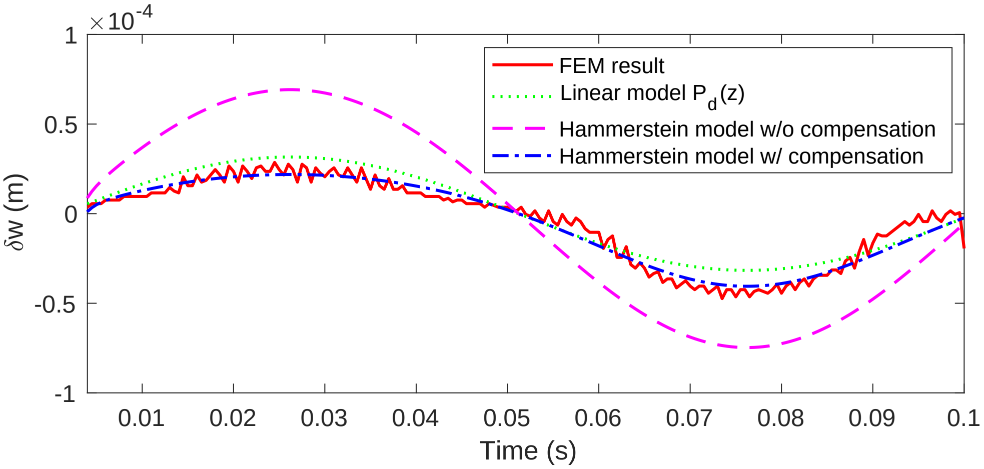

Figure 4.3: Parameter identification of the Hammerstein model with input signal of 10 Hz.

where $\alpha(q)$ is a quadratic function that passes through three points $(60\,\mathrm{W},\,1)$ (i.e., no compensation at the equilibrium point), $(80\,\mathrm{W},\,\alpha_1)$ (i.e., the maximum laser power), and $(40\,\mathrm{W},\,\alpha_2)$ (i.e., the minimum laser power). We identify the parameters α_1 and α_2, respectively, as 0.8507 and 1.1973 using the Parameter Estimation tool in MATLAB. The nonlinear least square regression is used to minimize the sum of squared errors between the FEM data and the output of the updated Hammerstein model with compensation (solid and dash-dotted lines in Fig. 4.3).

The compensated Hammerstein model is achieved by using (4.5) instead of (4.4) and letting $\delta w_{ss} = w_{ss} - w_0$. From Fig. 4.3, we can also tell that this Hammerstein model (dash-dotted line) gives a better approximation (41% increasing) of the system dynamics (solid line) than the identified linear model $P_d(z)$ (dotted line). More generally, as shown in Fig. 4.4, under different input frequencies, the compensated Hammerstein model yields smaller root mean squared errors (e.g., 4.67 µm at 10 Hz) with respect to the FEM result than the linear model (7.89 µm at 10 Hz) and achieves increasing model accuracies (41% increasing at 10 Hz). Fig. 4.5 illustrates the results of the compensated Hammerstein model and the FEM under the input frequency of 60 Hz. Following the procedures from (4.2) to (4.5), we can adaptively build the Hammerstein model for each specific equilibrium point and structurally draw the complete model map for the entire task space of LPBF.

We compare in Fig. 4.6 how δw_{ss} changes with respect to δq under different modeling schemes. In the identified linear model $P_d(z)$, the gradient of the dash-dotted line that links δw_{ss} with δq is the constant c (Fig. 4.2). From Fig. 4.6, we can tell that $P_d(z)$ is only a linear representation of the nonlinear Hammerstein model (solid line) near the equilibrium point. It is remarkable how $P_d(z)$

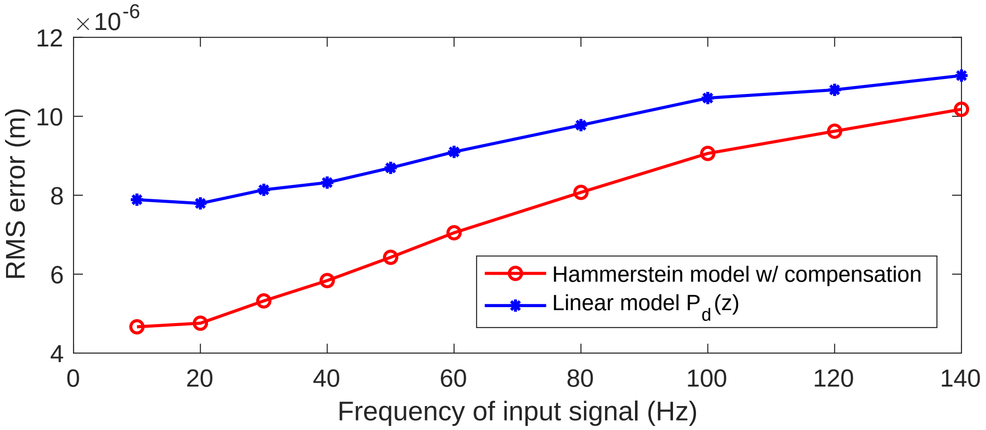

Figure 4.4: Root mean squared (RMS) errors with respect to different input frequencies.

identified from the FEM data coincides tangentially with the Hammerstein model derived from the governing equation. Next we will conduct the stability and robustness analyses to investigate when $P_d(z)$ would fail in representing the Hammerstein model.

4.3.3 Stability and Robustness

Based on the Hammerstein model, we evaluate the robustness and stability properties of the linear models $P_d(z)$ that are commonly used in practice. Let $H = P_d(z)(1+\Delta)$, where H is the Hammerstein model and Δ is the bounded model uncertainty. From Fig. 4.2, we have $\delta w_{ss} \cdot P(z) = \delta q \cdot cP(z)(1+\Delta)$, which gives

$$|\Delta| = \left|\frac{\delta w_{ss}}{c\delta q} - 1\right| \tag{4.6}$$

that is specified by the distance between the dash-dotted and solid lines in Fig. 4.6.

Theorem 1. *When there is (stable and bounded) model uncertainty* $\Delta(z)$ *such that* $\hat{P}(z) = P(z)(1+\Delta(z))$*, standard robust-stability analysis [40] gives that the closed-loop system is stable if and only if both of the following hold:*

1. *Nominal stability condition is satisfied, that is, the closed loop is stable when* $\Delta = 0$.

2. *Robust stability requirement is met by applying the small gain theorem [41]: for any frequency* Ω *in Hz,* $\left|\Delta \cdot T(e^{j\Omega T_s})\right| < 1$*, that is,* $|\Delta| < 1/\left|T(e^{j\Omega T_s})\right|$*, where* $T(z)$ *is the complementary sensitivity function [1].*

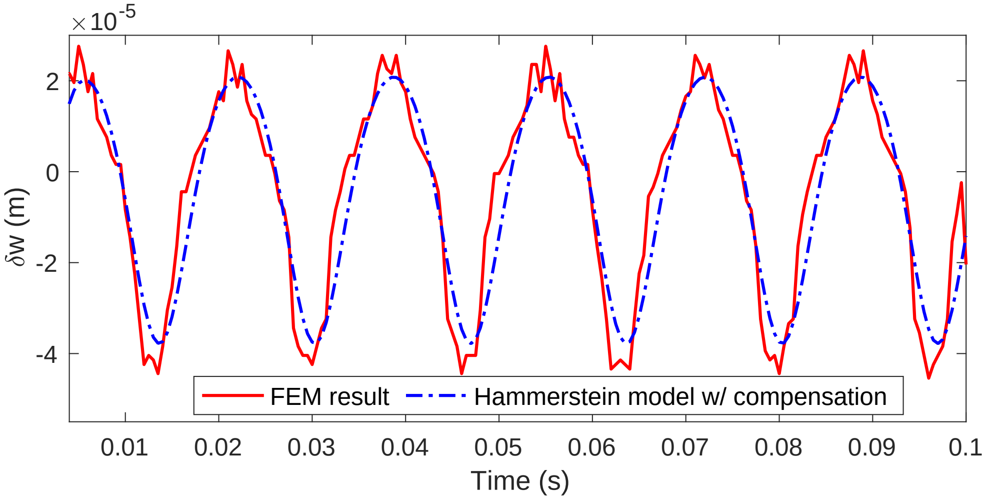

Figure 4.5: Melt pool width changes with input signal of 60 Hz.

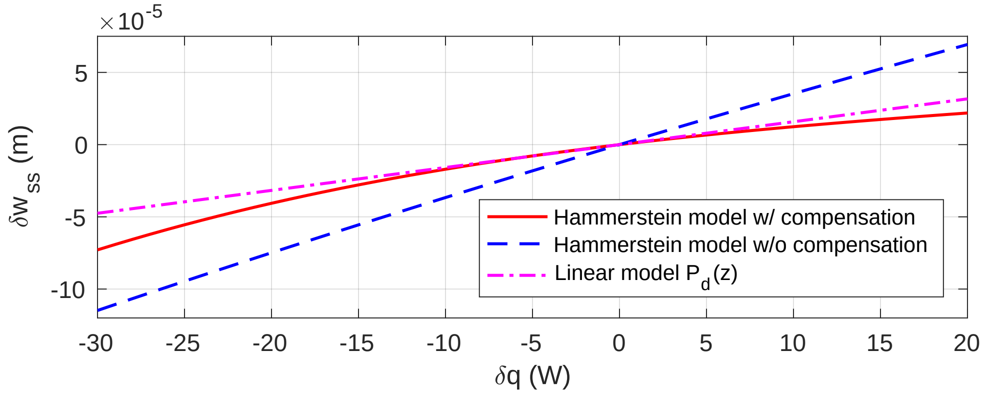

Figure 4.6: Steady-state melt pool width changes of different models.

Note that $|\Delta|$ in (4.6) is positively correlated to the control signal δq, that is, more laser power deviation from the equilibrium point yields a larger $|\Delta|$. Under a certain frequency Ω, we need to make sure the maximum $|\Delta|$ is less than $1/\left|T(e^{j\Omega T_s})\right|$. When the condition is violated, $P_d(z)$ will no longer be a valid representation of the Hammerstein model.

A sufficient condition for the stability of the Hammerstein model is the BIBO stability of the linear model $P(z)$ (Fig. 4.2) [37]. In practice, the linear model is typically a rational transfer function, whose stability can be easily examined.

4.3.4 Control Implementation

Although the focus of this chapter is on the modeling of the complex physics in LPBF, we have additionally presented in Fig. 4.7 a typical feedback loop when applying the Hammerstein model. An $f^{-1}(\cdot)$ block is prepended with the block of the Hammerstein model. Combining these two blocks together yields the linear model $P(z)$. It is thereafter standard practice to design the control algorithms for $P(z)$. To find the inverse of the nonlinear element, we can use a high-order polynomial to approximate f (solid line in Fig. 4.6). Besides, [36] proposes an approximate method for the cases when f is not invertible.

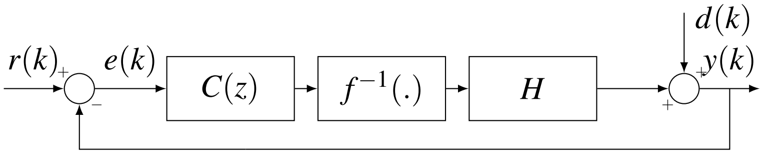

Figure 4.7: Block diagram of feedback control for a Hammerstein model.

Part II

MODEL-BASED MULTIRATE FEEDBACK CONTROL

Chapter 5

LOOP-SHAPING CONTROL

5.1 Introduction

A precision servo system aims at accurately positioning the controlled object(s) to follow the desired trajectories. The controlled object here, for instance, can be a galvo scanner for deflecting a laser beam in LPBF [42], a read/write head for accessing data in a commercial hard disk drive (HDD) [43], or a stage for carrying wafers (called wafer stage) in semiconductor lithography [44]. In all examples, the required position accuracies are quite high. Such ultra-high precision is achieved by careful consideration of various disciplines in mechanical engineering. From the viewpoint of system integration, the design elements are classified to the following four categories.

- *hardware and sensing components*: such as fluid or air bearings for reduced friction, laser interferometers or high-precision encoders for accurate measurements, and piezo-electronic actuators for fine positioning;

- *operation environment*: for example, friction-isolation tables, clean room, and thermostatic chambers;

- *task plans and arrangements*: well-designed trajectories, repetitive tasks in a manufacturing process, etc.;

- *servo control algorithms*: adaptive control, RC, predictive control, optimal control, and so on.

A well-designed precision system needs optimized considerations in all the above categories. Servo control, as the final step, is responsible for compensating as much as possible the imperfections from the previous three design processes. Such imperfections include: 1) *hardware imperfection*, such as system resonances, delays in motor drivers, and delays in signal acquisition; 2) *environmental disturbance*, such as turbulent airflow, periodic disturbance from cooling fans in HDD, and structural coupling between mirrors in the galvo scanner, as will be shown in Section 6.3.1; 3) *special errors due to the task nature*, such as repeated trajectories in the wafer scanner and LPBF.

Errors from the above sources present great challenges in reaching position accuracies at the micro/nano scale. Fortunately, part of them—for example, imperfect motor rotation, repeated trajectories, and fan noises—are repeatable once the hardware and the trajectory are fixed. Other errors—such as environmental vibrations—although may vary case by case, are at least structured and can be compensated by carefully designed servo controllers.

In this chapter, the loop shaping of the feedback control in precision positioning systems is considered. In the presence of various aforementioned error sources, the feedback loop needs to have the flexibility of providing different closed-loop features for error reduction and guarantee the stability under different loop modifications. To satisfy this requirement, enhanced control at selected frequencies has been adopted by many researchers. Based on the location of servo enhancement, enhanced control can be categorized into three groups to deal with: (i) independent disturbance frequencies by, for instance, peak filters [45, 46], adaptive feedforward cancellation [47, 48], disturbance observers (DOBs) [40, 49, 50], and YK parameterization [51–54]; (ii) a fundamental frequency and its integer multiples by means of RC and its variants [34, 55]; (iii) broadband frequencies through adaptive disturbance rejection [56], adaptive noise cancellation [57], and so on. This chapter discusses our recent results in enhanced control to reach the desired servo goals.

The main contributions of the chapter are:

- building flexible feedback loop-shaping schemes to compensate various error sources in precision positioning;
- formulating a new outer-loop inverse-based YK parameterization;
- presenting a detailed case study on the galvo scanner system to validate the proposed control algorithm.

The remainder of the chapter will unfold and discuss several feedback control algorithms including add-on designs for precision positioning. Section 5.2 reviews some fundamental feedback controller parameterizations. From there, Section 5.3 discusses the proposed controller factorizations, that is, inverse-based YK parameterization and its variant. A case study is conducted on a galvo scanner control in Section 5.4, and several comments on feedforward designs are provided.

5.2 Feedback Controller Parameterization

This section briefly reviews several fundamental concepts in feedback control and introduces YK parameterization for flexible servo designs.

A precision positioning system is designed to have an accurate plant dynamics P which is usually linear and time-invariant. For a single-input single-output plant controlled by linear controllers (at least at the steady state), the position servo design can essentially be cast as a loop shaping problem. Consider the block diagram of a standard feedback design in Fig. 2.1. The closed-loop transfer function from the disturbance d to the plant output y is defined as the sensitivity function $S \triangleq 1/(1+PC)$. The complementary sensitivity function is given by $T \triangleq 1-S = PC/(1+PC)$, that is, T is the transfer function from the reference r to y. The sensitivity function measures the closed-loop disturbance-attenuation property, while the complementary sensitivity function defines how the system responds to the reference input as well as the sensor noise. Consider a typical magnitude response of S in Fig. 5.1. Below the bandwidth $\Omega_c = 2\pi\omega_c$, the magnitude of $S(j\Omega)$ is less than 1, which infers the attenuation of d in Fig. 2.1. Due to the fundamental relationship $S+T=1$, wherever the magnitude of $S(j\Omega)$ is small, $T(j\Omega)$ is close to unity, which means that at frequencies where good disturbance rejection is achieved, improved reference tracking is also obtained.

The bandwidth in Fig. 5.1 cannot be pushed to be arbitrarily large. From the practical perspective, a mechanical system cannot respond to arbitrarily fast control inputs due to hardware (such as motors, gears, etc.) limitations. It is common practice to keep the gain of the controller small at high frequencies. From the theoretical perspective, under mild conditions,[1] it is inevitable to have $|S(j\Omega^{'})| > 1$ at certain frequencies if $|S(j\Omega)| < 1$ holds over some other frequency intervals, namely, when certain disturbance components are attenuated, some others are amplified. This is the "waterbed" effect which comes from Bode's Integral Theorem, a fundamental result of linear control design.

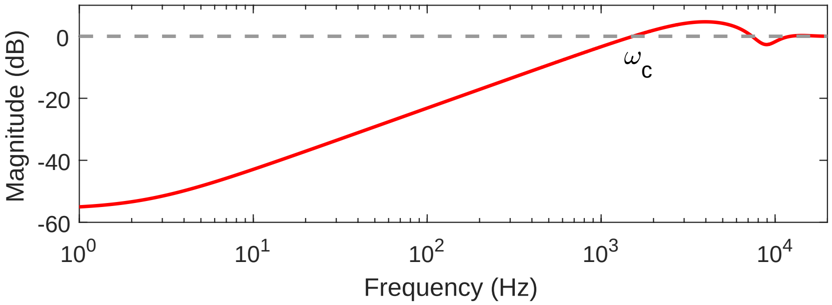

Figure 5.1: Magnitude response of the sensitivity function in Section 5.4.3.

---

[1] For continuous-time systems, the waterbed effect holds if the relative degree of the loop transfer function $L = PC$ is no less than 2. In the discrete-time case, the waterbed effect always holds.

Well formulated tools such as PID, lead-lag, and H_∞ controllers are available to achieve a loop shape that is similar to the one in Fig. 5.1. We focus next on how to perform safe and flexible add-on modifications to such a standard baseline loop shape.

A foundational tool suitable for achieving the design goal is the YK parameterization [53, 54], also known as all-stabilizing controller parameterization. If a plant $P = N/D$ can be stabilized by a negative-feedback controller $C = X/Y$ with (N, D) and (X, Y) being coprime pairs over the set $\mathscr{S} = \{$stable, proper, and rational transfer functions$\}$, then any stabilizing feedback controller can be represented by means of the YK parameterization as

$$C_{all} = \frac{X+DQ}{Y-NQ} : \ Q \in \mathscr{S}, \ Y(\infty) - N(\infty)Q(\infty) \neq 0. \tag{5.1}$$

Here a pair (N, D) is called coprime over $\mathscr{S}$, if $N, D \in \mathscr{S}$ and there exists $U, V \in \mathscr{S}$ such that $UN + VD = 1$.[2]

The sensitivity function with controller (5.1) in the loop is

$$\tilde{S} = \frac{1}{1+PC_{all}} = \frac{1}{1+PC}\left[1 - \frac{N}{Y}Q\right], \tag{5.2}$$

which is affine in Q. Therefore, changing Q can directly shape $\tilde{S}$, which is much more convenient compared to redesigning C in the denominator of $\tilde{S}$.

For stable P and C, one can simply choose $N = P$, $D = 1$, $X = C$, and $Y = 1$ in (5.1). Thus, (N, D) and (X, Y) are valid coprime factorizations since we can pick, for example, $U = C/(1+PC) \in \mathscr{S}$ and $V = 1/(1+PC) \in \mathscr{S}$ to make $UN + VD = 1$. In this case, a simplified and easier-to-use version of (5.1) and (5.2) can be obtained

$$\tilde{C} = \frac{C+Q}{1-PQ} : \ Q \in \mathscr{S}. \tag{5.3}$$

$$\tilde{S} = \frac{1}{1+P\tilde{C}} = \frac{1-PQ}{1+PC}. \tag{5.4}$$

The remaining design task about choosing Q in (5.4) depends on the plant P and the desired closed-loop response. For example, candidate Q-filter designs can be found by using a linear combination of some basis transfer functions (e.g., $\sum_{i=0}^{k_Q} \theta_i z^{-i}$ in discrete-time schemes), and adaptive/H_∞ control can be applied to find the scaling coefficients for the combination [40]. Regardless of what tools are used, to achieve good disturbance attenuation, $\tilde{S}$ in (5.4) is required to

---

[2] The inequality $Y(\infty) - N(\infty)Q(\infty) \neq 0$ makes the closed loop to be well-posed. This condition is usually easy to satisfy for practical problems. Consider, for example, the case where $P = z^{-1}$ and $C = 0.8$. We have $N = z^{-1}$, $D = 1$, $X = 0.8$, $Y = 1$, and $Y(z=\infty) - N(z=\infty)Q(z=\infty) = 1$.

be small, and hence PQ should be close to 1 at the desired frequencies. Consider a block-diagram realization in Fig. 5.2[3]. In the inner loop marked by $\star$, Q should then approximate P^{-1} to make $PQ \approx 1$.

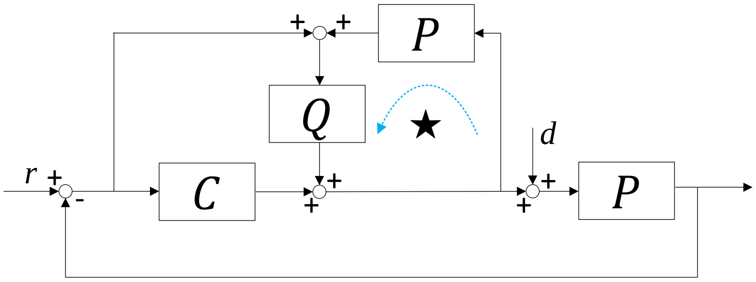

Figure 5.2: A forward-model YK parameterization.

5.3 Proposed Controller Factorization

Instead of a direct inversion of P by Q, this section discusses an alternative scheme that brings additional simplifications to (5.4). Although a general analysis can be made, we focus on precision servo systems and assume that the baseline controller C is stable.

Consider designing inverse-based YK parameterization in two steps: first to perform a stable model inversion P^{-1} and second to use Q for controlling the amount of loop shaping and disturbance rejection. Of course, a perfect inversion of the plant dynamics is practically impossible, and a nominal version $\hat{P}^{-1}$ has to be adopted. In addition, during discrete-time implementation, the sampled-data transfer function $\hat{P}^{-1}(z)$ is possibly not causal/realizable since a practical plant P usually has delays (suppose m steps of delays) that become z^m when inverted, where z is the complex indeterminate in z-transform. For realizability, consider using instead $z^{-m}\hat{P}^{-1}(z)$. For the moment, $\hat{P}^{-1}(z)$ is assumed to be stable. This is not difficult to achieve for precision positioning systems. Chapter 7 will discuss more about this model inversion topic. A block diagram of the alternative scheme is shown in Fig. 5.3. Compared to Fig. 5.2, this discrete-time scheme is closer to actual implementation, and modifications have been made to reduce the dependence of the plant information in the $(\star)$ loop in Fig. 5.2.

---

[3] In reality, d is usually generated in front of the plant. When the frequency response of the plant is known, d in Fig. 5.2 can be mapped to d_0 in Fig. 2.1 by $D_0(e^{j\omega}) = D(e^{j\omega})P(e^{j\omega})$.

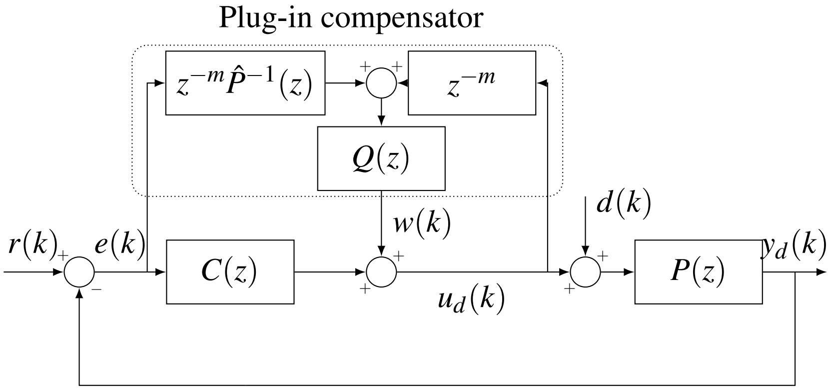

Figure 5.3: Block diagram of a plug-in RC design.

The transfer function of the overall feedback controller from $e(k)$ to $u_d(k)$ in Fig. 5.3 is

$$C_{all}(z) = \frac{C(z) + z^{-m}\hat{P}^{-1}(z)Q(z)}{1 - z^{-m}Q(z)}, \tag{5.5}$$

where high-gain control (increased control effort) is directly provided by $1/(1 - z^{-m}Q(z))$ instead of $1/(1 - PQ)$ in (5.3). This reduced dependence on P is also reflected in the frequency sensitivity function $\tilde{S}(e^{j\omega}) = \tilde{S}(z)\big|_{z=e^{j\omega}}$. If $\hat{P}(e^{j\omega}) = P(e^{j\omega})$, (5.5) gives

$$\begin{aligned} \tilde{S}(e^{j\omega}) &= \frac{1}{1 + P(e^{j\omega})C_{all}(e^{j\omega})} = \frac{1 - e^{-mj\omega}Q(e^{j\omega})}{1 + P(e^{j\omega})C(e^{j\omega})} \\ &= S_0(z)(1 - z^{-m}Q(z))\big|_{z=e^{j\omega}}. \end{aligned} \tag{5.6}$$

In some practices, when the plant and built-in controller (e.g., designed by manufacturers in the factory) are lumped together, only signals v and y in Fig. 5.4 are accessible, and separating the plant model P_e is infeasible. In this circumstance, an outer loop can be designed by adding one positive feedback loop and, at the same time, one negative feedback loop outside the original loop shaping, as shown in Fig. 5.4. With $C = 1$, the servo performance of the original feedback loop keeps unchanged. Take $L(z) \triangleq P_eC_e$ as the new plant. This augmented plant model $L(z)$ can be computed from $T_e(z)$, the transfer function from v to y, by $L(z) = T_e(z)/(1 - T_e(z))$. Then the controller $C(= 1)$ can be extended to obtain the desired closed-loop response. In Fig. 5.5, the inverse-based YK parameterization is added on C. With $C(e^{j\omega}) = 1$ as well as $P(e^{j\omega})$ replaced by $L(e^{j\omega})$ in (5.5) and (5.6), the outer-loop inverse-based YK parameterization gives

$$C_{all}(z) = \frac{1 + z^{-m}\hat{L}^{-1}(z)Q(z)}{1 - z^{-m}Q(z)}. \tag{5.7}$$

$$\tilde{S}(e^{j\omega}) = \frac{1}{1+L(e^{j\omega})}(1-z^{-m}Q(z))\bigg|_{z=e^{j\omega}}. \tag{5.8}$$

Nominal stability of the closed-loop system can be guaranteed given proper coprime factorizations. Summarizing the requirements in each of the four introduced YK schemes yields Table 5.1.

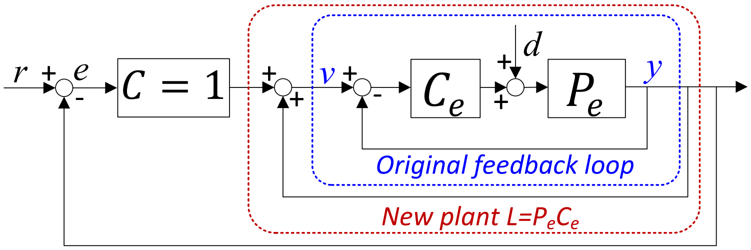

Figure 5.4: An outer-loop block diagram.

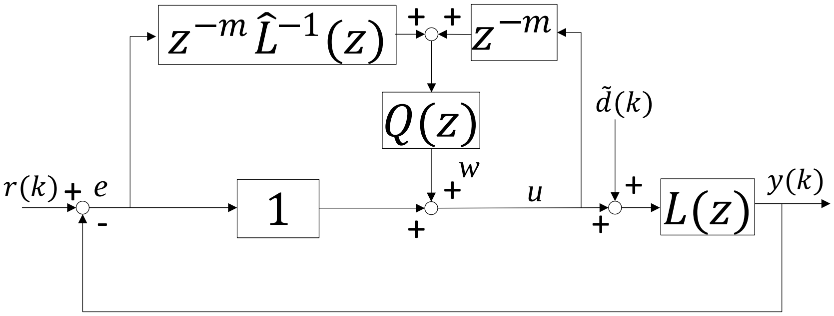

Figure 5.5: An outer-loop inverse-based YK parameterization.

Table 5.1: Nominal stability conditions for the four add-on designs.

YK parameterization	Simplified YK parameterization	inverse-based YK parameterization	Outer-loop YK parameterization
$Q \in \mathscr{S}$	$P, C, Q \in \mathscr{S}$	$\hat{P}^{-1}, C, Q \in \mathscr{S}$	$\hat{L}^{-1}, Q \in \mathscr{S}$

Remark 1. *The robust stability requirement in Theorem 1 in Section 4.3.3 is not difficult to satisfy. Take the inverse-based YK parameterization in (5.6) as an example, where* $\tilde{T}(e^{j\omega})$ *is given by*

$$\tilde{T}(e^{j\omega}) = \frac{\hat{P}(e^{j\omega})C(e^{j\omega}) + e^{-mj\omega}Q(e^{j\omega})}{1+\hat{P}(e^{j\omega})C(e^{j\omega})}. \tag{5.9}$$

If $Q(e^{j\omega}) = 0$, $\tilde{T}(e^{j\omega})$ *reduces to the original complementary sensitivity function* $T_0(e^{j\omega})$ *without the add-on design. We thus have* $\left|\Delta(e^{j\omega})T_0(e^{j\omega})\right| < 1$, *which is the robust stability condition of the baseline feedback loop. If* $e^{-mj\omega}Q(e^{j\omega}) = 1$, $\tilde{T}(e^{j\omega}) = 1$. *At these frequencies,* $\left|\Delta(e^{j\omega})\right| < 1$ *is required, that is, the mismatch between* $P(e^{j\omega})$ *and* $\hat{P}(e^{j\omega})$ *has to be less than 100%.*

In (5.6) and (5.8), the add-on design narrows down to the design of $1 - z^{-m}Q(z)$, which is much simpler than $1 - PQ$ in (5.4) and $1 - NQ/Y$ in (5.2). Several general design guides for $Q(z)$ can now be made.

5.3.1 Low-frequency Servo Enhancement

An intuitive choice for $Q(z)$ is a low-pass filter. In this case, if the delay of the plant is not very large, then the frequency transfer function $1 - e^{-j\omega m}Q(e^{j\omega})$ would be small when $Q(e^{j\omega})$ is approximately one at low frequencies and be close to unity when $|Q(e^{j\omega})| \ll 1$ at high frequencies. A direct result is that any bias disturbance can be rejected. This is because under the low-pass assumption, $1 - e^{-jm\times 0}Q(e^{j\times 0}) = 1 - Q(e^{j\times 0}) = 0$ at $\omega = 0$. Therefore, an integral action is built into the closed-loop controller.

5.3.2 Narrow-band Disturbance Rejection

Vibrations are frequency-dependent signals by nature. Since the closed-loop bandwidth cannot be arbitrarily increased, vibrations at frequencies above the servo bandwidth are fundamentally more difficult to handle. Actually, such band-limited disturbances, if strong enough, significantly limit the servo performance. To compensate for such vibrations, some special feedback adjustments are needed. Meantime, we commonly want to keep as much as possible the original loop shape because it is often achieved by means of careful baseline design. A candidate add-on design is to use the proposed inverse-based YK parameterization and design a notch shape for $1 - z^{-m}Q(z)$ such as the one shown in the bottom plot of Fig. 5.6. To demonstrate the flexibility, five notches are introduced in the magnitude of $1 - z^{-m}Q(z)$. The first three notches are very close to each other, and the other two are separated at higher frequencies. When $1 - e^{-mj\omega}Q(e^{j\omega})$ is close to unity, $\tilde{S}(e^{j\omega}) = S_0(z)(1 - z^{-m}Q(z))|_{z=e^{j\omega}}$ is close to $S_0(e^{j\omega})$, and hence the original loop shape is maintained. At frequencies where $1-z^{-m}Q(z)$ has very small gains in Fig. 5.6, the overall controller (5.5) then has high gain, $\tilde{S}(e^{j\omega})$ is very small, and hence vibrations can be attenuated.

An example about disturbance attenuation in an HDD benchmark problem [58] is presented in Fig. 5.7. This benchmark has been used in a number of publications on information storage systems. The compensation scheme is implemented for rejecting two strong vibrations at around 1100 Hz and 1500 Hz. Both vibrations occur at frequencies above the baseline servo bandwidth (1060 Hz) and cannot be attenuated in the standard feedback setting. After compensation, the two originally sharp spectral peaks are actually visually not detectable due to the deep notch shape of $1-z^{-m}Q(z)$ in Fig. 5.6.

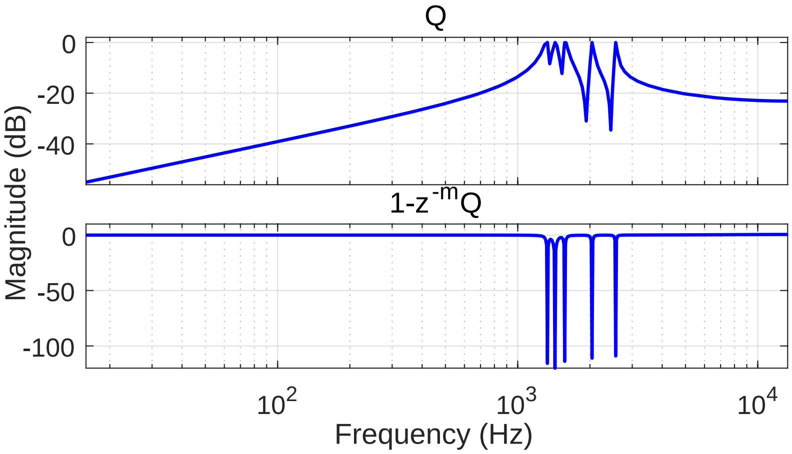

Figure 5.6: A Q-design example for narrow-band disturbance rejection.

Take the example of $m=1$. The key concept of Q design is to have a notch shape of $1-z^{-1}Q(z)$ at certain disturbance frequency $\omega_0 = 2\pi f_0 T_s$, where T_s is the sampling time and f_0 is in Hz. Designing $1-z^{-1}Q(z) = \frac{1-2\cos\omega_0 z^{-1}+z^{-2}}{1-2\alpha\cos\omega_0 z^{-1}+\alpha^2 z^{-2}}$ and solving for $Q(z)$ gives

$$Q(z) = \frac{a(\alpha-1)+(\alpha^2-1)z^{-1}}{1+a\alpha z^{-1}+\alpha^2 z^{-2}},\ a=-2\cos(\omega_0). \tag{5.10}$$

Extending (5.10), if multiple notches are desired, with $1-z^{-1}Q(z) = A(z^{-1})/A(\alpha z^{-1})$, $A(\alpha z^{-1}) = \prod_{i=1}^{n}(1-2\cos(\Omega_i T_s)\alpha z^{-1}+\alpha^2 z^{-2})$, and $A(z^{-1}) = A(\alpha z^{-1})\big|_{\alpha=1}$, letting $Q(z) = B_Q(z^{-1})/A_Q(z^{-1})$

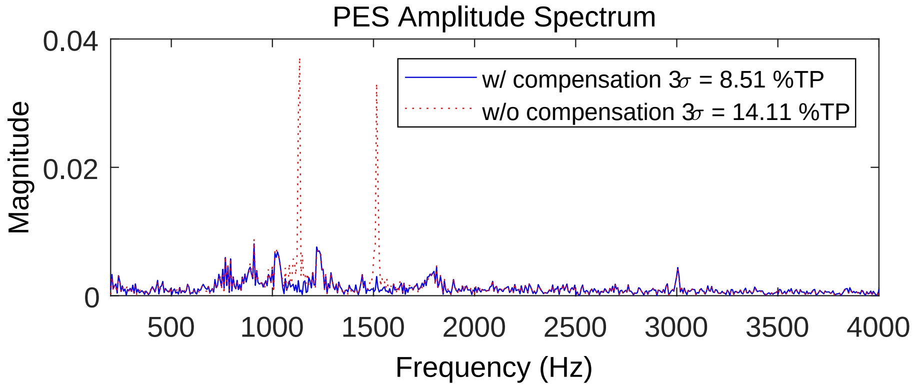

Figure 5.7: Frequency spectra of the position error signals in a simulated HDD benchmark: 1 TP (Track Pitch) = 254nm in this example.

gives the general solution

$$A_Q(z^{-1}) = 1 + \sum_{i=1}^{n-1} a_i(\alpha^i z^{-i} + \alpha^{2n-i} z^{-2n+i}) + a_n \alpha^n z^{-n} + \alpha^{2n} z^{-2n}.$$

$$B_Q(z^{-1}) = \sum_{i=1}^{2n} (\alpha^i - 1) a_i z^{-i+1}. \ a_i = a_{2n-i}. \tag{5.11}$$

Here $\alpha(< 1)$ controls the width of the attenuation regions and can be taken very close to 1 for narrow-band disturbance rejection. The coefficients a_i's in (5.10) and (5.11) determine the notch frequencies of $Q(z)$. In (5.11), a_i and the desired notch frequency Ω_i in rad/s are connected by the mapping $A_Q(z^{-1}) = A(\alpha z^{-1})$.

When $m > 1$, several additional steps are needed since $1 - z^{-m}Q(z) = A(z^{-1})/A(\alpha z^{-1})$ would not have a realizable solution. An approach that uses Diophantine identity to address this issue is provided in the reference [49]. Specifically, when $m = 2$, the expression of $Q(z)$ is

$$Q(z) = \frac{\left[\alpha^2 - 1 - a^2(\alpha - 1)\right] - a(\alpha - 1)z^{-1}}{1 + a\alpha z^{-1} + \alpha^2 z^{-2}}, \tag{5.12}$$

where α and a have the same meanings as those in (5.10).

5.3.3 Repetitive Control

An example application of RC is for addressing the problem involved in wafer-scanning process, one key step for circuit fabrication in the semiconductor industry. To print the circuit, the wafer is exposed to patterned ultraviolet lights that come through a mask carried by a reticle stage. The wafer stage and the reticle stage move the wafer and the mask in a synchronized manner. Due to the limited size of the lens, only a small part of the wafer is exposed at each scan, and the wafer is moved from one field to another between the scans. The scanning process is repeated until all required areas on the wafer have been exposed under the light. An intuition about RC is that if the same type of disturbance occurs after a fixed period of time, that is, $d(k) = d(k - N_d)$ where N_d is the period of the disturbance, then at the next occurrence of $d(k)$, we can learn and reduce the resulting error, no matter how it behaves within one period of time. From the spectral perspective, the magnitude response of $1 - z^{-m}Q(z)$ in Fig. 6.4 provides a typical loop shape for RC that $|1 - e^{-jm\omega}Q(e^{j\omega})|$ gives low gains to $|\tilde{S}(e^{j\omega})|$ at the fundamental frequency and its integer multiples. Meanwhile, at other frequencies $|1 - e^{-jm\omega}Q(e^{j\omega})|$ is approximately unity yielding no change to $|\tilde{S}(e^{j\omega})|$. More details will be provided in Chapter 6.

5.3.4 General Band-limited Vibration Compensation

The loop shaping in Section 5.3.2 is for narrow-band disturbance rejection. When excitation sources are rich in frequency, a wider attenuation bandwidth of $1 - z^{-m}Q(z)$ is needed and can be achieved by changing the design parameter α in (5.10) and (5.11), which is related to the width of the $-3\,\mathrm{dB}$ passband for $1 - z^{-m}Q(z)$ by $BW \approx (1-\alpha^2)/[(\alpha^2+1)(\pi T_s)]$ (Hz) [59]. As the disturbance attenuation is pushed further, the trade-off amplification due to the waterbed effect also increases. Additional design considerations are therefore necessary for a safe implementation. Fig. 5.8 shows the loop-shaping result on an HDD benchmark example. No large sensitivity amplifications are observed due to: (i) a gain scheduling in the Q-filter with $Q_{\text{implement}} = k_Q Q(z)$ $(k_Q \leq 1)$; (ii) the use of a damped notch filter $F_{nf}(z) = A(\beta z^{-1})/A(\alpha z^{-1})$ $(\alpha < \beta < 1)$ in the design of $Q(z)$. Auxiliary zeros and convex optimization can be applied for specific magnitude constraints on $Q(z)$ [60].

5.4 Application on Laser Scanning

In this section, we provide the design and analysis steps for implementing the (outer-loop) inverse-based YK parameterization on a galvo scanner platform to verify the effectiveness of the proposed servo design. In LPBF, laser beams are controlled to melt the powder materials following pre-designed trajectories. Rather than moving the laser source, LPBF efficiently applies a galvo scanner platform to reflect the laser beams. Besides LPBF, the galvo scanner platform is also widely used in other laser-related applications, such as laser scanning, laser engraving, and laser welding.

A typical galvo scanner platform is composed of two sets of mirrors, galvanometers, and control

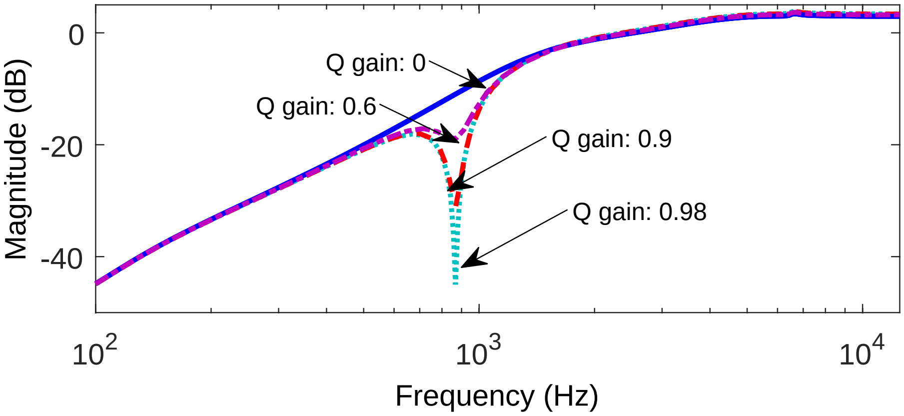

Figure 5.8: The control of attenuation efforts by means of gain scheduling on Q.

systems, as shown in Fig. 5.9. The galvanometer consists of motors to rotate the mirrors and encoders to feedback the mirror position information. A dSPACE DS1104 board connects control system designs in MATLAB with the servo drivers. The mirror assembly is attached to the end of the motors in a coaxial manner and deflects the laser beam over the angular range of the motor shaft, as shown in Fig. 5.10. O_1 and O_2 indicate the centers of the two mirrors, and the corresponding rotation angles are denoted as γ and δ, respectively. L_1 is the distance between the two mirror centers, and L_2 represents the distance between mirror O_2 and the image field O.

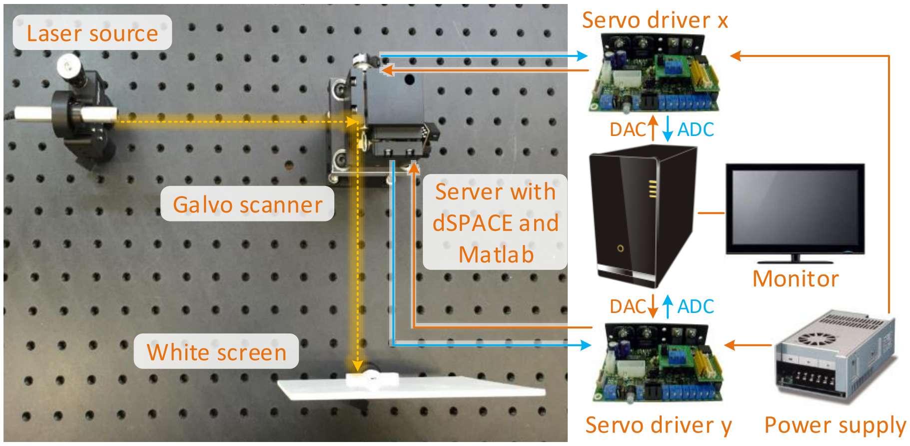

Figure 5.9: Schematic of the galvo scanner platform.

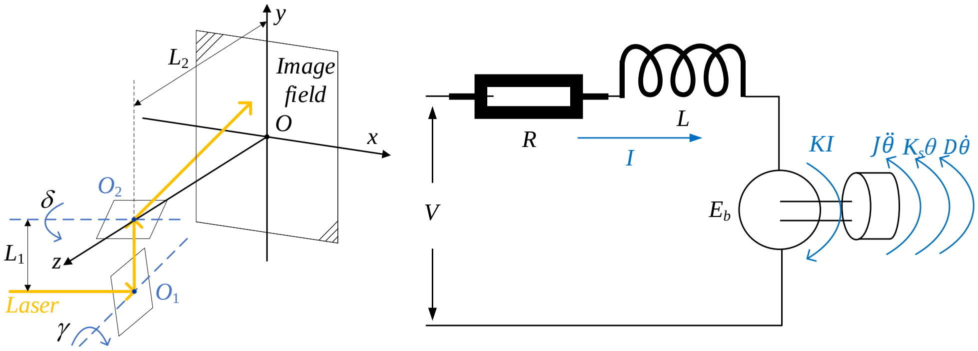

Figure 5.10: Schematic diagram and electrical model of glavo scanner.

5.4.1 Plant Identification, PID Tuning, and Discretization

In the electrical model (Fig. 5.10) of a generalized galvo scanner platform, the open-loop transfer function [61, 62] relating the input drive current $I(s)$ to the output position $\Theta(s)$ is

$$\frac{\Theta(s)}{I(s)} = \frac{K}{K_s + Ds + Js^2}, \tag{5.13}$$

where s is the complex indeterminate in the Laplace transform, K the torque constant, K_s the spring constant of the galvo, D the damping constant, and J the rotor and mirror inertia.

In addition, we have

$$\begin{cases} L\frac{dI}{dt} + RI + E_b = V \\ E_b = K_b\frac{d\Theta}{dt} \end{cases}, \tag{5.14}$$

where E_b is the back electromotive force (EMF), K_b the back EMF constant, L the lumped inductance, and R the lumped resistance.

Combining (5.13) with (5.14), one can obtain the transfer function from the input voltage V to the output position Θ

$$\frac{\Theta}{V} = \frac{K}{(LJ)s^3 + (RJ + DL)s^2 + (RJ + K_sL + K_bK)s + K_sR}. \tag{5.15}$$

With $K_s = 0.02\,\text{Nm}\cdot\text{rad}^{-1}$, $D = 1.74\times10^{-6}\,\text{Ns·m}$, $J = 0.028\,\text{kg}\cdot\text{m}^2$, $K_b = 0.005\,\text{Nm·A}$, $R = 2.3\,\Omega$, $L = 0.001\,\text{H}$, and $K = 0.005\,\text{Nm}\cdot\text{A}^{-1}$, the plant model in (5.15) reduces to a second-order model [61]

$$P(s) = \frac{0.005}{0.0644s^2 + 0.0644s + 0.0460}, \tag{5.16}$$

where the term s^3 in (5.15) is ignored as the coefficient LJ is several orders of magnitude smaller than the other coefficients.

To build a baseline feedback loop, a PID controller, based on the Ziegler-Nichols tuning, is designed as [63]

$$C(s) = 17760(1 + \frac{1}{0.0650s} + 0.0163s). \tag{5.17}$$

To implement the discrete-time YK scheme, by means of the ZOH discretization and the bilinear transformation, the continuous-time plant and controller are, respectively, discretized as

$$C(z)|_{s=\frac{2}{T_s}\frac{1-z^{-1}}{1+z^{-1}}} = 10^4 \frac{4.243z^2 - 7.767z + 3.56}{z^2 - 1.667z + 0.6667}. \tag{5.18}$$

$$P_d(z) = (1 - z^{-1})\mathscr{Z}\left\{\mathscr{L}^{-1}\left[\frac{P(s)}{s}\right]\bigg|_{t=kT_s}\right\}. \tag{5.19}$$

The transfer function of the discrete-time plant with the sampling time $T_s = 0.004\,\text{s}$ is

$$P_d(z) = 10^{-7}\frac{6.203z + 6.195}{z^2 - 1.996z + 0.996}. \tag{5.20}$$

5.4.2 YK Parameterization Implementation

The inverse-based YK parameterization (Fig. 5.3 and (5.5)) is applied to reject disturbances in the galvo scanner platform, such as channel crosstalk (Section 6.3.1), atmospheric turbulence, and environmental vibration. Such disturbances are narrow-band by nature. For demonstration, a proof-of-concept single-frequency disturbance $d(k) = A\sin(2\pi f_0 T_s k)$ is considered.

Here, $P^{-1}(z)$ and $C(z)$ are stable, which means that the prerequisites to implement the inverse-based YK scheme are satisfied. The relative degree m of $P(z)$ in (5.20) is 1. Hence the Q design in (5.10) is applied. Substituting $f_0 = 12.5\,\text{Hz}$, $A = 1\,\text{V}$, $T_s = 0.004\,\text{s}$, and $\alpha = 0.999$ into (5.10) gives

$$Q(z) = \frac{0.001902 - 0.001999z^{-1}}{1 - 1.9z^{-1} + 0.998z^{-2}}. \tag{5.21}$$

As shown in Fig. 5.11, by applying high-gain control of (5.5), a notch shape is introduced for $\left|1 - z^{-1}Q(z)\right|$ at 12.5 Hz, where $|C_{all}(z)| \to \infty$ and $\left|\tilde{S}(z)\right|$ in (5.6) is thus very small, yielding the time-domain output $y(kT_s) = 0$ at 12.5 Hz. At the other frequencies, $\left|1 - z^{-1}Q(z)\right|$ is close to unity, that is, $\left|\tilde{S}(z)\right|$ approximates $|S_0(z)|$, and hence the original loop shape is maintained.

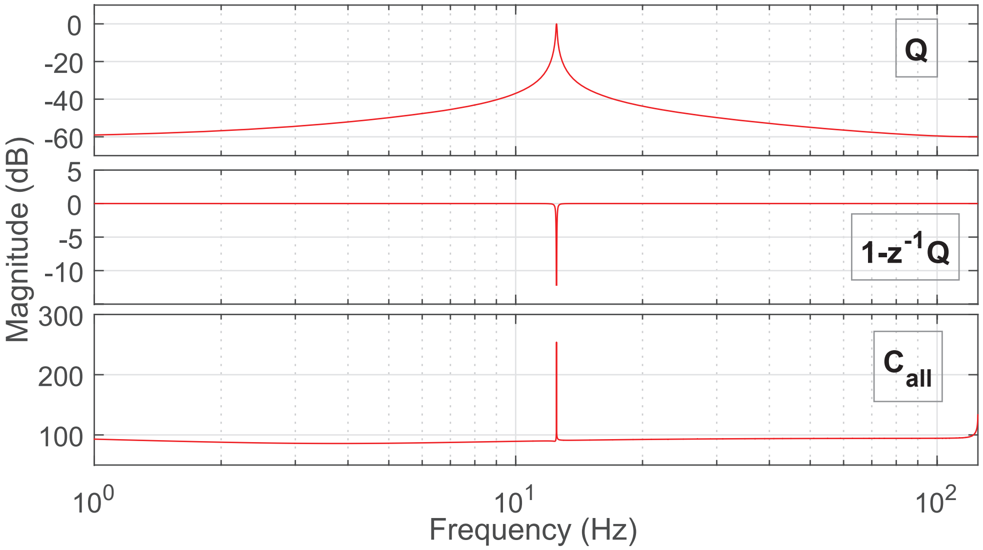

Figure 5.11: Magnitude responses of $Q(z)$, $1-z^{-m}Q(z)$, and $C_{all}(z)$.

In regulation control, the $Q(z)$ output w in Fig. 5.3 acts as a window to check if the Q-filter works well. A good Q design yields w to cancel the disturbance, that is, $w(k) \approx -d(k)$. Hence the inverse-based YK structure acts as an input-DOB. Discussions on this point are provided in the reference [34].

Fig. 5.12 shows the simulated outputs and control efforts with the Q-filter and the baseline PID controller. The results verify that compared with the baseline controller, the inverse-based YK scheme can fully reject the disturbance at 12.5 Hz with increased control efforts.

5.4.3 Experimentation

Experiments are conducted on the galvo scanner platform [42] in Fig. 5.9. During implementation, nonlinearity effects such as slew rate limit and input saturation are insignificant compared with the external disturbance and are thus omitted. The control signal is limited to ±10 V. The system is subjected to broad-band random disturbances at a magnitude of about 10 mV. The sampling time T_s is 0.025 ms, that is, the Nyquist frequency is 20 kHz.

A pseudorandom binary sequence signal is used as an input to estimate the plant model. Magnitude responses of the measured and identified plants are shown in Fig. 5.13. The identified

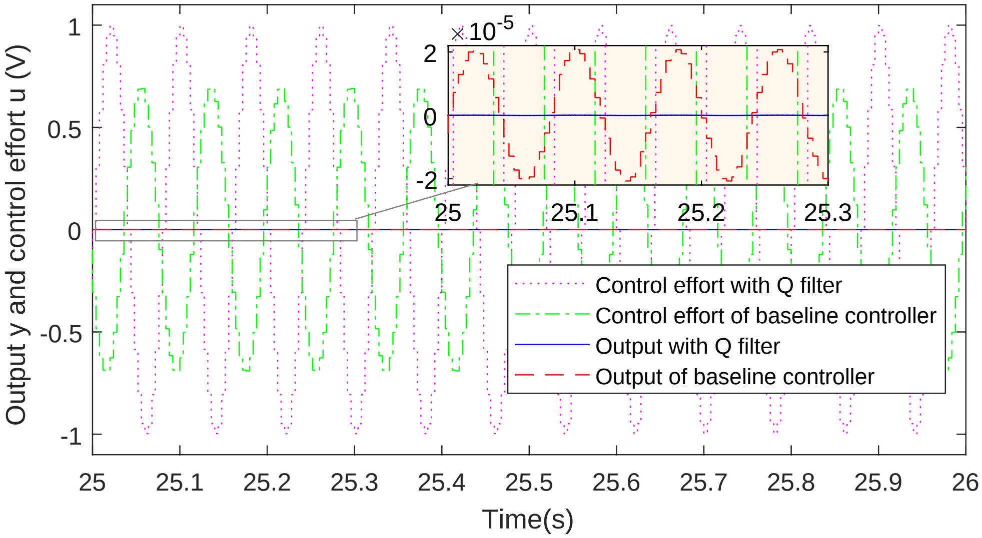

Figure 5.12: Outputs and control efforts of the baseline controller and Q-filter.

plant model is expressed as

$$P_d(z) = \frac{-0.001945z + 0.03172}{z^2 - 1.955z + 0.9703}. \tag{5.22}$$

One can observe that (5.20) and (5.22) share the same structure and similar poles with some gain normalization, which attests to the validity of the identified plant model.

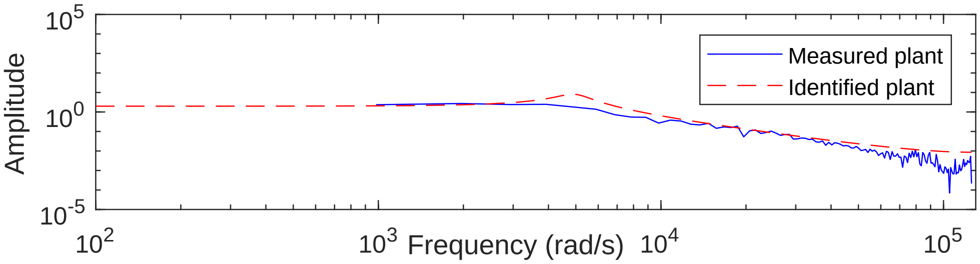

Figure 5.13: Magnitude response of the measured and identified plant.

Next, we take the galvo scanner and the servo drivers, namely, the lumped plant and controller, as the new augmented plant $L(z)$ to apply the outer-loop inverse-based YK parameterization in Fig. 5.5. The bandwidth ω_c of the baseline feedback loop is 1526 Hz, as shown in Fig. 5.1.

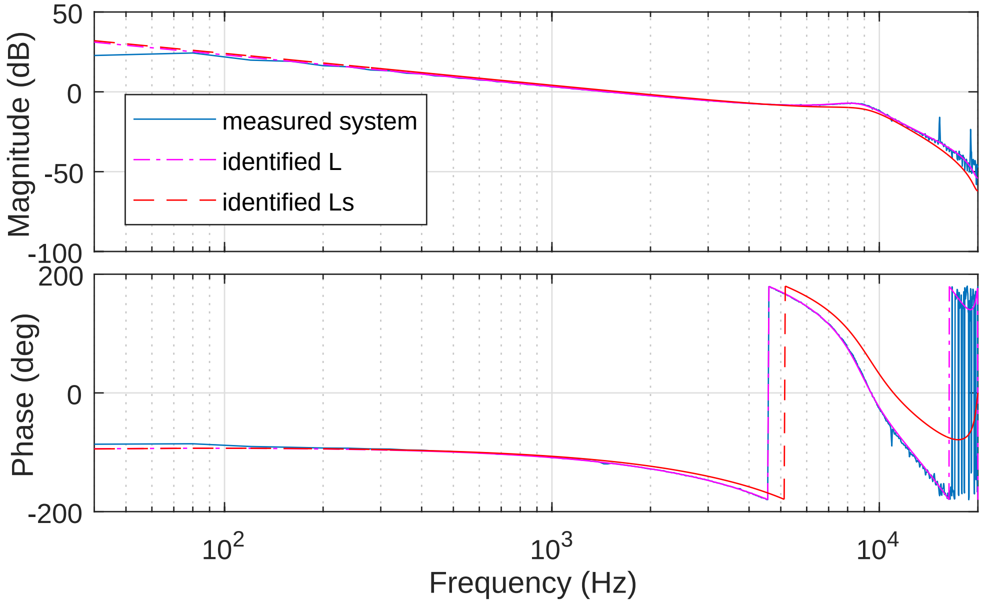

Figure 5.14: Magnitude responses of the measured system, and identified $\hat{L}(z)$, $\hat{L}_s(z)$.

The identified $\hat{L}(z)$ is

$$\hat{L}(z) = \frac{0.02816z^2 + 0.1504z + 0.1146}{z^4 - 1.319z^3 + 0.929z^2 - 0.6073z - 0.0035}. \tag{5.23}$$

Moving the unstable zero of $\hat{L}(z)$ at -4.419 to -0.6 inside the unit circle and keeping the other zeros and poles unchanged generates a new plant $\hat{L}_s(z)$ with a stable inverse $\hat{L}_s^{-1}(z)$

$$\hat{L}_s(z) = \frac{z^2 + 1.521z + 0.5526}{10.49z^4 - 13.83z^3 + 9.037z - 6.312z + 0.6124}. \tag{5.24}$$

The magnitude responses of the measure system, the identified $\hat{L}(z)$, and $\hat{L}_s(z)$ are very close to each other, as illustrated in Fig. 5.14. The Q-filter in Fig. 5.5 is then designed based on the inverse-stable plant $\hat{L}_s(z)$. The relative degree m of $\hat{L}_s(z)$ is 2. A disturbance with $f_0 = 5\,\text{kHz}$ and $A = 0.1\,\text{V}$ is introduced to the system. f_0 at $5\,\text{kHz}$ is beyond the bandwidth ω_c ($1526\,\text{Hz}$) and cannot be attenuated by the baseline feedback loop. Also, the Nyquist frequency of $20\,\text{kHz}$ is large enough to obtain the frequency response of the system at 5 kHz. Substituting $\alpha = 0.9$ into (5.12) gives

$$Q(z) = \frac{0.01 - 0.1414z^{-1}}{1 - 1.273z^{-1} + 0.81z^{-2}}. \tag{5.25}$$

As shown in Fig. 5.15, the control effort with the Q-filter is larger than that with the baseline controller. The disturbance is attenuated remarkably with the outer-loop inverse-based YK parameterization turned on. The performance gain is also clear in the frequency domain that as shown in Fig. 5.16, the spectral peak at 5 kHz is completely removed without visible amplification of disturbances at the other frequencies.

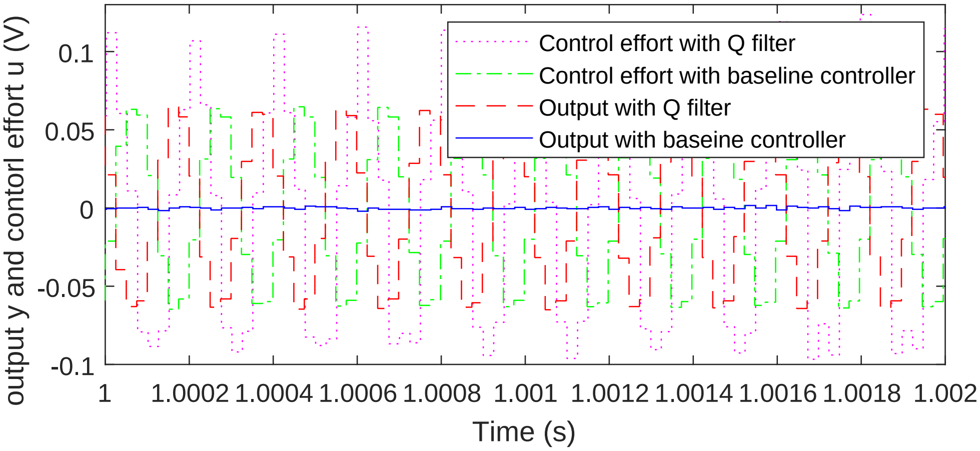

Figure 5.15: System outputs and control efforts with/without YK parameterization.

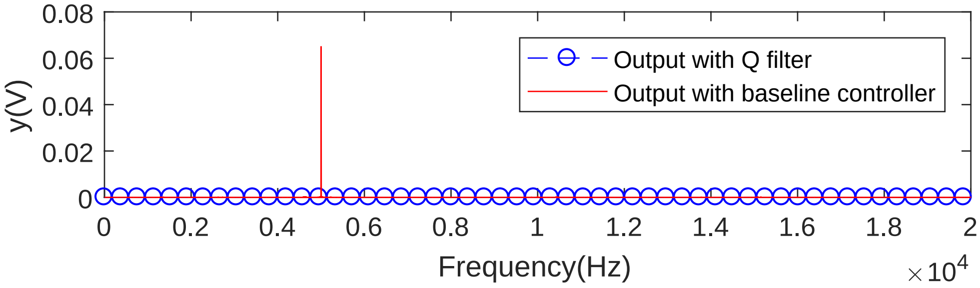

Figure 5.16: Spectrum of output $y(k)$.

Here are some remarks about the implementation of the loop-shaping method.

The plant model and its inverse: The (inverse) model information is essential in the discussed control schemes since it not only provides convenience for feedback design but also is beneficial for tasks such as fault detection and disturbance isolation. Such a model is usually available in industries. By the physical construction, the input to actuators in a precision positioning system is usually a voltage/current signal that is approximately linear with respect to motor torque, and the measurement is commonly an angular or linear position. The inverse system dynamics thus usually has a double-differentiator type of frequency response due to Newton's law. It is thus not difficult to obtain a stable nominal $\hat{P}^{-1}(z)$ that accurately presents the low-frequency dynamics.[4] Direct differentiation at high frequencies is not practical due to high-frequency resonances. High-frequency unstable zeros, if any, can be addressed by, for instance, shifting them inside the unit circle. A more systematic model inversion technique will be presented in Chapter 7.

Robust stability: Strictly speaking, after $\hat{P}$ is applied in the controller design, we are implementing a robust version of YK parameterization. Notice that in the examples in Figs. 5.6 and 6.4, the Q-filters are designed such that their magnitudes are small at high frequencies, namely, the loop behavior at ultra-high frequencies does not change. This is important for implementation, since it is practically impossible to have an exact mathematical model for mechanical systems. The robust stability analysis can give us upper bounds of the plant uncertainties for the closed-loop system to maintain stable. Intuitively, flexible loop shaping can be readily achieved at frequency regions where the model $\hat{P}^{-1}(z)$ accurately reflects the actual system dynamics. At high frequencies where the plant behavior itself cannot be well predicted, the magnitude of $Q(z)$ (and hence the add-on control efforts) is recommended to be kept small for robust stability.

Feedforward control: The feedback perspective for precision servo has been discussed. Necessity of feedforward control comes from the simple fact that feedback designs have bandwidth limitations. In the feedforward class of control algorithms, model-based design is also of essential importance. Inverse complementary sensitivity and inverse plant dynamics are two common approaches for feedforward design. When the process is repetitive, ILC is another powerful tool for error correction in the iteration domain.

Adaptive configuration: When the disturbance spectra is not known (but with known structure), adaptive control can be applied to update the parameters of $Q(z)$ online. Investigation for the case of narrow-band disturbance rejection is provided in the references [49, 64].

Reference of YK parameterization: For additional materials about YK parameterization, readers can refer to references [41, 51, 65]. In the discrete-time case, the simplest example of Q design is using $Q(z) = \theta_0 + \theta_1 z^{-1} + \theta_2 z^{-2} + ... + \theta_{k_Q} z^{-k_Q}$, namely, a finite impulse response filter and then applying parameter adaptation algorithms to find a set of θ_i that minimizes the feedback error. This idea is also used in adaptive inverse control [66].

---

[4] Friction can also be approximated by a second-order mode with damping and spring.

Chapter 6

FRACTIONAL-ORDER REPETITIVE CONTROL

6.1 Introduction

Repetitive control (RC) [67] is designed to track/reject periodic exogenous signals in applications with repetitive tasks, as mentioned in Section 5.3.3. By learning from memories of previous iterations in the repetitive task, RC can drastically enhance current control performance in the structured task space. Application examples include tracking controls in magnetic and optical disk drives [68, 69], wafer scanners [70], and robotic manipulators [71, 72], as well as regulation controls in wind turbines [73, 74], power converters [75], and unmanned aerial vehicles [76].

This chapter studies RC in LPBF process (see, e.g., Figs. 1.1 and 1.2) that contains highly repetitive thermomechanical interactions [77–79]. As a result, periodic errors are introduced in the laser-material interaction and path planning. Indeed, such periodicity has been validated and leveraged upon to improve control processes in other laser-based AM technologies [80–82]. To fully release the capability of RC to fundamentally improve the repetitive laser scanning in LPBF AM, the internal model principle [83, 84] must be carefully configured in the control design. In digital RC, an internal model $1/(1-z^{-N})$ is implemented in the controller, where N is the period of the disturbance/reference. N equals the sampling frequency (denoted in this dissertation as $1/T_s$ or f_s) divided by the fundamental frequency (f_0) of the periodic signal. When N is an integer, the repetitive controller can generate high gains at the fundamental frequency and its harmonics, yielding small gains in the error-rejection dynamics to create the desired servo performances. When f_s is not divisible by f_0, that is, N is not an integer, RC with the rounded N cannot target the aimed harmonic frequencies exactly, resulting in degraded performances.

Several strategies exist to potentially address problems related to fractional-order periods in RC. [55] and [85] introduce high-order repetitive controllers with delay elements to widen the high-gain regions around the harmonic frequencies. [86], [87], and [88] employ spatial repetitive controllers in a spatial domain to obtain time-invariant disturbance periods. [89] and [90] propose adaptive RC schemes where the sampling rate is adjusted adaptively to get an integer N. [91] proposes a delay-varying repetitive controller that uses knowledge of the repetitive variable to continuously adjust the time-varying delay. [75], [92], and [93] design different filters to approximate the fractional orders of delays. [94] uses a correction factor to correct the deviated poles of the fractional-order repetitive controller.

Despite the existing literature, it remains not well understood how to create RC *exactly* at the harmonic frequencies in the presence of fractional-order periods and how to systematically analyze the closed-loop performances. To bridge these knowledge gaps, this chapter aims at generating enhanced control efforts exactly at desired frequencies in the fractional-order RC. The main result is the development of a multirate RC algorithm and two indirect RC schemes. First, a wide-band RC is achieved by applying the nearest integer of N while widening the attenuation width of each frequency notch in the error-rejection dynamics. In the second indirect RC, a fictitious fundamental frequency is introduced to get an integer N, which creates an overdetermined rejection of the original repetitive errors. The proposed new multirate RC designs the internal model under a second divisible fast sampling frequency $f_s^{'}$ such that $N = f_s^{'}/f_0$ is an integer, and embeds a new zero-phase low-pass filter design to address multirate closed-loop robustness.

Along the course of formulating the multirate RC, an unexpected selective loop-shape modulation is discovered in the intrinsic multirate digital control design. This fundamental behavior, prone to be neglected in the design phase, inspires in the first instance a closed-loop analysis method that exhibits the complete disturbance-attenuation properties of the multirate RC. This analysis method also enables a new design space for applying RC to general systems with mismatched sampling and task periodicity. The remainder of this chapter will discuss the theoretical benefits, implementation guidance, and performance comparison of the proposed algorithms. Theoretical analyses are verified by a case study on a galvo scanner in LPBF.

The remainder of this chapter is structured as follows. Section 6.2 reviews an RC design. Two examples in Section 6.3 elucidate the existence of fractional-order disturbances in LPBF. Section 6.4 builds the proposed fractional-order RC algorithms. Section 6.5 provides the numerical and experimental verification of the algorithms.

6.2 Preliminaries of Repetitive Control

The proposed fractional-order RC algorithms are based on a plug-in RC design in Fig. 5.3 [70]. Consider a baseline feedback system composed of the plant $P(z)$ and the baseline controller $C(z)$ (Fig. 5.3 without the dotted box). $C(z)$ can be designed by means of common servo algorithms, such as PID, H_∞, and lead-lag compensation. The signals $r(k)$, $e(k)$, $d(k)$, and $y_d(k)$ represent, respectively, the reference, the tracking error, the input disturbance, and the system output. Throughout the chapter, it is assumed that 1) the coefficients of all transfer functions are real; 2) both $P(z)$ and $C(z)$ are rational, proper, linear, and time-invariant; 3) the baseline feedback loop consisting of $P(z)$ and $C(z)$ is stable.

The plug-in compensator utilizes the internal signals $e(k)$ and $u_d(k)$ to generate a compensation signal $w(k)$. Let m denote the relative degree of $P(z)$, whose nominal model is $\hat{P}(z)$. With the plug-in compensator, the transfer function of the overall controller from $e(k)$ to $u_d(k)$ is (5.5)

If $Q = (1-\alpha^N)z^{m-N}/(1-\alpha^N z^{-N})$, that is,

$$1 - z^{-m}Q(z) = \frac{1-z^{-N}}{1-\alpha^N z^{-N}}, \tag{6.1}$$

where $\alpha \in [0,\,1)$ is a tuning factor that determines the attenuation bandwidth of $1-z^{-m}Q(z)$, then at the harmonic frequencies ($\omega_k = k2\pi f_0 T_s$, $k \in \mathbb{Z}^+$, the set of positive integers), the magnitude responses of $1-z^{-m}Q(z)$ are zero because $1-\mathrm{e}^{-j\omega_k N} = 1-\mathrm{e}^{-jk2\pi f_0 T_s/(f_0 T_s)} = 1-\mathrm{e}^{-jk2\pi} = 0$. Hence, $|C_{all}(z)| \to \infty$ and $G_{d\to y_d}(z) = \frac{P(z)[1-z^{-m}Q(z)]}{1+P(z)C(z)} = 0$ when $z = \mathrm{e}^{j\omega_k}$. At the intermediate frequencies, $Q(\mathrm{e}^{j\omega}) \approx 0$, and $|1-z^{-m}Q(z)|_{z=\mathrm{e}^{j\omega}} \approx 1$ when α is close to 1; thus $C_{all}(z) \approx C(z)$, and the original loop shape is maintained. Choosing a smaller α can yield a wider attenuation bandwidth, at the cost of deviating from the baseline loop shape, as shown in Fig. 6.4.

Note that for $Q(z)$ in (6.1) to be implementable, the disturbance period N should be greater than the relative degree m, which is commonly satisfied in sampled-data regulation control. For instance, in the multirate RC example in Section 6.5, $N = 40 > m = 3$. Indeed, since the closed-loop bandwidth (B_p) is designed to cover the fundamental disturbance frequency f_0 and B_p is no less than 10% of the Nyquist frequency ($f_s/2$) from principles of feedback design, common control practice thus renders $N = f_s/f_0$ to be greater than 20. That is, N is at least one order of magnitude larger than the relative degree of the plant model under principles of feedback design.

During implementation, zero-phase pairs $q_j(z^{-1})q_j(z)$ ($j \in \mathbb{Z}$) are additionally incorporated into $Q(z)$ for robustness against plant uncertainties at high-frequency regions:

$$Q(z) = \frac{(1-\alpha^N)z^{-(N-m)}}{1-\alpha^N z^{-N}} \prod_{j=0}^{M} q_j(z^{-1})q_j(z), \tag{6.2}$$

where $M \in \mathbb{Z}$ is determined according to the design requirements. For instance, the following design of $q_i(z)$ ($i \in \mathbb{Z}^+$) places four zeros of $Q(z)$ at $\mathrm{e}^{\pm j\Omega_i T_s'}$ to make its frequency response equal zero at Ω_i:

$$q_i(z) = \frac{1-2\cos(\Omega_i T_s)z + z^2}{2-2\cos(\Omega_i T_s)}. \tag{6.3}$$

$$q_0(z) = \frac{(1+z)^{n_0}}{2^{n_0}}, \quad i = 0. \tag{6.4}$$

Here, $n_0 \in \mathbb{Z}$ is the number of the added zero pairs at the Nyquist frequency (Fig. 6.1). Note that the Q-filter in (6.2), (6.3), and (6.4) is designed assuming an integer N under the sampling time of T_s.

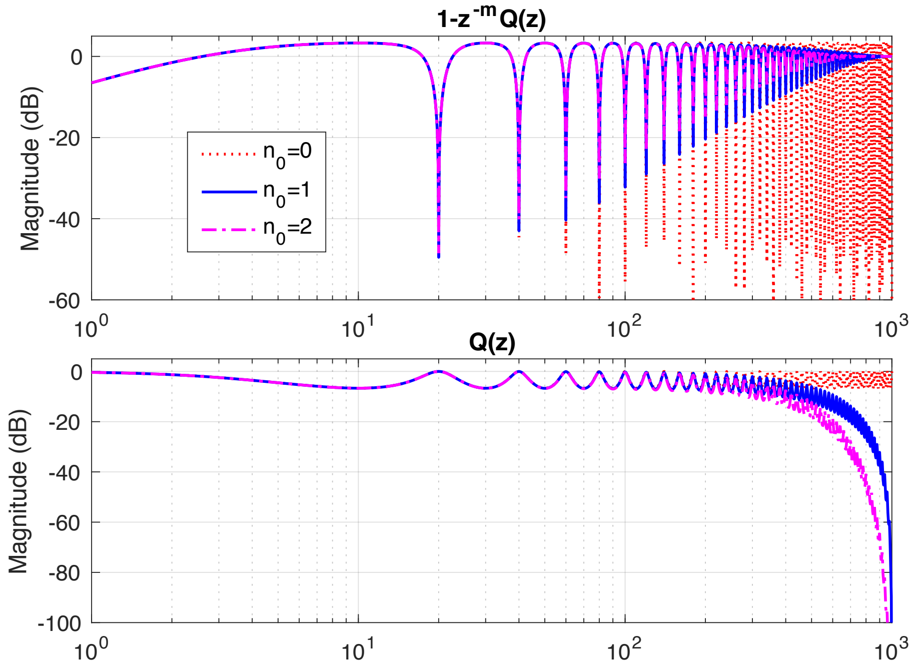

Figure 6.1: Magnitude responses of $1-z^{-m}Q(z)$ and $Q(z)$ with different n_0 (and $\alpha = 0.99$) in an example of Chapter 9. x-axis denotes frequency in Hz.

6.3 Fractional-order Disturbances in LPBF

This section motivates and justifies the application of fractional-order RCs to the field of LPBF. In the first example, fractional-order disturbances are observed to arise from the laser scanning mechanism, that is, the galvo scanner system. Based on the periodic thermal cycles during the LPBF process, the second example verifies the existence of the fractional-order disturbances.

6.3.1 Collaborative Control in Galvo Scanner

The dual-axis galvo scanner in Fig. 5.9 is a key component in LPBF for laser path planning. Typically, the dual-axis galvo scanner consists of two sets of mirrors, motors, and control systems, here referred to as the X channel and the Y channel, respectively. With the collaborative rotation of the two mirrors, the input laser beam is reflected to generate a predefined scanning trajectory at high speed with high precision. The rotation angles of the mirrors are measured by encoders mounted coaxially with the motor shaft in the scanner enclosure.

In practice, periodic disturbances appear in the dual-axis galvo sets. First, examine one single channel (e.g., Y channel) with a simple harmonic signal $A\sin(2\pi f_0 t + \phi)$. Frequency spikes at odd multiples of f_0, instead of a single spike at f_0, show up in the FFT of the channel output (Fig. 6.2). This is because signal conditioning boards in the servo driver limit the rate of change in the output signal when the slope of the input signal is faster than the predefined slew rate [95]. The slewed output waveform is thus not a pure sine waveform and results in harmonics at odd multiples of the fundamental frequency.

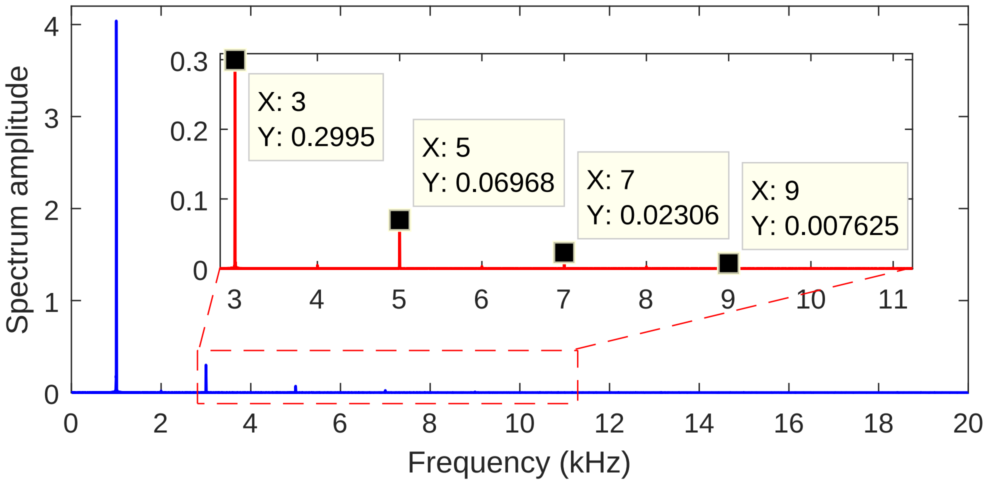

Figure 6.2: (Experimental result) FFT of the Y output with a simple harmonic input.

Second, the collaborative control of the two channels also introduces periodic disturbances. The mechanical motion of one rotating mirror can transmit to the other mirror as disturbances. In addition, high currents in the ground lines of the two servo drivers can cause the channels to crosstalk [96]. When actuating one channel with a simple harmonic signal at f_0, the FFT of the non-actuated channel output was observed to contain a frequency spike at f_0 caused by mechanical vibrations and frequency spikes at $2nf_0$ ($n \in \mathbb{Z}^+$) due to crosstalk. Numerically, if the Y channel is driven with a sine wave at 600 Hz and the X channel has no input, frequency spikes at 1200 Hz, 2400 Hz, 3600 Hz, etc arise at the FFT of the X output when the crosstalk is unaccounted for. The crosstalk is more obvious with increased amplitudes A and frequencies f_0 of the input signals (Fig. 6.3).

For both single- and cross-channel disturbances, the disturbance frequencies vary with the input signal frequencies and are not guaranteed to divide the sampling frequency of the galvo scanner. For instance, when $T_s = 1/16\,\text{ms}$, conventional RC fails in eliminating the crosstalk-induced harmonics at $\{1200i\,\text{Hz}\}$ ($i \in \mathbb{Z}^+$) since $N = 16000/1200$ in the internal model is not an integer. Without loss

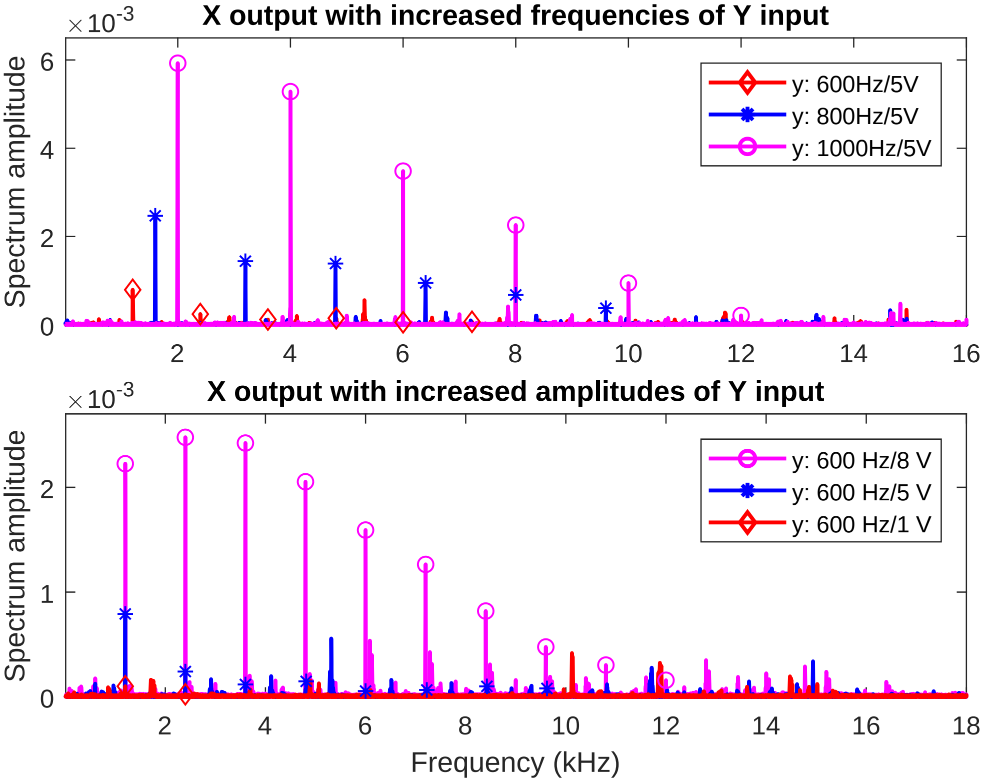

Figure 6.3: (Experimental result) FFT of the X output with increased frequencies and amplitudes of Y input.

of generality, in this dissertation, the proposed fractional-order RC algorithms are evaluated on the dual-axis galvo scanner as a case study to reduce the channel crosstalk.

6.3.2 Periodic Thermal Cycles in LPBF

The LPBF is built upon repeated scanning of laser beam on a bed of powder feedstock. The scan trajectories determine the periodicity of the laser-material interactions (see, e.g., Fig. 1.2). Here, the laser beam melts the powder material following predefined tracks, and monitoring sensors, such as cameras and imaging systems, are applied to obtain the melt pool information. To get a uniform part quality, the melt pool width is desired to be kept at a user-defined reference value [17]. On the one hand, periodic disturbances are introduced into the LPBF process by the complex, repetitive thermomechanical interactions, as shown in Section 3.3. On the other hand, because vision sensors are restricted in changing sampling rates, the disturbance frequencies, defined by laser path plannings, cannot always divide the sampling frequencies of the monitoring sensors.

In the sample simulation in Section 3.3.2, period $N(= f_s/f_0 = 2000/20 = 100)$ is an integer because u_x/L divides $1/T_s$. However, the scan speed u_x and the track length L are tailored to the required energy density but not the speed of the monitoring sensors (which is restricted for cameras and general integrated imaging systems). For instance, if $T_s = 3\,\text{ms}$, $N = 1000/60$ will become a non-integer. Therefore, the disturbance periodicity—defined by the scan speed, the part geometry, and the laser path planning—has no guarantees to be an integer multiple of the sampling rate of the melt pool sensors. These fractional-order disturbances challenge conventional RC and demand new algorithmic designs for RC to maximize performance in LPBF.

6.4 Proposed Fractional-order RC Algorithms

Three algorithms are proposed to tackle a non-integer N in the RC internal model. Two indirect schemes, a wide-band RC and a quasi RC, are first explored. Then the analyses and applications of the main new multirate RC are developed. For concreteness, this section will use the collaborative control example in Sections 6.3.1 and 6.5 throughout the discussions and generalize the algorithms along the course of design and analysis.

6.4.1 Wide-band and Quasi Repetitive Control

The wide-band and quasi RC algorithms are two variants for directly applying the conventional RC in (5.5) and Fig. 5.3 to the fractional-order cases. Both of them are implemented at the baseline sampling time, namely, T_s. In the wide-band RC, N is rounded to the nearest integer. Thus, high-control gains are generated near the desired disturbance frequencies. To include these frequencies, the wide-band RC chooses a smaller α to widen the attenuation width of each frequency notch in $1-z^{-m}Q(z)$, as shown in Fig. 6.4. With α decreasing from 0.99 to 0.8, the magnitude response of $1-z^{-m}Q(z)$ in Fig. 6.5 (a zoom-in view of Fig. 6.4) decreases from $-1.7\,\text{dB}$ to $-13\,\text{dB}$ at $1200\,\text{Hz}$, yielding increased control efforts at the aimed frequencies. Although the wide-band RC cannot perfectly reject the aimed disturbances, attenuation can be achieved to some extent. As the attenuation width increases further, so does the amplification of intermediate frequencies due to the waterbed effect [97].

The proposed quasi RC designs an integer N by introducing a fictitious fundamental frequency that is the greatest common divisor (GCD) of the fundamental and the sampling frequencies, namely, $N = f_s/\text{GCD}(f_s, f_0)$ and $f_0^{'} = \text{GCD}(f_s, f_0) = f_s/N$. In the example from Section 6.5, with $T_s = 1/16\,\text{ms}$ and $f_0 = 1200\,\text{Hz}$, $N = 16000/\text{GCD}(16000, 1200) = 40$, and the fictitious fundamental

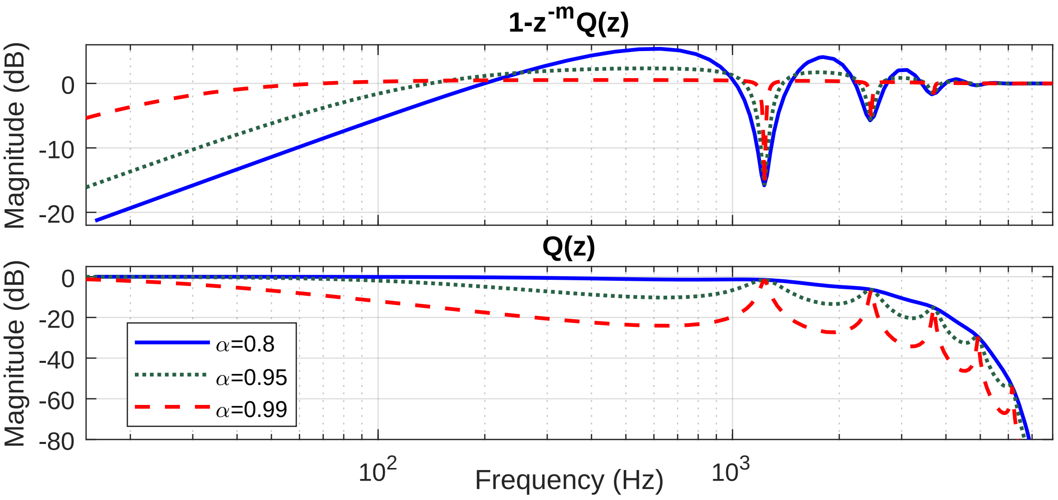

Figure 6.4: Magnitude responses of $1-z^{-m}Q(z)$ and $Q(z)$ in wide-band RC.

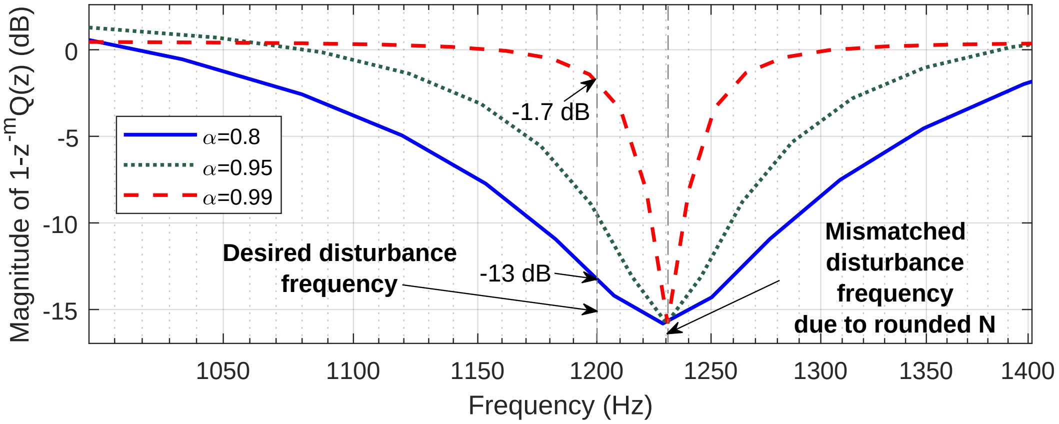

Figure 6.5: Zoom-in magnitude responses of $1-z^{-m}Q(z)$ in Fig. 6.4.

frequency f_0' is $16000/40 = 400\,\text{Hz}$. Quasi RC designed at $\{400i\,\text{Hz}\}$ $(i \in \mathbb{Z}^+)$ thus covers the desired harmonics at $\{1200i\,\text{Hz}\}$ $(i \in \mathbb{Z}^+)$ (with extra servo enhancement at $\{400i\,\text{Hz}\}$ $(i, k \in \mathbb{Z}^+ \,\text{and}\, i \neq 3k)$), as shown in Fig. 6.6. Note that f_0' must be applicable for the quasi RC to work. For an example of $f_0 = 1220\,\text{Hz}$, $f_0' = \text{GCD}(16000,\, 1220) = 20$, and the control efforts are largely wasted by generating high gains at many undesired frequencies at $\{20i\,\text{Hz}\}$ $(i, k \in \mathbb{Z}^+ \,\text{and}\, i \neq 61k)$).

Inheriting from the plug-in RC design, the stability conditions for the wide-band and quasi RCs are: $\hat{P}^{-1}(z)$, $Q(z)$, and $C(z)$ belong to the set of stable, proper, and rational transfer functions [98].

The wide-band RC and quasi RC are indirect solutions, only partially attenuating the disturbances.

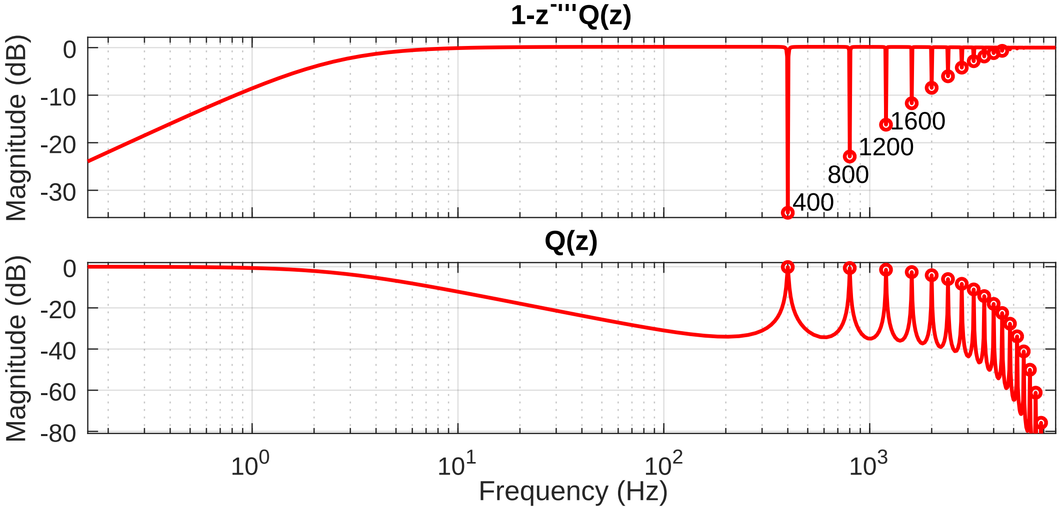

Figure 6.6: Magnitude responses of $1 - z^{-m}Q(z)$ and $Q(z)$ in quasi RC.

For applications that require stronger servo enhancement, more fundamental structural changes in the controller design will be discussed next.

6.4.2 Multirate Repetitive Disturbance Attenuation

The proposed multirate RC directly addresses the fractional-order period by introducing a second divisible sampling frequency $f_s^{'}$. Let $f_s^{'}$ equal the least common multiple (LCM) of the sampling and fundamental frequencies, namely, $f_s^{'} = \mathrm{LCM}(f_s, f_0)$. Without changing the sampling frequency of the plant, the multirate RC algorithm designs the repetitive controller with the internal model under the newly introduced fast sampling frequency. Since $N = f_s^{'}/f_0$ is now an integer, the multirate repetitive controller can thus generate high-gain control signals exactly at the fundamental frequency and its harmonics.

Consider first a multirate sampled-data regulation control in Fig. 6.7, where the solid and dashed lines represent the slow and fast signals sampled by T_s and $T_s^{'}(\triangleq 1/f_s^{'})$, respectively. $T_s^{'}$ and T_s are related by $T_s^{'} = T_s/F$ ($F > 1$ and $F \in \mathbb{Z}^+$). The main elements here include the plant $P(z)$, the controller $C_{dh}(z)$, the upsampler ↑ F, and the downsampler ↓ F. Based on multirate signal processing (see Appendix A.2), the frequency response of the equivalent feedback controller $C(z)$ in Fig. 6.7 is

$$C(\mathrm{e}^{j\Omega T_s}) = \frac{1}{F}\sum_{k=0}^{F-1} C_{dh}(\mathrm{e}^{j(\Omega T_s^{'} - \frac{2\pi k}{F})}). \tag{6.5}$$

The proposed multirate RC (Fig. 6.8) is configured by inserting the upsampling and downsampling

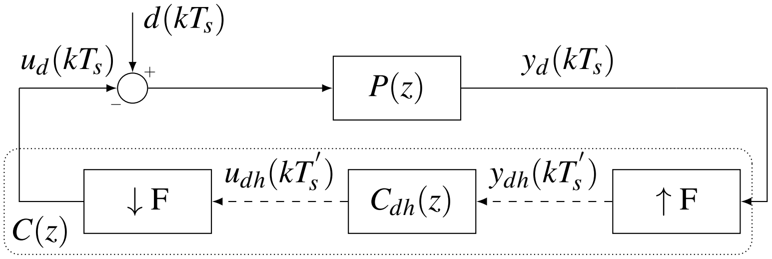

Figure 6.7: Block diagram for multirate sampled-data analysis.

blocks into Fig. 5.3 before and after the all-stabilizing controller.

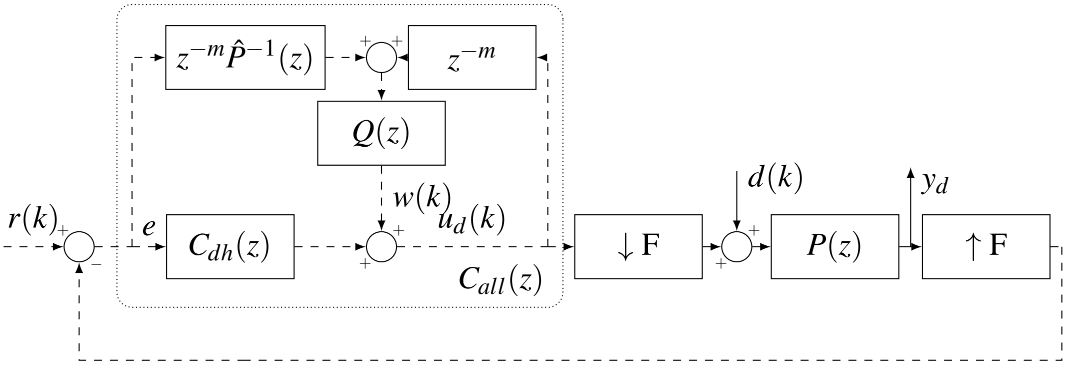

Figure 6.8: Block diagram for multirate RC.

The transfer functions inside the $C_{all}(z)$ block are implemented at $T_s^{'}$. With the plug-in RC applied on top of $C_{dh}(z)$, from (6.5), the frequency response of the open-loop transfer function from y_d to the summing junction before $P(z)$ is

$$\tilde{C}(e^{j\Omega T_s}) = \frac{1}{F}\sum_{k=0}^{F-1} C_{all}(e^{j(\Omega T_s^{'} - \frac{2\pi k}{F})}), \tag{6.6}$$

$$C_{all}(e^{j\Omega T_s^{'}}) = \frac{C_{dh}(e^{j\Omega T_s^{'}}) + e^{-jm\Omega T_s^{'}}\hat{P}^{-1}(e^{j\Omega T_s^{'}})Q(e^{j\Omega T_s^{'}})}{1 - e^{-jm\Omega T_s^{'}}Q(e^{j\Omega T_s^{'}})}. \tag{6.7}$$

Thus, when the reference $r(k)$ is zero (i.e., in regulation problems), block diagram manipulations in Fig. 6.8 give the Fourier transform of the plant output $y_d(k)$

$$\begin{aligned} Y_d(\mathrm{e}^{j\Omega T_s}) &= \frac{P(\mathrm{e}^{j\Omega T_s})D(\mathrm{e}^{j\Omega T_s})}{1+\frac{1}{F}P(\mathrm{e}^{j\Omega T_s})\sum_{k=0}^{F-1}C_{all}(\mathrm{e}^{j(\Omega T_s^{'}-\frac{2\pi k}{F})})} \\ &= \frac{P(\mathrm{e}^{j\Omega T_s})D(\mathrm{e}^{j\Omega T_s})}{1+P(\mathrm{e}^{j\Omega T_s})\tilde{C}(\mathrm{e}^{j\Omega T_s})}. \end{aligned} \tag{6.8}$$

Before discussing the detailed full multirate closed-loop properties, the authors provide a conceptual example and an overall disturbance-attenuation principle. Consider again $T_s = 1/16\,\text{ms}$ and $f_0 = 1200\,\text{Hz}$. Multirate RC gives $T_s^{'} = 1/\text{LCM}(16000,\ 1200) = 1/48\,\text{ms}$. The plug-in compensator is designed under the sampling time of $T_s^{'}$ such that small gains of $1-z^{-m}Q(z)$ are generated at the harmonic frequencies of $\Omega_0 = 2\pi n \times 1200\,\text{rad/s}$ ($n \in \mathbb{Z}^+$), as shown in Fig. 6.9. For disturbances at Ω_0, since the Q-filter design in Section 6.2 gives $C_{all}(\mathrm{e}^{j\Omega_0 T_s^{'}}) \to \infty$, the summation form of C_{all} in (6.6) also goes to infinity. Thus, in (6.8), $Y_d(\mathrm{e}^{j\Omega_0 T_s}) \to 0$, yielding $y_d(kT_s) = 0$ at Ω_0.

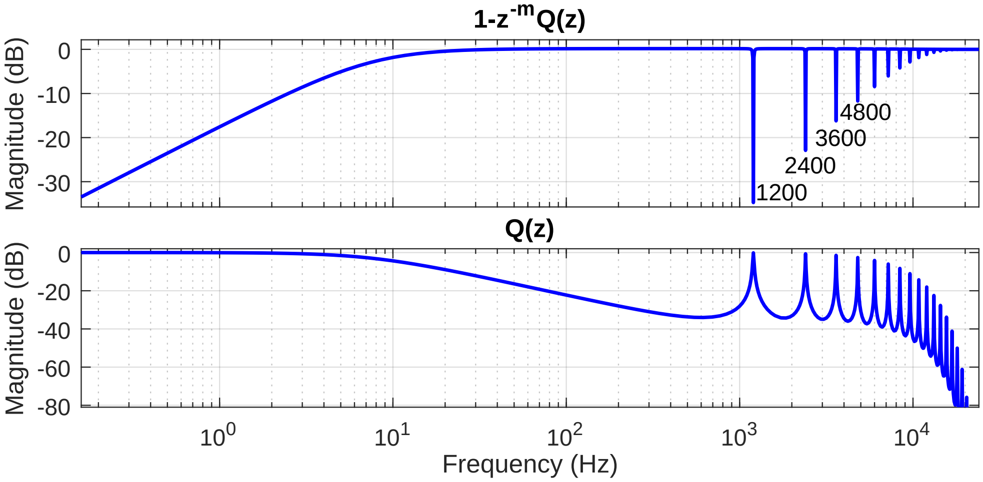

Figure 6.9: Magnitude responses of $1-z^{-m}Q(z)$ and $Q(z)$ in multirate RC.

Remark: The proposed algorithm targets exact transformation of the closed loop to formulate an integer parameter of the disturbance period in the internal model, and thereby generates high control gains exactly at the disturbance frequencies. As a trade-off, additional computation is required to facilitate the multirate signal processing. Under certain pairs of disturbance frequency and sampling rate of the system, previous approximate RCs may work more economically under the available computation budget. For instance, when $f_0 = 1199\,\text{Hz}$ and $T_s = 1/16\,\text{ms}$, then $\text{LCM}(1/T_s,\ f_0) = \text{LCM}(16000,\ 1199) = 1918.4\,\text{kHz}$ is orders of magnitude larger than the original sampling rate, resulting in high computation load that may be cost prohibitive on certain embedded platforms.

Multirate Closed-loop Analysis

In Fig. 6.8, the transfer function from the disturbance $d(k)$ to the output $y_d(k)$ equals $S(z) = S_0(z)P(z)$, where $S_0(z)$ is the closed-loop sensitivity function:

$$S_0(\mathrm{e}^{j\Omega T_s}) = \frac{1}{G(\mathrm{e}^{j\Omega T_s})}, \tag{6.9}$$

and

$$G(\mathrm{e}^{j\Omega T_s}) = 1 + \frac{1}{F}P(\mathrm{e}^{j\Omega T_s})\sum_{k=0}^{F-1} C_{all}(\mathrm{e}^{j(\Omega T_s^{'} - \frac{2\pi k}{F})}). \tag{6.10}$$

To reject disturbances at Ω_0, when the plant dynamics is fixed, $|S_0(\mathrm{e}^{j\Omega_0 T_s})|$ in the multirate RC is desired to be small at Ω_0, that is, $|G(\mathrm{e}^{j\Omega_0 T_s})| \rightarrow \infty$. With the direct Q-filter design under the sampling time of $T_s^{'}$ (Fig. 6.9), $|S_0(\mathrm{e}^{j\Omega T_s})|$ has the desired small gains at the target frequencies, as discussed in the paragraph after (6.8). However, small spikes also appear in $|S_0(\mathrm{e}^{j\Omega T_s})|$, that is, decreasing notches show up in $|G(\mathrm{e}^{j\Omega T_s})|$ (Fig. 6.10). The undesired selective small gains imply potential amplification of other error sources. The complete disturbance-attenuation properties of the proposed multirate RC will be deciphered next to assist in eliminating those error amplifications.

Note that $G(\mathrm{e}^{j\Omega T_s})$ in (6.10) contains hybrid frequency responses of $P(z)$ under the sampling time of T_s and $C_{all}(z)$ under $T_s^{'}$, and the frequency index satisfies the periodicity property:

$$\mathrm{e}^{j(\Omega T_s^{'} - \frac{2\pi k}{F})} = \mathrm{e}^{j(\Omega - \frac{2\pi k}{T_s})T_s^{'}} = \mathrm{e}^{j2\pi(f - \frac{k}{T_s})T_s^{'}}, \tag{6.11}$$

where $f = \Omega/(2\pi)$ is in Hz. Take the previous example ($T_s = 1/16\,\mathrm{ms}$, $T_s^{'} = 1/48\,\mathrm{ms}$, and $F = T_s/T_s^{'} = 3$). Then

$$G(\mathrm{e}^{j2\pi f T_s}) = 1 + \frac{1}{3}P(\mathrm{e}^{j2\pi f T_s})\sum_{k=0}^{2} C_{all}(\mathrm{e}^{j2\pi(f - \frac{k}{T_s})T_s^{'}}). \tag{6.12}$$

Let $G_k(\mathrm{e}^{j2\pi f T_s^{'}}) = 1 + P(\mathrm{e}^{j2\pi f T_s})C_{all}(\mathrm{e}^{j2\pi(f - \frac{k}{T_s})T_s^{'}})$. Then (6.12) is decomposed to

$$G(\mathrm{e}^{j2\pi f T_s}) = \frac{1}{3}\left[G_0(\mathrm{e}^{j2\pi f T_s^{'}}) + G_1(\mathrm{e}^{j2\pi f T_s^{'}}) + G_2(\mathrm{e}^{j2\pi f T_s^{'}})\right]. \tag{6.13}$$

With $\mathrm{e}^{j2\pi f T_s} = \mathrm{e}^{j2\pi(f - \frac{k}{T_s})T_s}$, the relationship between G_0 and G_1 is:

$$G_1(\mathrm{e}^{j2\pi f T_s^{'}}) = G_0(\mathrm{e}^{j2\pi(f - \frac{1}{T_s})T_s^{'}}), \tag{6.14}$$

and similarly

$$G_2(\mathrm{e}^{j2\pi f T_s^{'}}) = G_0(\mathrm{e}^{j2\pi(f + \frac{1}{T_s})T_s^{'}}). \tag{6.15}$$

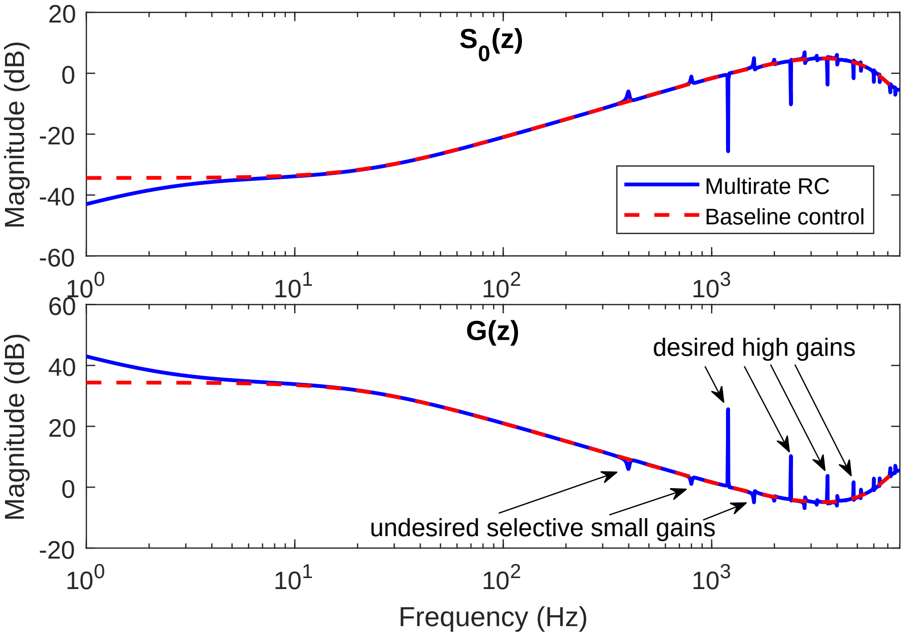

Figure 6.10: Frequency responses of $S_0(z)$ and $G(z)$ in Multirate RC with $T_s = 1/16\,\mathrm{ms}$, $T_s^{'} = 1/48\,\mathrm{ms}$, $F = 3$, and $f_0 = 1200\,\mathrm{Hz}$.

$G_1(\mathrm{e}^{j2\pi f T_s^{'}})$ and $G_2(\mathrm{e}^{j2\pi f T_s^{'}})$ are thus shifted versions of $G_0(\mathrm{e}^{j2\pi f T_s^{'}})$. Note $S_0(\mathrm{e}^{j2\pi f T_s})$ in (6.9) and $G(\mathrm{e}^{j2\pi f T_s})$ in (6.10) are evaluated from 0 to the slower Nyquist frequency corresponding to T_s, namely, $f \in [0, 8\,\mathrm{kHz}]$ in this example. Based on (6.14), $G_1(\mathrm{e}^{j2\pi f T_s^{'}})$ at $f \in [0, 8]$ kHz maps to $G_0(\mathrm{e}^{j2\pi f T_s^{'}})$ at $f \in [-16, -8]$ kHz, which is symmetric to $G_0(\mathrm{e}^{j2\pi f T_s^{'}})$ at $f \in [8, 16]$ kHz with respect to the line $f = 0$. Similarly, based on (6.15), $G_2(\mathrm{e}^{j2\pi f T_s^{'}})$ with $f \in [0, 8]$ kHz maps to $G_0(\mathrm{e}^{j2\pi f T_s^{'}})$ with $f \in [16, 24]$ kHz. Therefore, $G_0(\mathrm{e}^{j2\pi f T_s^{'}})$ evaluated at $f \in [0, 24]$ kHz (0 to $0.5/T_s^{'}$, the faster Nyquist frequency corresponding to $T_s^{'}$) includes all the desired information of $G_0(\mathrm{e}^{j2\pi f T_s^{'}})$, $G_1(\mathrm{e}^{j2\pi f T_s^{'}})$, and $G_2(\mathrm{e}^{j2\pi f T_s^{'}})$ under $f \in [0, 8\,\mathrm{kHz}]$, as shown in Fig. 6.11.

It can now be understood that because $G(\mathrm{e}^{j2\pi f T_s})$ in (6.13) is the average of $G_0(\mathrm{e}^{j2\pi f T_s^{'}})$, $G_1(\mathrm{e}^{j2\pi f T_s^{'}})$, and $G_2(\mathrm{e}^{j2\pi f T_s^{'}})$, the undesired small gains of $G(\mathrm{e}^{j2\pi f T_s})$ in the bottom plot of Fig. 6.10 are inherited from $G_1(\mathrm{e}^{j2\pi f T_s^{'}})$ and $G_2(\mathrm{e}^{j2\pi f T_s^{'}})$ or, equivalently, from $G_0(\mathrm{e}^{j2\pi f T_s^{'}})$ at frequencies larger than 8 kHz (Fig. 6.11).

It will be shown next that the undesired magnitude characteristics of $G_0(\mathrm{e}^{j2\pi f T_s^{'}})$ arise from an implicit model mismatch. Recall that

$$G_0(\mathrm{e}^{j2\pi f T_s^{'}}) = 1 + P(\mathrm{e}^{j2\pi f T_s})C_{all}(\mathrm{e}^{j2\pi f T_s^{'}}). \tag{6.16}$$

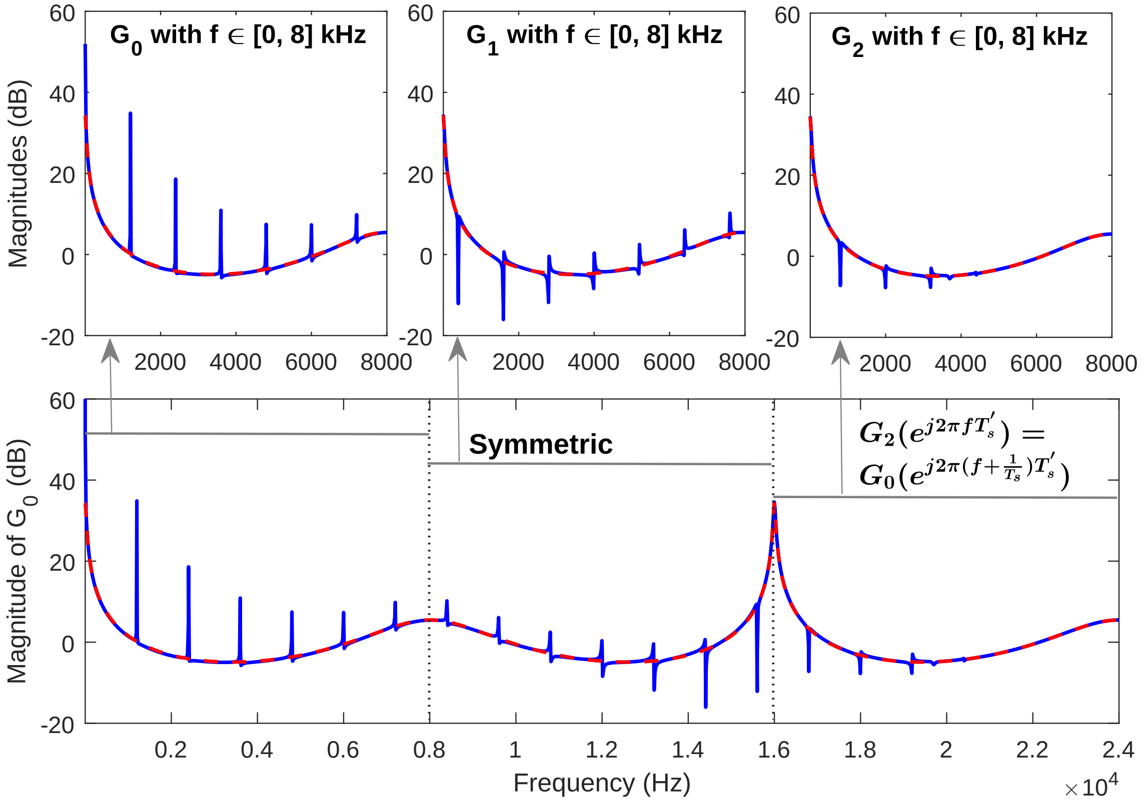

Figure 6.11: The relationships between $G_0(e^{j2\pi f T_s'})$, $G_1(e^{j2\pi f T_s'})$, and $G_2(e^{j2\pi f T_s'})$.

Substituting (6.7) into (6.16) gives

$$G_0(e^{j\Omega T_s'}) = \frac{[P(e^{j\Omega T_s})\hat{P}^{-1}(e^{j\Omega T_s'})-1]e^{-jm\Omega T_s'}Q(e^{j\Omega T_s'})}{1-e^{-jm\Omega T_s'}Q(e^{j\Omega T_s'})} + \frac{1+P(e^{j\Omega T_s})C_{dh}(e^{j\Omega T_s'})}{1-e^{-jm\Omega T_s'}Q(e^{j\Omega T_s'})}. \tag{6.17}$$

Fig. 6.12 presents the frequency responses of $P(e^{j\Omega T_s})$ and $\hat{P}(e^{j\Omega T_s'})$. At low frequencies, $P(e^{j\Omega T_s}) \approx P(e^{j\Omega T_s'}) \approx \hat{P}(e^{j\Omega T_s'})$, and (6.17) reduces to

$$G_0(e^{j\Omega T_s'}) = \frac{1+P(e^{j\Omega T_s})C_{dh}(e^{j\Omega T_s'})}{1-e^{-jm\Omega T_s'}Q(e^{j\Omega T_s'})}. \tag{6.18}$$

$G_0(e^{j\Omega T_s'})$ thus generates high gains where the magnitude responses of the denominator $1 - z^{-m}Q(z)$ are designed to be small (Fig. 6.9). At high frequencies, intrinsic model mismatches

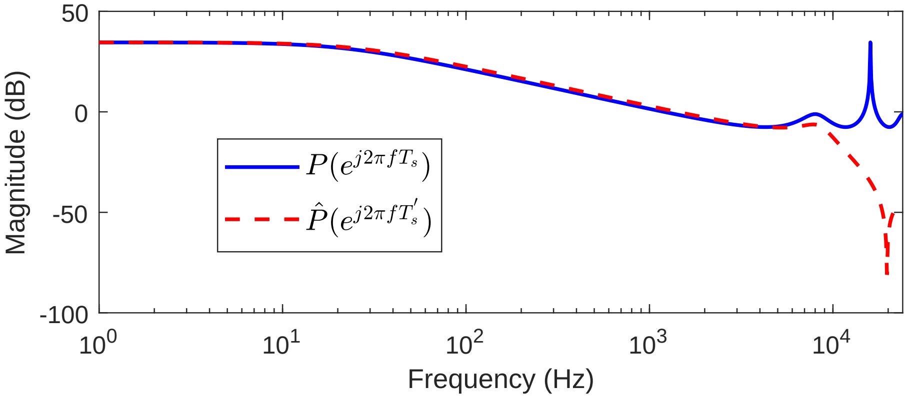

Figure 6.12: Magnitude responses of $P(\mathrm{e}^{j\Omega T_s})$ and $\hat{P}(\mathrm{e}^{j\Omega T_s'})$.

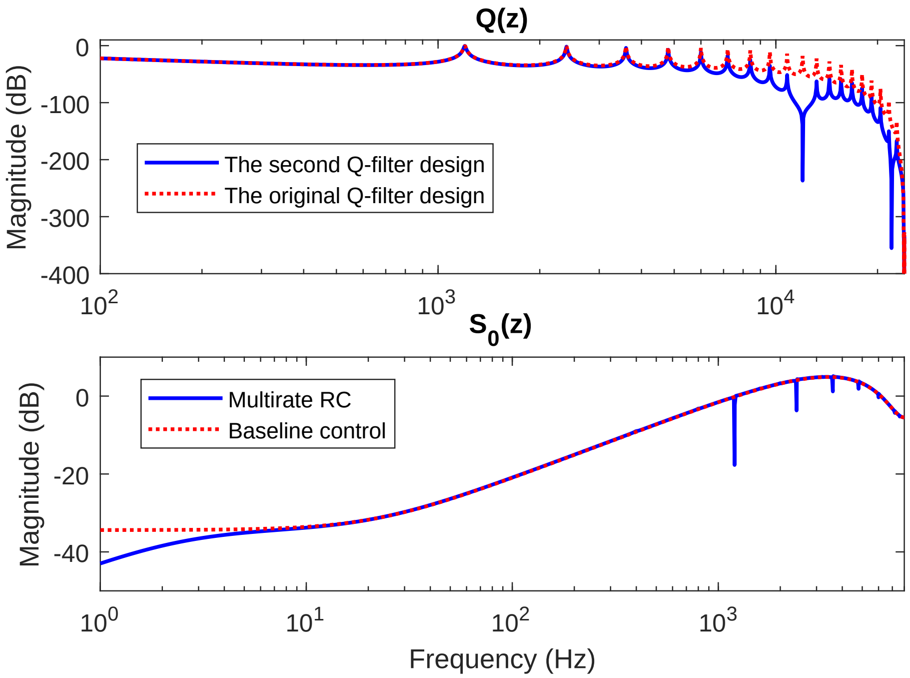

Figure 6.13: Magnitude responses of the second Q-filter design.

exist between $P(\mathrm{e}^{j\Omega T_s})$ and $\hat{P}(\mathrm{e}^{j\Omega T_s'})$ due to different sampling frequencies. Even though the magnitude response of $1-\mathrm{e}^{-jm\omega}Q(\mathrm{e}^{j\omega})\big|_{\omega=\Omega T_s'}$ is small, the first term of (6.17) must be carefully considered. To eliminate the undesired magnitude shapes, $Q(\mathrm{e}^{j\Omega T_s'})$ should be designed small enough at high frequencies to reduce the effect of the model mismatches in $[P(\mathrm{e}^{j\Omega T_s})\hat{P}^{-1}(\mathrm{e}^{j\Omega T_s'})-$

$1]\mathrm{e}^{-jm\Omega T_s^{'}} Q(\mathrm{e}^{j\Omega T_s^{'}})$.

Compared with the original Q-filter design used in Fig. 6.10, the multirate RC thus demands an enhanced design with reduced $Q(\mathrm{e}^{j\Omega T_s^{'}})$ at high frequencies (the top plot in Fig. 6.13). This second Q-filter is designed with $\alpha = 0.999$, $n_0 = 2$, $\Omega_1 = 2\pi \times (12\,\mathrm{kHz})$, and $\Omega_2 = 2\pi \times (22\,\mathrm{kHz})$ (see Section 6.2). As a result, in the multirate RC using the second Q-filter design, the undesired selective small gains of $|G_0(\mathrm{e}^{j2\pi f T_s^{'}})|$ disappear (the bottom plot of Fig. 6.14), which yields a clear magnitude response of the closed-loop sensitivity function with no visible error amplifications, as shown in the bottom plot in Fig. 6.13.

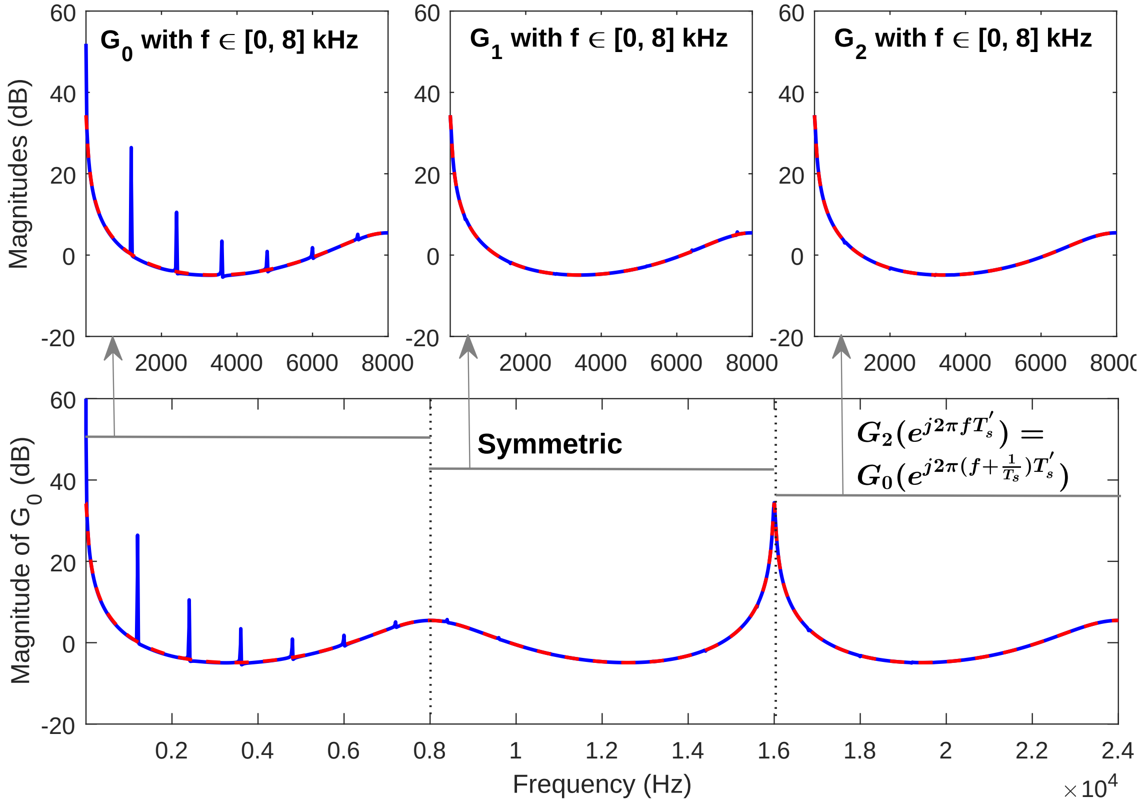

Figure 6.14: $G_0(\mathrm{e}^{j2\pi f T_s^{'}})$, $G_1(\mathrm{e}^{j2\pi f T_s^{'}})$, and $G_2(\mathrm{e}^{j2\pi f T_s^{'}})$ of the second Q-filter design.

For more general cases in the multirate RC, the analysis steps are:

1. Given f_s and f_0, identify the second sampling frequency $f_s^{'} = \mathrm{LCM}(f_s, f_0)$ for multirate RC design. Let $F = T_s/T_s^{'} = f_s^{'}/f_s$.

2. Design the repetitive controller in (6.7) under the deviated sampling frequency to get desired disturbance-attenuation properties.

3. Calculate and plot the closed-loop sensitivity function $S_0(\mathrm{e}^{j\Omega T_s})$ and $G(\mathrm{e}^{j\Omega T_s})$ in (6.9) to check if undesired selective small gains show up.

4. Look into $G_k(\mathrm{e}^{j2\pi f T_s'})$ $(k = 0, 1, 2, \cdots, F-1)$ with $f \in [0, f_s/2]$ to disentangle $G(\mathrm{e}^{j\Omega T_s})$ in the summation form. Since all $G_k(\mathrm{e}^{j2\pi f T_s'})$'s map into $G_0(\mathrm{e}^{j2\pi f T_s'})$, it suffices to analyze $G_0(\mathrm{e}^{j2\pi f T_s'})$ under $f \in [0, f_s'/2]$ to identify the frequencies of the undesired notches.

5. Redesign the Q-filter in the repetitive controller, and repeat steps 2–4 to reduce the undesired selective small gains until the design requirements are satisfied.

Stability and Robustness

For stability and robustness analysis, the second condition in Theorem 1 in Section 4.3.3 translates to $|\Delta(e^{j\Omega T_s})| < 1/|T(e^{j\Omega T_s})|$, where $T(z) = \frac{P(z)C(z)}{1+P(z)C(z)}$ is the complementary sensitivity function.

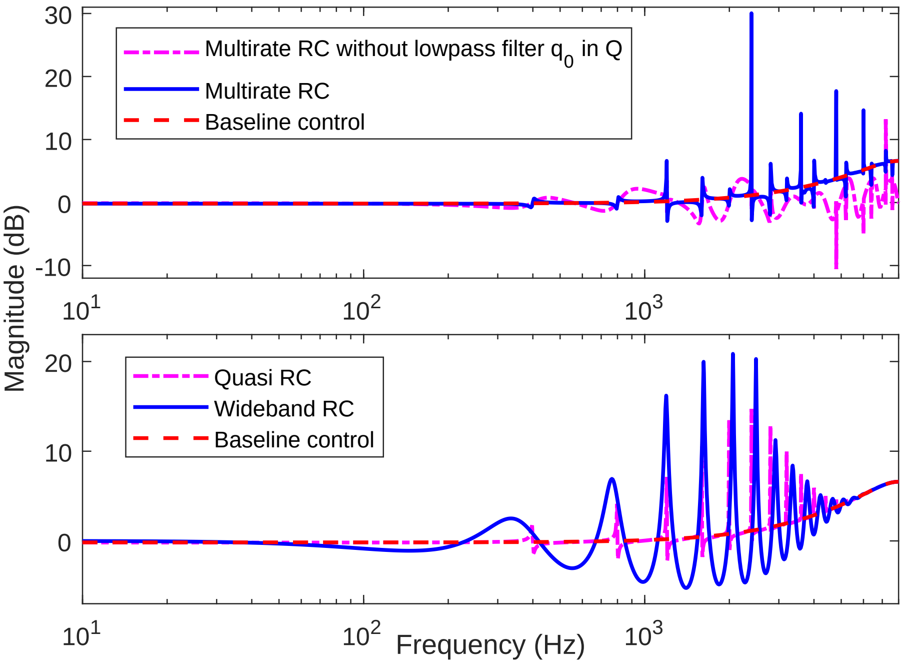

Figure 6.15: Magnitude responses of $1/T(z)$, which specify the upper bounds of the plant uncertainties to keep robustness.

Thus, $1/|T(e^{j\Omega T_s})|$ specifies the upper bound of the plant uncertainty at all frequencies. Fig. 6.15 shows the magnitude responses of $1/T(z)$ from the example in Section 6.5. Compared with the baseline control (PID control in this example), the introduction of the multirate RC extensively preserves and increases the robust stability bounds, especially at high frequencies. With the multirate RC (solid line in the top plot of Fig. 6.15), the minimal $1/|T(e^{j\Omega T_s})|$ is -2.9 dB at 1203 Hz, which requires the magnitude response of the uncertainty not to be greater than 71.6% of the magnitude response of the plant at this frequency. Without the lowpass filter $q_0(z^{-1})q_0(z)$ (dash-dot line in the top plot), the minimal $1/|T(e^{j\Omega T_s})|$ of the multirate RC decreases to -10.6 dB (29.5%) at 4801 Hz. Thus, the lowpass filter improves the robustness of the multirate repetitive controller.

The minimal $1/|T(e^{j\Omega T_s})|$ of the wide-band RC (solid line in the bottom plot) is -5.25 dB at 1404 Hz, that is, the uncertainty magnitude at this frequency should be less than 54.6% of the frequency response of the plant. In the quasi RC (dash-dot line in the bottom plot), the upper bound of the plant uncertainties is -2.16 dB (78%) (located at 1203 Hz). The quasi RC is more robust than the wide-band RC, although as shall be discussed in the next section, these two RCs have similar disturbance-attenuation performances.

6.5 Numerical and Experimental Verification in a Dual-axis Laser Galvo Scanner

This section provides implementation guidance and performance comparison of the theoretical analyses. As a case study, the proposed fractional-order RC algorithms are employed to reduce the crosstalk in the collaborative control of the galvo scanner (see Section 6.3.1).

To attenuate crosstalk-induced disturbances with fractional-order periods in the X channel, the wide-band, quasi, and multirate RC designs in Section 6.4 are implemented on top of the baseline X-channel controller.

The identified plant model with the sampling time $T_s^{'} = 1/48\,\text{ms}$ is

$$P^{'}(z) = \frac{0.061z^2 + 0.103z + 0.061}{z^5 - 1.485z^4 + 1.032z^3 - 0.433z^2 - 0.057z - 0.061}. \tag{6.19}$$

A stable plant model under the sampling time $T_s = 1/16\,\text{ms}$ is:

$$P(z) = \frac{0.061z^4 + 0.737z^3 + 0.351z^2 + 0.034z + 0.0001}{z^5 + 0.144z^4 - 0.773z^3 - 0.359z^2 - 0.034z - 0.0001}. \tag{6.20}$$

Fig. 6.16 shows the frequency responses of the measured and identified $P^{'}(z)$ of the X channel in (6.19).

The plant models already contain a factory built-in PID-type controller. The baseline feedback loop (Fig. 5.3 without the plug-in compensator) is thus designed under the sampling time of

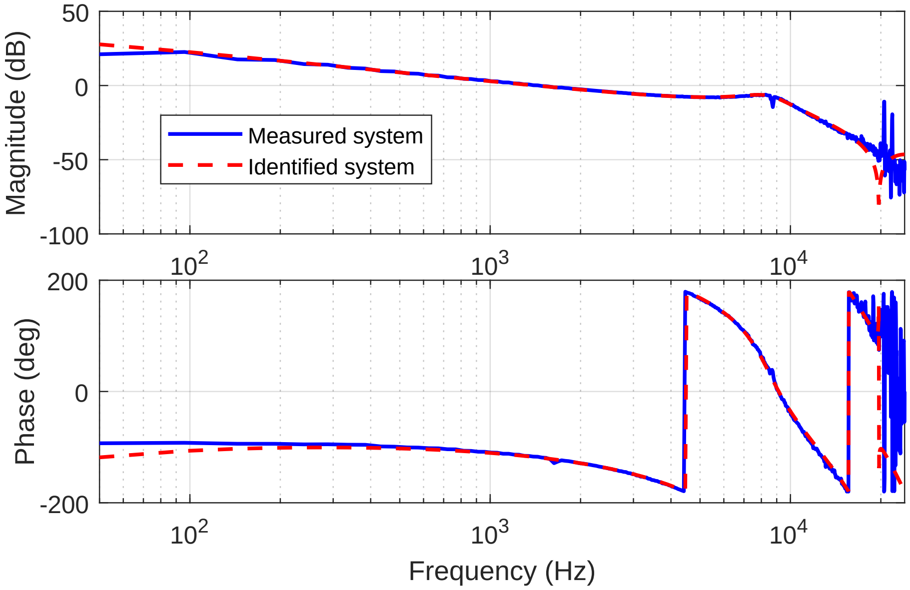

Figure 6.16: Bode plot of $P^{'}(z)$ sampled at $T_s^{'}$.

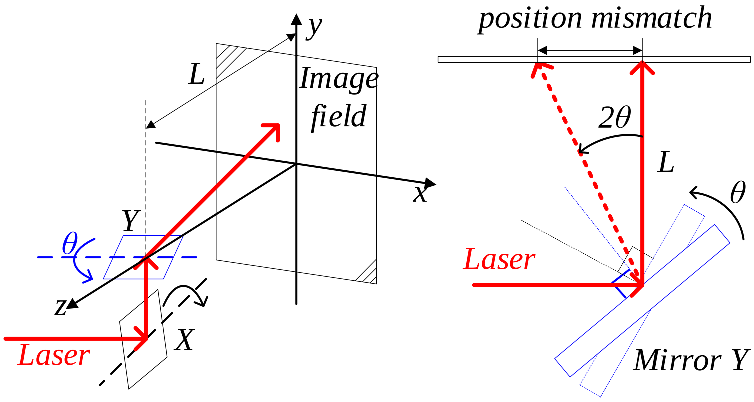

Figure 6.17: Schematic diagram of galvo scanner and position mismatch.

$T_s = 1/16\,\text{ms}$ by applying $P(z)$ in (6.20) and by letting $C(z) = 1$ (see Section 5.3 or [99]). Such a design provides a 4400 Hz bandwidth in the complementary sensitivity function $T(z)$. Throughout Sections 6.5.1 and 6.5.2, n_0 in (6.4) is chosen to be 3, and M in (6.2) equals zero.

6.5.1 Numerical Verification

In numerical verification, the same periodic disturbance with five frequency components is introduced into the X-channel loop (Figs. 5.3 and 6.8): $d(k) = A\sum_{n=1}^{5}\sin(2\pi n f_0 T_s k)$ with $A = 4\,\text{mV}$ (corresponding to $0.006°$ of the Y-channel mirror rotation) and $f_0 = 1200\,\text{Hz}$. As shown in Fig. 6.17, the position mismatch of the laser hitting the powder bed is $L\tan 2\theta = 1\text{m}\times\tan(2\times 0.006°)\approx 0.21\,\text{mm}$. When the length of the track to be sintered is 1 mm, this mismatch causes an error of 21%.

The dotted line in Fig. 6.18 presents the output of the baseline feedback loop in the time domain. Since the PID controller is generic and not tailored to the repetitive disturbance, the baseline controller barely attenuates the frequency spike at 1200 Hz and provides limited attenuation to the other four spikes (the top plot of Fig. 6.19). The wide-band and quasi RC algorithms are both implemented at the sampling time of $T_s = 1/16\,\text{ms}$, i.e. $f_s = 16\,\text{kHz}$. The relative degree of $P(z)$ in (6.20) is 1, that is, $m = 1$. In the wide-band RC, $N = \text{round}(f_s/f_0) = \text{round}(16000/1200) = 13$.

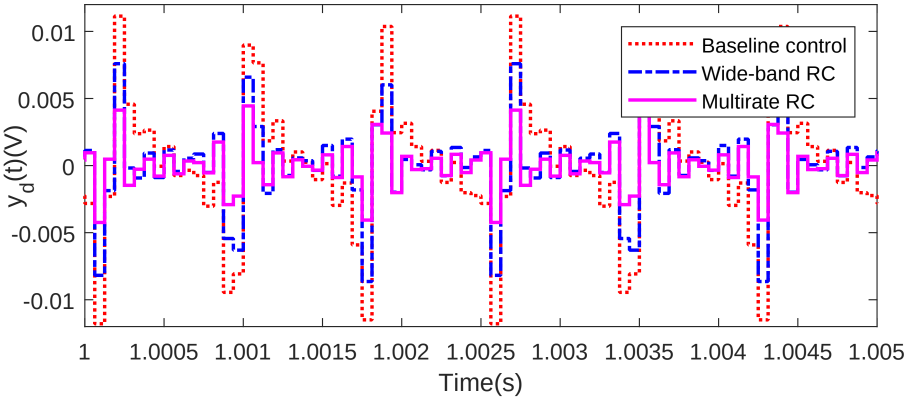

Figure 6.18: Plant outputs under baseline control, the proposed wide-band RC, and the proposed multirate RC.

Under this configuration, the frequency spikes the plug-in compensator targets are at $f_s/N = 1230.77\,\text{Hz}$ and its integer multiples. A wider attenuation width is needed in $1 - z^{-m}Q(z)$ to cover the adjacent harmonics at 1200 Hz, 2400 Hz, 3600 Hz, etc. To achieve this goal, α is set as 0.8, as shown in Fig. 6.4. In the quasi RC, the fictitious fundamental frequency is configured at 400 Hz such that $N = 16000/400 = 40$. Thus, the plug-in compensator generates high gains at 400 Hz and its integer multiples, covering the target frequencies $\{1200i\,\text{Hz}\}\,(i \in \mathbb{Z}^+)$. α is designed to be 0.999 to achieve good steady-state performance. The time-domain result of the quasi RC is similar to the wide-band RC result shown in the dash-dotted line in Fig. 6.18 and is omitted here.

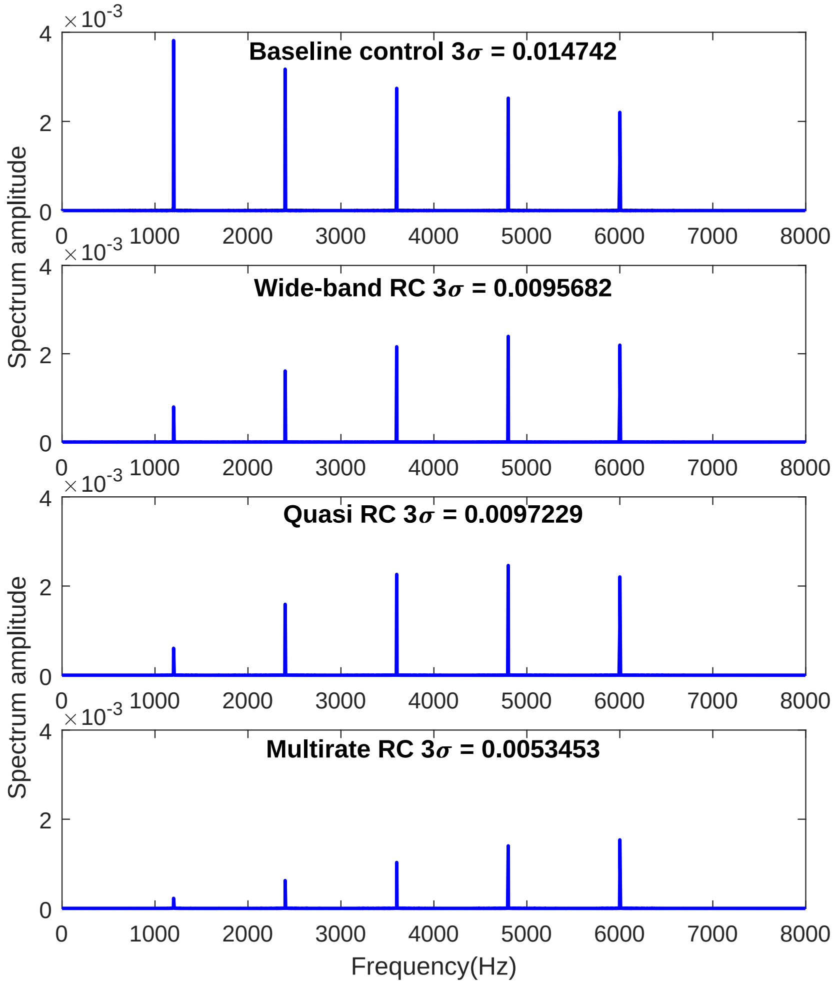

Figure 6.19: FFT of plant output sampled at T_s.

The time-domain outputs show that the wide-band and quasi RCs work better than the baseline control. The frequency-domain analysis in Fig. 6.19 further shows the first two frequency spikes are remarkably reduced compared with the baseline control. Due to the decreased control effort, the high-frequency spikes at 3600 Hz, 4800 Hz, and 6000 Hz remain largely unchanged.

In the multirate RC, the plug-in compensator is designed at $T_s^{'} = 1/48\,\text{ms}$ ($f_s^{'} = 48\,\text{kHz}$) with $F = T_s/T_s^{'} = 3$. The relative degree of $P^{'}(z)$ in (6.19) is 3 ($m = 3$). α is chosen to be 0.999 to reduce the waterbed effect. In this case, $N = f_s^{'}/f_0 = 48000/1200 = 40$. In Fig. 6.9, small gains of $1 - z^{-m}Q(z)$ are generated exactly at 1200 Hz and its integer multiples. The increased control efforts at high frequencies yield a further-attenuated output in the time domain (the solid line in Fig. 6.18) and in the frequency domain (the bottom plot of Fig. 6.19). Besides the attenuated low-frequency spikes, the peaks at 3600 Hz, 4800 Hz, and 6000 Hz are also largely reduced.

The numerical results of the four control systems are compared in Table 6.1. As a performance metric, for each control system, the 3σ value of the time-domain result is provided, where σ denotes the standard deviation. Compared with the baseline control, the application of the multirate, wide-band, and quasi RC algorithms decreases the 3σ values, thereby achieving the desired disturbance-attenuation effect. In more details, the wide-band and quasi RCs have similar performance, and the performance gains are 35% and 34%, respectively. The multirate RC outperforms the other two by reaching a 64% decrease of the 3σ value and reducing the laser point mismatch by one order of magnitude to $0.21 \times (1-64\%) \approx 0.075\,\text{mm}$. In the case of a 1 mm track, the sintering error reduces from 21% to 7%.

Table 6.1: Numerical and experimental results of the baseline control and the three proposed RC schemes. (N/A denotes "not applicable.")

		Baseline	Multirate	Wide-band	Quasi
Simulation	3σ	0.0147	0.0053	0.0096	0.0097
	Decreasing	N/A	64%	35%	34%
Experiment	3σ	0.0132	0.0045	0.0074	0.0071
	Decreasing	N/A	66%	44%	46%

6.5.2 Experimental Verification

Experiments are conducted on the galvo scanner platform in Fig. 5.9 to reduce the crosstalk in the collaborative control (see Section 6.3.1). Without loss of generality, the Y channel is run with a simple harmonic signal $A\sin(2\pi f_0 t + \phi)$ with $A = 8\,\text{V}$, $f_0 = 600\,\text{Hz}$, and $\phi = 0$. The periodic disturbance emerges on the output of the X channel, with frequency spikes at 1200 Hz, 2400 Hz, 3600 Hz, etc (the top plot in Fig. 6.20), as stated in Section 6.3.1. The baseline PID-type controller is unable to reduce the crosstalk between the X and Y channels (the dotted line in Fig. 6.21). The experimental and numerical results match well with each other. The output signals $y_d(t)$ in Fig. 6.21 show the clear performance difference of multirate RC>wide-band RC(≈quasi RC)>baseline control. Indeed, frequency-domain analysis reveals that the wide-band and quasi methods can reduce the first two but not other high-frequency spikes above 3600 Hz. The multi-rate RC algorithm, on

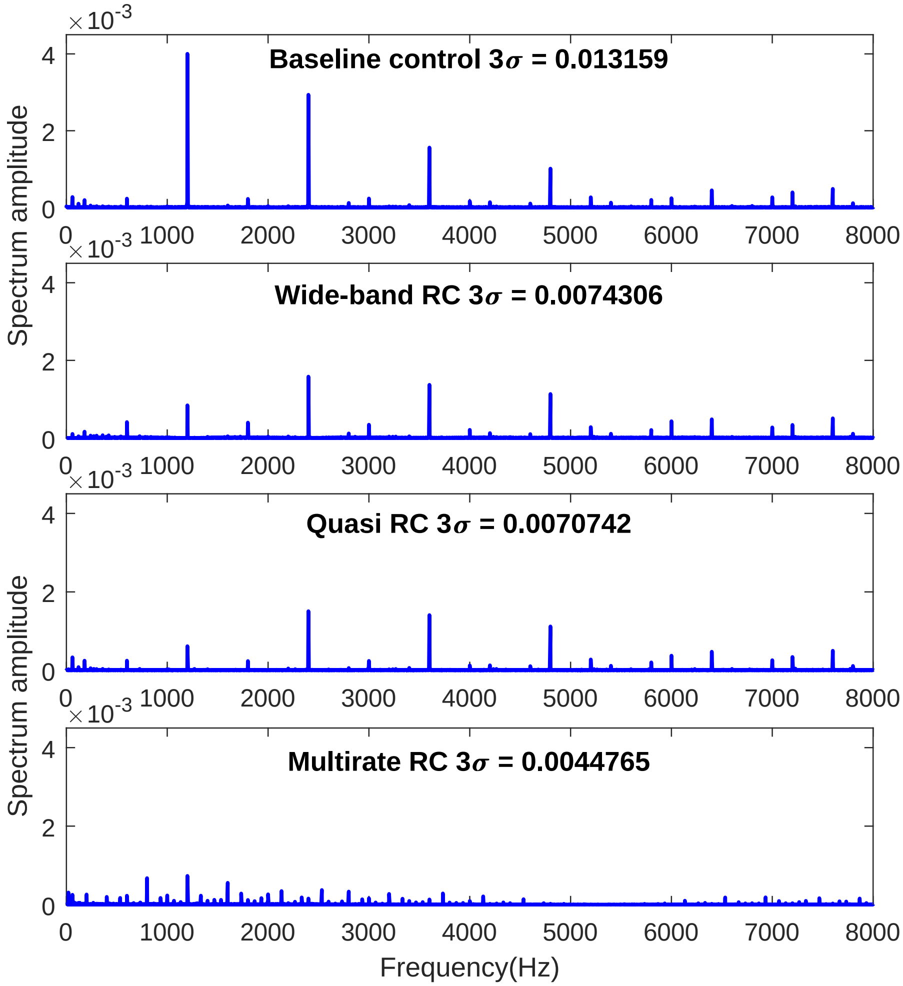

Figure 6.20: FFT of plant output sampled at T_s.

the other hand, can effectively attenuate the periodic frequency spikes appearing at $2nf_0$ ($n \in \mathbb{Z}^+$) by generating frequency notches in $1 - z^{-m}Q(z)$ and enhanced control efforts exactly at those frequencies.

The slight differences between the simulated and experimental results in Table 6.1 are caused by the different disturbance sources in the two cases. In simulations, the same amplitude is selected for the five introduced frequency spikes. In experiments, the disturbances induced by the crosstalk are different in amplitudes. For each spike, as the frequency increases, the amplitude decreases (Fig. 6.3).

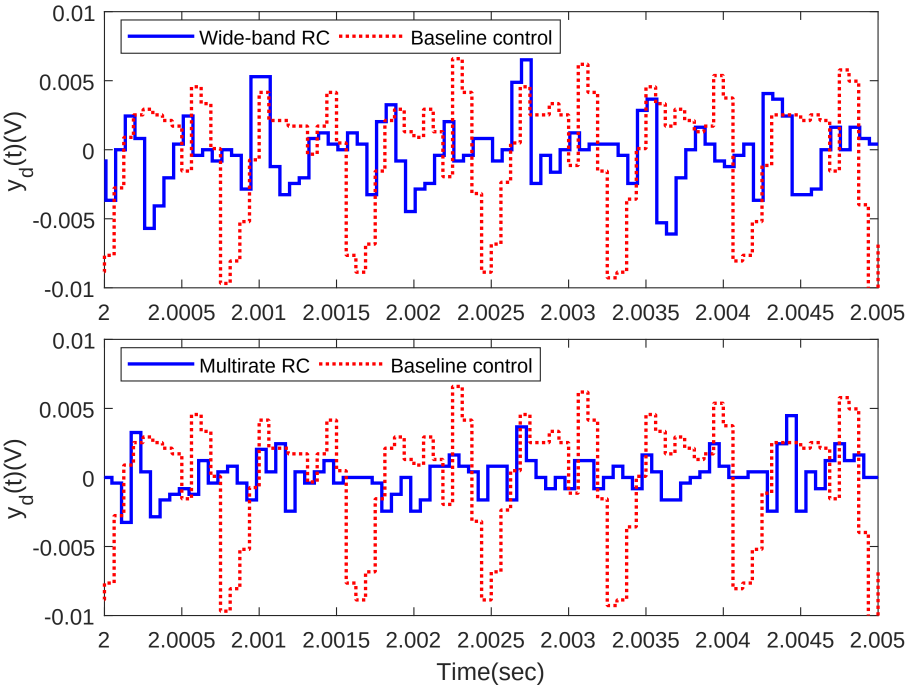

Figure 6.21: Plant output of baseline control, the proposed wide-band RC, and the proposed multirate RC.

Chapter 7

H_∞-BASED MODEL INVERSION

7.1 Introduction

Given a linear time-invariant system model G, the inversion of G has numerous practical applications including ILC [100–102], repetitive control [1, 103], two-degree-of-freedom servo in feedforward control [104, 105], as well as YK parameterization and DOB in feedback control [99, 106–109]. Here, G can be an open-loop plant model or a closed-loop control system. For a minimum-phase system, G^{-1} is stable and ready to be implemented. However, for a system with nonminimum-phase (NMP or unstable) zeros, G^{-1} is unstable and cannot be implemented directly. To find a stable, rational, and causal replacement $\hat{G}^{-1}$ such that $G\hat{G}^{-1}$ approximates 1 is thus a fundamental challenge in inversion-based control designs. Such a challenge is more pronounced in discrete-time systems since 1) integrator-type plant dynamics[1], common in motion control, generate NMP zeros in their ZOH equivalents when the sampling time is sufficiently small; 2) fractional-order delays induce unstable zeros after discretization [110].

Considering the importance and the challenge of model inversion, numerous strategies have been established in modern literature. Based on system representations and scopes of application, we can classify these strategies into two categories: frequency- and time-domain model inversions. The frequency-domain strategies focus on expressing the transfer functions of the stable inverses and hence can be used in both feedback and feedforward controls. Examples in this category include the approximate (e.g., NPZ-ignore, ZPETC, and ZMETC) [111–114], the ILC-based [115–117], and the H_∞-based [50, 118, 119] model inversions. On the other hand, the time-domain strategies [120–123] aim at identifying the optimal control signal that minimizes the error between a given reference and the output. These time-domain algorithms are mainly used as feedforward techniques since a preview of the reference is generally not available in feedback design.

This dissertation studies the analysis and design of model inversion strategies in the frequency domain. Current strategies in this category aim at achieving effective model matching between $\hat{G}$ and G. Compared with the approximate and the ILC-based model inversions, the H_∞-based

---

[1] When actuators take forces or torques as the input and linear/angular position as the output, integrator-type plant dynamics with a relative degree not less than two show up.

model inversion can automatically identify the inverse model without knowing the exact NMP zeros, which particularly benefits systems with complicated pole-zero distributions. However, when the inverses are to be implemented in feedback systems, additional considerations are needed for assuring closed-loop stability and robustness. In pursuit of bridging the gap between accurate model approximations and robust feedback performances, this dissertation builds a new H_∞-based optimal inversion algorithm that advances the field by 1) mitigating control efforts at customized frequencies and thereby enhancing system robustness; 2) reaching high efficiency for complex high-order systems and unstable systems.

Before presenting the main algorithm, we first provide a pole-zero-map-based NMP-zero modulation by replacing high-frequency NMP zeros with stable ones in motion control applications. We verify the feasibility and limit of this intuitive modulation in achieving a stable inverse model and meanwhile capturing the low-frequency system dynamics for high-performance motion control. Then we extend this intuitive modulation to an optimal design of model inversion. There, replacing the manual adjustment with an automatic and optimal search, we develop a new H_∞-based algorithm that can attain model accuracy at the frequency regions of interest while constraining noise amplification elsewhere to guarantee system robustness. The design goals are achieved by a multi-objective formulation and an all-pass factorization that consider model matching, gain constraints, causality of transfer functions, and factorization of unstable system modes in a unified scheme. The proposed algorithm is validated on motion control systems and complex high-order systems. Moreover, along the path, we unveil previously ignored features of existing inversion strategies by developing a general frequency-domain analysis method, which also gives new insights into comparing the performances of different strategies.

The main contributions of this chapter are:

1. conducting an up-to-date review of model inversion strategies and proposing a new frequency-domain analysis method;

2. analyzing the effect of an intuitive NMP-zero modulation and developing a new H_∞-based inversion algorithm;

3. validating the proposed algorithm by presenting detailed case studies with high-fidelity experimental data.

The remainder of this chapter is structured as follows. Section 7.2 conducts an in-depth review of literature and proposes the new frequency-domain analysis method. Section 7.3 elucidates the effect of modulating NMP zeros. The proposed optimal inversion is presented and verified in Section 7.4.

7.2 Review and Comparison of Frequency-domain Inversion Algorithms

The frequency-domain inversion algorithms aim at expressing the stable inverse models $F = \hat{G}^{-1}$ in the s- or z-domain. $\hat{G}$ is the minimum-phase system model that approximates G and has a stable inverse. An optimal inverse model is desired for $G\hat{G}^{-1}$ to approximate 1. In this section, we review and compare three typical types of frequency-domain inversion algorithms. In addition, we unveil new features of existing algorithms by developing a general frequency-domain analysis method.

7.2.1 H_∞-based Model Inversion

1) Algorithm

The model inversion problem for NMP systems has been solved using the H_∞ formulation [50, 118, 119]. For a continuous-time NMP system $G(s) = (b-s)/(b+s)$ with $b > 0$, under a cost function $J = ||W(s)(1 - G(s)\hat{G}^{-1}(s))||_\infty$, where the weighting $W(s) = (k+\xi s)/(k+s)$ is a low-pass filter with $k > 0$ and $0 \leq \xi < 1$, the optimal inverse of $G(s)$ that minimizes J is a lead filter [119]:

$$\hat{G}^{-1}(s) = \frac{k(1-\xi)(b+s)}{(k+b)(k+\xi s)} \tag{7.1}$$

that has high gains at high frequencies. The frequency response of the optimal $G(s)\hat{G}^{-1}(s)$ is

$$G(j\Omega)\hat{G}^{-1}(j\Omega) = \frac{k(1-\xi)(b-j\Omega)}{(k+b)(k+j\xi\Omega)}, \tag{7.2}$$

where Ω is in rad/s.

2) Frequency-domain Analysis

To quickly capture the essence of $G\hat{G}^{-1}$, we examine the frequency response of $G\hat{G}^{-1}$ at the two frequency endpoints (0 and ∞ for a continuous-time system or 0 and π in rad for a discrete-time system) and evaluate the characteristics of model matching.

Considering $b = 2$, $\xi = 0.3$, and different k's, we depict in Fig. 7.1 the frequency responses of (7.2). As Ω increases from 0 to ∞, the phase of $G(j\Omega)\hat{G}^{-1}(j\Omega)$ always goes from 0 to $-180°$ (the bottom plot of Fig. 7.1), and its magnitude goes from $b\left(\frac{1-\xi}{k+b}\right)$(<0 dB) to $\frac{k}{\xi}\left(\frac{1-\xi}{k+b}\right)$, monotonically. Therefore, depending on the values of k and ξ, $G(s)\hat{G}^{-1}(s)$ is a high-pass filter when $\frac{k}{\xi}\left(\frac{1-\xi}{k+b}\right) > b\left(\frac{1-\xi}{k+b}\right)$, i.e., $k > \xi b$ (0.6 in this example), a low-pass filter when $k < \xi b$, and has a constant magnitude when $k = \xi b$ (the top plot of Fig. 7.1).

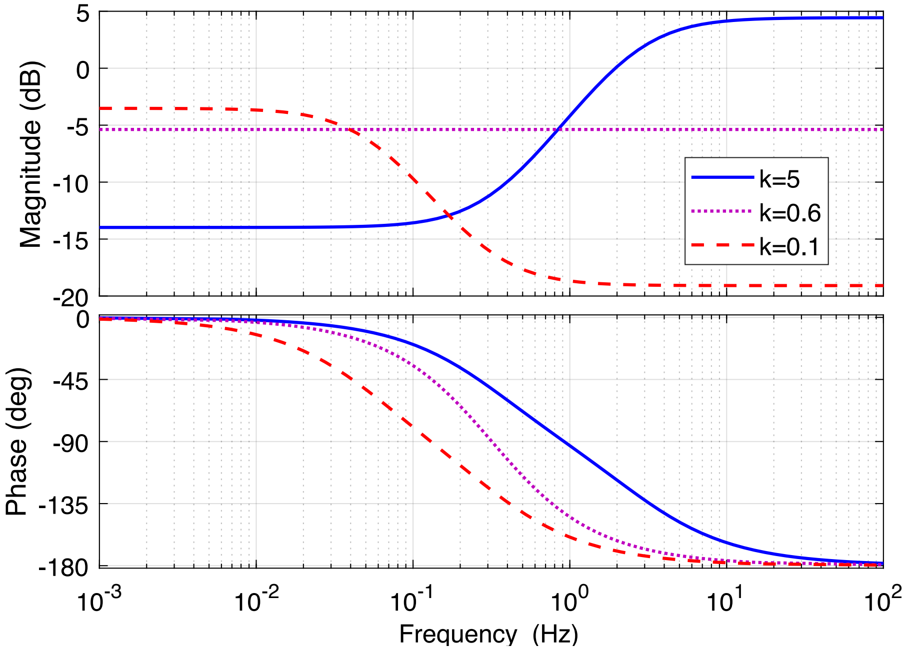

Figure 7.1: Frequency responses of $G(j\Omega)\hat{G}^{-1}(j\Omega)$ with $b=2$, $\xi=0.3$, and different values of k

7.2.2 Approximate Model Inversions

1) Algorithms

For discrete-time NMP systems, to obtain the basic structure of the inverse model, approximate model inversions [111–114] first factor out the unstable zeros of the system as

$$G(z)=\frac{N(z)}{D(z)}=\frac{N_s(z)N_u(z)}{D(z)}, \tag{7.3}$$

where $N(z)$ and $D(z)$ are coprime polynomials of z, and $N_s(z)$ and $N_u(z)$ contain, respectively, the stable and the unstable zeros. Here, we define $N_u(z)$ as

$$N_u(z)=(z-z_1)(z-z_2)\cdots(z-z_n), \tag{7.4}$$

where $z_1, z_2, \cdots, z_n$ are outside the unit circle. Note that

$$N_u(z^{-1})=(z^{-1}-z_1)(z^{-1}-z_2)\cdots(z^{-1}-z_n)$$

has stable zeros. In addition, $N_u(z)N_u(z^{-1})$ is zero-phase.

In the general case, the approximate inverse model of $G(z)$ in (7.3) has a structure of

$$\hat{G}^{-1}(z)=\frac{D(z)}{N_s(z)\tilde{N}_u(z)}, \tag{7.5}$$

Table 7.1: $\tilde{N}_u(z)$, $G(z)\hat{G}^{-1}(z)$, and $\frac{Y(z)}{R(z)}$ in approximate model inversions. $Y(z)$ and $R(z)$ are transfer functions of the output and reference signals shown in Fig. 7.2.

Methods	NPZ-ignore	ZPETC	ZMETC
$\tilde{N}_u(z)$	$N_u(1)$	$\frac{[N_u(1)]^2}{N_u(z^{-1})}$	$N_u(z^{-1})$
$G(z)\hat{G}^{-1}(z)$	$\frac{N_u(z)}{N_u(1)}$	$\frac{N_u(z)N_u(z^{-1})}{[N_u(1)]^2}$	$\frac{N_u(z)}{N_u(z^{-1})}$
$\frac{Y(z)}{R(z)}$	$z^{-m}\frac{N_u(z)}{N_u(1)}$	$z^{-m}\frac{N_u(z)N_u(z^{-1})}{[N_u(1)]^2}$	$z^{-m}\frac{N_u(z)}{N_u(z^{-1})}$
$\frac{Y(\mathrm{e}^{j\omega})}{R(\mathrm{e}^{j\omega})}$	$\mathrm{e}^{-jm\omega}\frac{N_u(\mathrm{e}^{j\omega})}{N_u(1)}$	$\mathrm{e}^{-jm\omega}\frac{N_u(\mathrm{e}^{j\omega})N_u(\mathrm{e}^{-j\omega})}{[N_u(1)]^2}$	$\mathrm{e}^{-jm\omega}\frac{N_u(\mathrm{e}^{j\omega})}{N_u(\mathrm{e}^{-j\omega})}$
$\left\lvert\frac{Y(\mathrm{e}^{j\pi})}{R(\mathrm{e}^{j\pi})}\right\rvert$	$\left\lvert\frac{N_u(-1)}{N_u(1)}\right\rvert$	$\left[\frac{N_u(-1)}{N_u(1)}\right]^2$	1

where $\tilde{N}_u(z)$ is a design parameter.

Table 7.1 summarizes three approximate model inversions with different designs of $\tilde{N}_u(z)$. The NMP zeros ignore method (NPZ-ignore) [113, 114] replaces $N_u(z)$ with $\tilde{N}_u(z) = N_u(1)$ at the cost of magnitude and phase mismatch in $G(z)\hat{G}^{-1}(z)$. The zero-phase-error-tracking control (ZPETC) [111] assigns instead $\tilde{N}_u(z) = [N_u(1)]^2/N_u(z^{-1})$ and achieves zero-phase error dynamics since $G(z)\hat{G}^{-1}(z) = N_u(z)N_u(z^{-1})/[N_u(1)]^2$ is zero-phase. The zero-magnitude-error-tracking control (ZMETC) [113], on the other hand, eliminates all magnitude errors by converting the unstable zeros to their stable reciprocals, namely, $\tilde{N}_u(z) = N_u(z^{-1})$. Note that $N_u(1)$ in NPZ-ignore and $[N_u(1)]^2$ in ZPETC are added to create a unity DC gain of $G(z)\hat{G}^{-1}(z)$.

Furthermore, to make the approximate inverse model $\hat{G}^{-1}(z)$ in (7.5) realizable and ready to be implemented as a block during feedback/feedforward implementation, a causal inverse model is obtained by multiplying $\hat{G}^{-1}(z)$ with z^{-m}:

$$F(z) = z^{-m}\hat{G}^{-1}(z) = z^{-m}\frac{D(z)}{N_s(z)\tilde{N}_u(z)}, \tag{7.6}$$

$$m = Order[Denominator\ of\ \hat{G}(z)] - Order[Numerator\ of\ \hat{G}(z)] \tag{7.7}$$

is the relative degree of $\hat{G}(z)$ and the *Order* function calculates the highest exponent in a transfer function. Next we will prove that m is always larger than 0 in the NPZ-ignore, ZPETC, and ZMETC.

Proof. We can tell from Table 7.1 that the relative degree of $\tilde{N}_u(z)$ is 0 in each of the three designs.

Thus, from (7.5), the expression of m in (7.7) can be reduced to

$$m = Order[D(z)] - Order[N_s(z)]. \tag{7.8}$$

Also, we have $Order[D(z)] \geq Order[N_s(z)] + Order[N_u(z)]$ from (7.3) and $Order[N_u(z)] > 0$ for NMP systems, yielding $Order[D(z)] > Order[N_s(z)]$, that is, $m > 0$ in (7.8). $\square$

Here, the result $m > 0$ means the delay z^{-m} should always be accounted for to make the inverse model realizable in the feedback/feedforward applications of approximate model inversions. In feedforward applications where a preview of the desire output $y_d(k)$ is available, the delay z^{-m} can be canceled out by letting $r(k) = y_d(k+m)$.

2) Frequency-domain Analysis

Fig. 7.2 shows a block diagram to illustrate the goal of the model inversion design, where r, u, and y represent the reference, the input, and the output signals, respectively. Note that subsequently F can be implemented as a block in the feedback/feedforward controller designs, such as the examples in Section 7.4.3. In Fig. 7.2, the overall transfer function from the reference signal $r(k)$ to the output signal $y(k)$ is $\frac{Y(z)}{R(z)} = F(z)G(z) = z^{-m}G(z)\hat{G}^{-1}(z)$, which reflects the accuracy of the causal inverse $F(z)$. Table 7.1 lists the transfer functions of $\frac{Y(z)}{R(z)}$ in the three approximate model inversions. We take the HDD system in Section 7.3 as an illustrative example. The transfer function of the system with a sampling frequency ($1/T_s$) of 26.4 kHz is

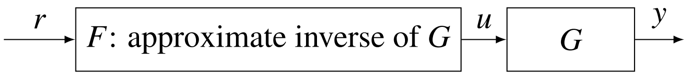

Figure 7.2: Block diagram to illustrate the goal of the model inversion design. Note that F can be implemented as a feedback/feedforward controller.

$$G(z) = z^{-3}\frac{1.447663(z+0.050852)(z+2.494311)}{z^2 - 1.978354z + 0.978808}. \tag{7.9}$$

Here, $G(z)$ has one NMP zero at around -2.5, $N_u(z) = z + 2.494311$, and m in (7.8) is 4. $\frac{Y(z)}{R(z)}$ are $\frac{z^{-4}(z+2.494311)}{3.494311}$ for NPZ-ignore, $\frac{z^{-4}(z+2.494311)(z^{-1}+2.494311)}{3.494311^2}$ for ZPETC, and $\frac{z^{-4}(z+2.494311)}{z^{-1}+2.494311}$ for ZMETC. Fig. 7.3 plots the frequency responses of $\frac{Y(z)}{R(z)}$ of the three approximate designs. At low frequencies close to 0, i.e., $z = e^{j\omega} \to 1$, we get the desired result $\frac{Y(z)}{R(z)} \to 1$ for all three methods,

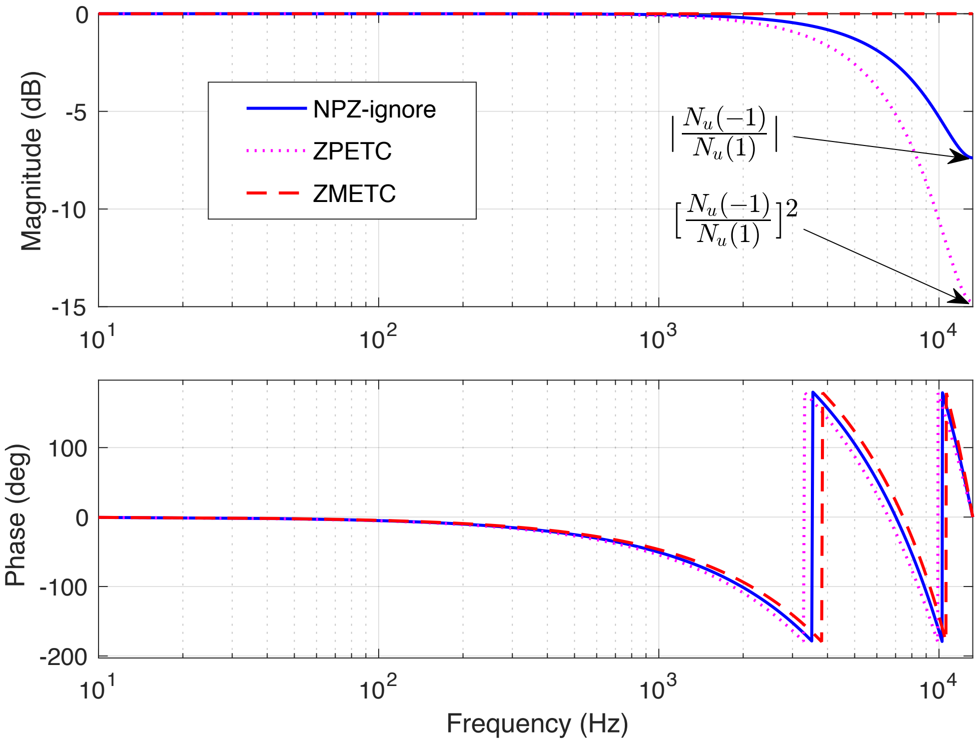

Figure 7.3: Frequency responses of $Y(z)/R(z)(= z^{-m}G(z)\hat{G}^{-1}(z))$ (indicating tracking performances) for different approximate model inversions used in the example of the HDD system in (7.9)

and thereby the magnitude and phase responses of $\frac{Y(z)}{R(z)}$ largely overlap with each other (Fig. 7.3). At the Nyquist frequency π rad (i.e., 13.2 kHz), where $z = \mathrm{e}^{j\pi}$, $\left|\frac{Y(\mathrm{e}^{j\pi})}{R(\mathrm{e}^{j\pi})}\right|$ equals $\left|\frac{N_u(-1)}{N_u(1)}\right|$ for NPZ-ignore and equals $\left[\frac{N_u(-1)}{N_u(1)}\right]^2$ for ZPETC; that is to say, in *log* scale, $\frac{Y(\mathrm{e}^{j\pi})}{R(\mathrm{e}^{j\pi})}$ in ZPETC ($-14.72\,\mathrm{dB}$) has twice the magnitude of $\frac{Y(\mathrm{e}^{j\pi})}{R(\mathrm{e}^{j\pi})}$ in NPZ-ignore ($-7.36\,\mathrm{dB}$) (the top plot of Fig. 7.3). Moreover, in this HDD example, since the NMP zero is a real one at around -2.5 and $m = 4$, all three $\frac{Y(\mathrm{e}^{j\pi})}{R(\mathrm{e}^{j\pi})}$ have zero phase at the Nyquist frequency (the bottom plot of Fig. 7.3).

7.2.3 ILC-based Model Inversion

1) Algorithm

ILC, originally developed for output tracking in repetitive tasks, can be extended to the field of model inversion [115–117]. Here, the inverse model $F(z)$ is constructed by designing its impulse

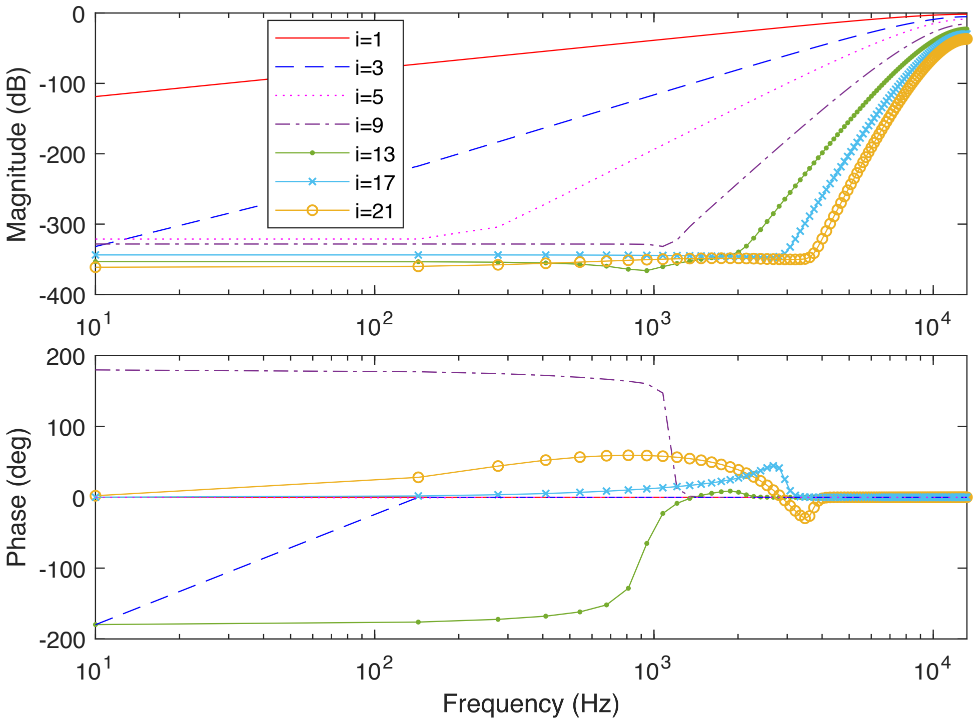

Figure 7.4: Frequency responses of $(1-L(z)G(z))^i$ for the example of the HDD system in (7.9), where $L(z)$ is the learning filter built from ZPETC

response $f(k)$ as the feedforward signal in the following ILC:

$$
\begin{aligned}
F(z) &= \sum_{k=-N/2}^{N/2} f(k) z^{-k}, \\
f(k) &\triangleq \lim_{i \to \infty} u_i(k),
\end{aligned} \tag{7.10}
$$

where $u_i(k)$ is the learned input at the i-th iteration:

$$
\begin{aligned}
u_i(k) &= u_{i-1}(k) + L(z)\left[r(k) - G(z) u_{i-1}(k)\right] \\
&= \left[I - (I - L(z)G(z))^i\right] G^{-1}(z) r(k).
\end{aligned} \tag{7.11}
$$

Here, the training reference $r(k)$ is designed as the delta impulse $\delta(k)$. The ILC learning filter $L(z)$ is built from the approximate model inversions (Section 7.2.2) such that the stability condition $\|1-L(z)G(z)\|_\infty < 1$ is satisfied. With $i \to \infty$, from (7.10) and (7.11), $f(k) \to u_\infty(k) \to G^{-1}(z)\delta(k)$, that is, $f(k)$ approximates the impulse response of the unstable $G^{-1}(z)$. Recall that $f(k)$ is the impulse response of $F(z)$. Thus, we obtain $F(z) \approx G^{-1}(z)$.

Table 7.2: Overview of frequency-domain inversion strategies: approximate, ILC-based, and H_∞-based methods. DT and CT are short for discrete time and continuous time, respectively.

Method	DT or CT	Basic structure or design goal
Approximate	DT	$F(z) = z^{-m}\frac{D(z)}{N_s(z)\tilde{N}_u(z)}$
ILC-based	DT	$F(z) = \sum_{k=-N/2}^{N/2} f(k)z^{-k}$, $f(k) \triangleq \lim_{i\to\infty} u_i(k)$
H_∞-based	CT/DT	$\min \|\|W(s)(1-G(s)\hat{G}^{-1}(s))\|\|_\infty$
Proposed H_∞-based	DT	$\min_{F(z)\in\mathscr{S}} \left\| \begin{bmatrix} W_1(z)(F(z)G(z)-z^{-m}) \\ W_2(z)F(z)G(z) \end{bmatrix} \right\|_\infty$ with $F(z) = z^{-m}\hat{G}^{-1}(z)$

2) Frequency-domain Analysis

In the ILC-based model inversion, the transfer function $1-L(z)G(z)$ determines not only the stability condition but also the convergence rate. Fig. 7.4 shows the frequency responses of $(1-L(z)G(z))^i$, taking again the HDD system in (7.9) for example. Here, $L(z)$ is built from ZPETC. With increasing iteration number i, the magnitudes of $(1-L(z)G(z))^i$ at low frequencies start to converge to zero. Moreover, a larger i yields a wider low-frequency region with zero magnitude.

Therefore, under finite implementation of i, $F(z)$ represents a low-pass approximation of $G^{-1}(z)$ with a tunable bandwidth. One drawback, however, is that system hardware (or a very accurate model G) is needed for iterative experiments to run.

7.2.4 Summary of Literature Review and Motivations of This Chapter

Table 7.2 summarizes the three model inversion strategies. It is noteworthy that these frequency-domain strategies can be implemented in both feedback and feedforward controls. Application of each method certainly depends on the specific problem at hand. Compared with the other two methods, the H_∞-based model inversion can automatically identify the inverse model without knowing the exact NMP zeros, which particularly benefits unstable systems and high-order systems with complicated pole-zero distributions.

For inverse-based *feedback* control, all the surveyed algorithms have considered accurate model inversion but not *robustness against model mismatch* that is also crucial for closed-loop performance. In contrast, the algorithm to be proposed in Section 7.4 enhances the system robustness by limiting the magnitude of the inverse model at frequency regions where large model mismatches exist. Before discussing the main algorithm, we provide in Section 7.3 some preparatory work on the effect of the NMP zeros.

7.3 *Frequency-domain Implications of Modulating NMP Zeros*

This section studies the influence of modulating the NMP zeros (i.e., shifting the locations of the NMP zeros) on the frequency response of a system. For concreteness, we take the HDD system in [108] as an example, where model inversion underpins servo designs that control precisely the position of the read/write head to provide reliable storage.

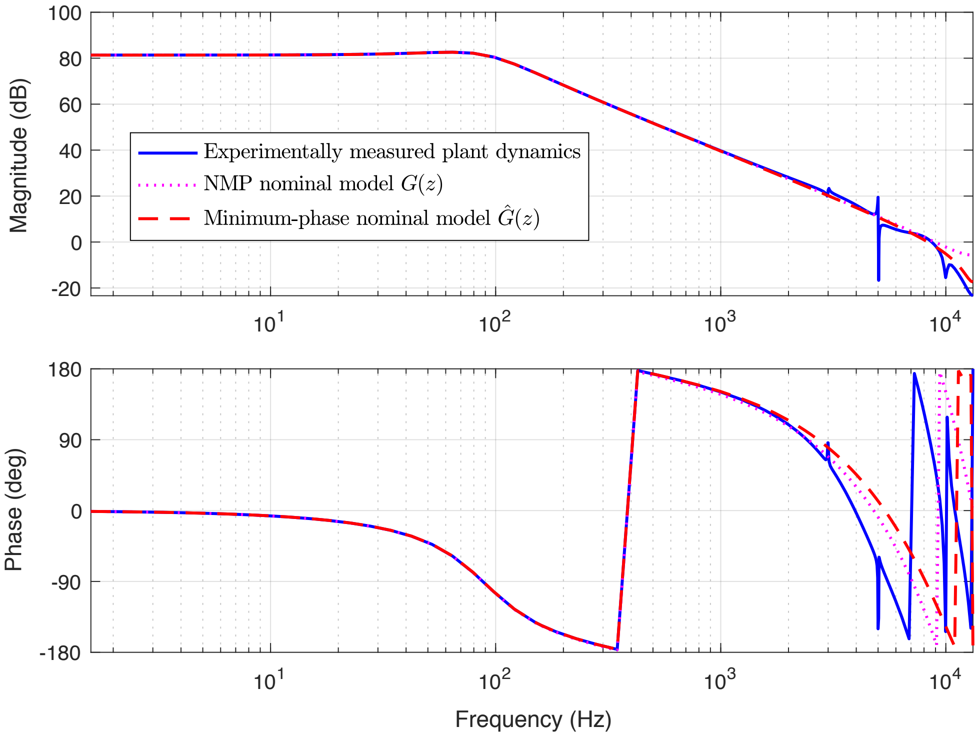

Figure 7.5: Frequency responses of actual system dynamics from experiments and nominal system models in the HDD system

The solid line in Fig. 7.5 shows the frequency response of an experimentally measured HDD system. The nominal model of the motors and actuators in the system is [108]:

$$G_c(s) = e^{-10^{-5}s}\frac{3.74488 \times 10^9}{s^2 + 565.487s + 3.19775 \times 10^5}. \tag{7.12}$$

The ZOH equivalent of $G_c(s)$ sampled at 26.4 kHz, namely $G(z)$, is expressed in (7.9) and has one unstable zero at around -2.5. As plotted in Fig. 7.5, the frequency response of the NMP $G(z)$ matches well with the actual system dynamics (solid line).

We investigate next the frequency-domain implications of the NMP-zero locations by analyzing $N_u(\mathrm{e}^{j\omega}) = \mathrm{e}^{j\omega} + 2.494311$ in (7.9). Consider the rule of thumb that the closed-loop bandwidth B_p is around 10% of the Nyquist frequency ($\frac{1}{2T_s}$ Hz) or $\omega_p = 2\pi B_p T_s \approx 2\pi \frac{0.1}{2T_s} T_s = 18^\circ$; in this example, $B_p = 1300$ Hz, and $\omega_p = 2\pi \times 1300/26400 = 17.72^\circ$. In other words, ω sweeps only a small arc on the unit circle from 0 to 17.72° in the main performance region, yielding mild changes to the vector $\mathrm{e}^{j\omega} + 2.494311$, as shown in Fig. 7.6. Therefore, when shifting the NMP zero to a stable one, e.g., at -0.8 (Fig. 7.6), we can get a minimum-phase nominal model $\hat{G}_0(z)$ that has a stable inverse and largely maintains frequency response of the system in desired low-frequency regions:

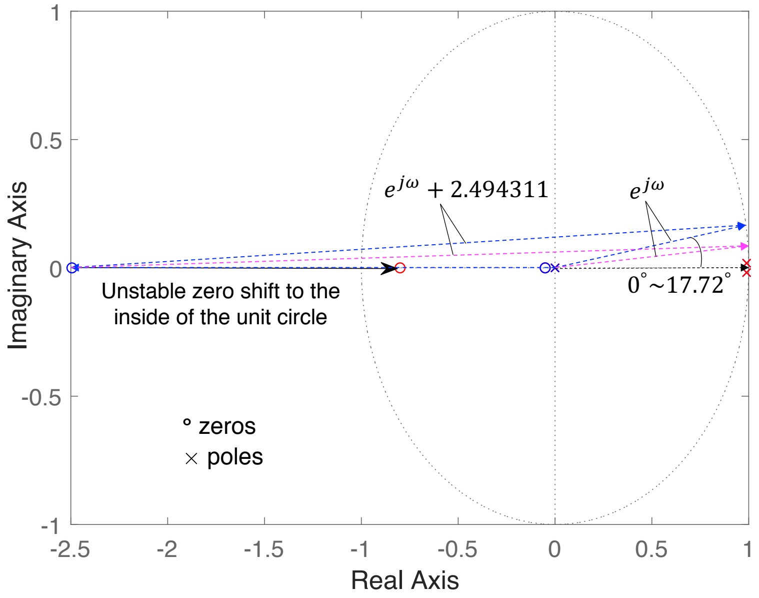

Figure 7.6: Illustration of modulating the experimentally identified NMP zero in the HDD system

$$\hat{G}_0(z) = z^{-3}\frac{1.447663(z+0.050852)(z+0.8)}{z^2 - 1.978354z + 0.978808}.$$

Normalizing $\hat{G}_0(z)$ to retain the DC gain of $G(z)$ in (7.9), we get

$$\hat{G}(z) = z^{-3}\frac{(z+0.050852)(z+0.8)}{0.355831z^2 - 0.703959z + 0.348290}. \tag{7.13}$$

As shown in Fig. 7.5, $\hat{G}(\mathrm{e}^{j\omega})$ (dashed line) matches well with the NMP $G(\mathrm{e}^{j\omega})$ (dotted line) and the actual system dynamics (solid line) below 3000 Hz. This frequency is large enough for most servo-enhancement schemes in single-stage HDDs.

In summary, a stable inverse is readily achievable through modulating the NMP zeros as long as the NMP zeros do not occur in the desired low-frequency regions. This result justifies the basic idea of the H_∞-based optimal inversion, where the manual modulation is upgraded to an automatic and optimal search, as shall be proposed next.

7.4 Proposed H_∞-based Optimal Inversion

Based on the frequency-domain analysis in Section 7.3, this section develops an H_∞-based optimal inversion. The design principle is to automatically search for the optimal inverse model to selectively fit different frequency regions. At frequencies where no NMP zeros exist and no large model uncertainties occur, we impose an accurate model matching between the minimum-phase model $\hat{G}(z)$ and the original NMP model; at other frequencies, we limit the magnitude response of the inverse model to increase the system robustness. We explore the design procedures, case studies, and frequency-domain analyses of the proposed algorithm first for NMP systems and then for unstable systems.

7.4.1 H_∞-based Optimal Inversion for NMP Systems

1) Algorithm

We search among $\mathscr{S}$ (i.e., the set of stable, proper, and rational transfer functions) to find the optimal inverse model $F(z) = z^{-m}\hat{G}^{-1}(z)$ that satisfies:

1. $F(z)$ is realizable/proper. This relates to the z^{-m} term in $F(z)$. To minimize the delays, m can be tuned and usually equals the relative degree of $G(z)$.

2. *model matching*: $\min ||W_1(z)(F(z)G(z) - z^{-m})||_\infty$. Namely, we minimize the maximum magnitude of the model mismatch $F(z)G(z) - z^{-m}$ weighted by $W_1(z)$. The weighting $W_1(z)$ determines the frequency regions for accurate model matching. If $G^{-1}(z)$ is stable, the direct solution is $F(z) = z^{-m}G^{-1}(z)$.

3. *gain constraint*: $\min ||W_2(z)F(z)G(z)||_\infty$. Here, the magnitude of $F(z)G(z)$ is scaled by the weighting $W_2(z)$. For instance, $W_2(z)$ can be a high-pass filter to constrain noise amplification at high frequencies. The solution for this condition alone is $F(z) = 0$, that is, $F(z)$ does not amplify any input signals.

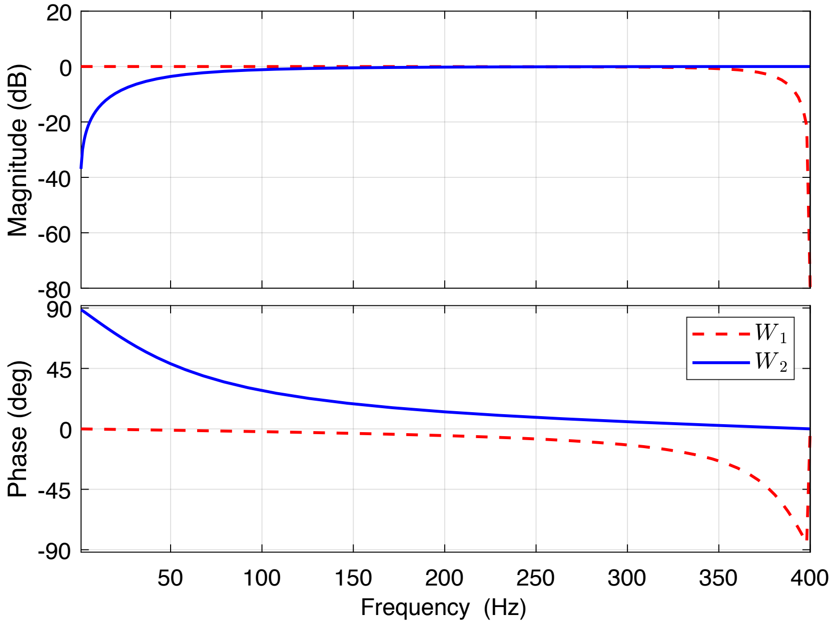

Figure 7.7: Frequency responses of the weightings W_1 and W_2 in the active suspension system

Integrating the above three goals yields the multi-objective optimization principle:

$$\min_{F(z)\in\mathscr{S}} \left\| \begin{bmatrix} W_1(z)(F(z)G(z)-z^{-m}) \\ W_2(z)F(z)G(z) \end{bmatrix} \right\|_\infty . \tag{7.14}$$

The optimal inverse model $F(z)$ given by (7.14) preserves accurate model information in the frequency regions specified by $W_1(z)$ and, on the other hand, penalizes excessive high gains of $F(z)$ at frequencies determined by $W_2(z)$. Typically, $W_1(z)$ is a low-pass filter, and $W_2(z)$ is a high-pass one, as shown in the example of Fig. 7.7. For one system model, the weightings can be flexibly designed, yielding different inverse models $F(z)$.

The optimization principle in (7.14) can be solved within the framework of H_∞ controls. $F(z)$ can be solved by the *hinfsyn* function in the robust control toolbox of MATLAB and tuned for the target performance by changing the input arguments *gamTry* and *gamRange* of the function. Fig. 7.8 shows the block diagram realization of (7.14). Here, the *hinfsyn* function minimizes the two error signals e_1 and e_2. The solution of $F(z)$ exists as long as $G(z)$, $W_1(z)$, and $W_2(z)$ are stable. After (7.14) is solved, a lower-order $F(z)$ can be reached by applying standard model-reduction techniques, if needed.

Remark: When the system model is subjected to perturbations, we can use a multiplicative

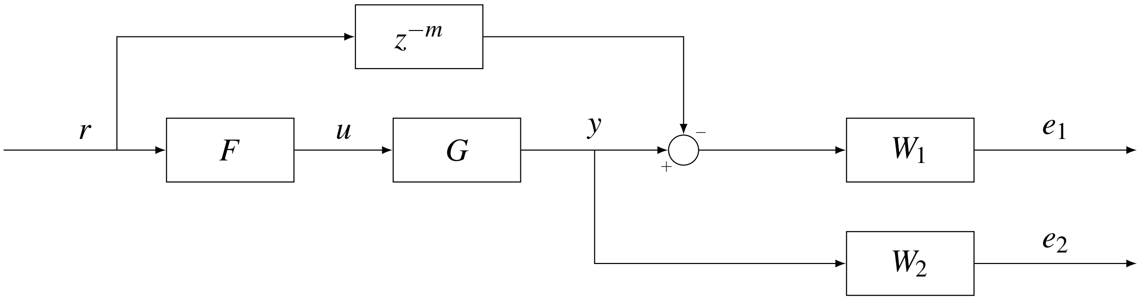

Figure 7.8: Block diagram for the H_∞-based optimal inverse design

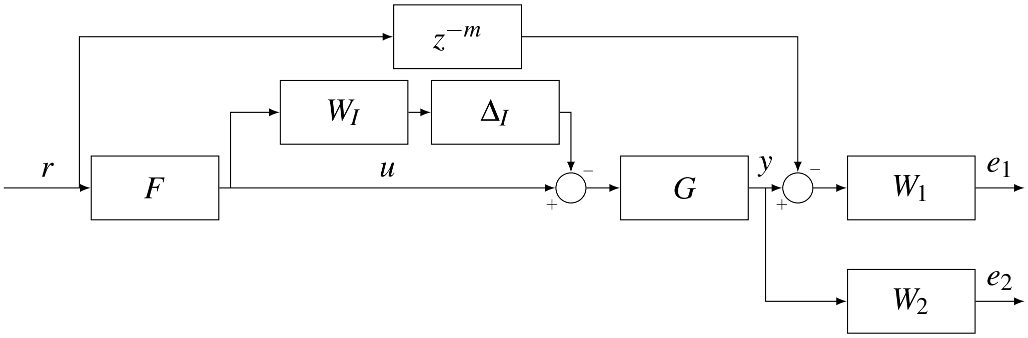

Figure 7.9: Block diagram for the H_∞-based optimal inverse design considering uncertainty

uncertainty model to lump the various dynamic uncertainties:

$$G_p(z) = G(z)(1 + W_I(z)\Delta_I(z)), \tag{7.15}$$

where $\|\Delta_I\|_\infty \leq 1$ [124]. Fig. 7.9 shows the block diagram of the proposed H_∞-based optimal inverse with uncertainties taken into consideration. The problem now is to find a stabilizing inverse model $F(z)$ such that the H_∞ norm of the transfer function between r and $[e_1, e_2]^T$is less than 1 for all Δ_I, that is,

$$\min_{F(z)\in\mathscr{S}} \left\| \begin{bmatrix} W_1(z)(F(z)G_p(z) - z^{-m}) \\ W_2(z)F(z)G_p(z) \end{bmatrix} \right\|_\infty, \tag{7.16}$$

which is no longer a standard H_∞ optimization but a robust performance problem. The μ-synthesis and DK-iteration procedures can be utilized to solve the problem [50, 124].

2) Case Study with Frequency-domain Analysis

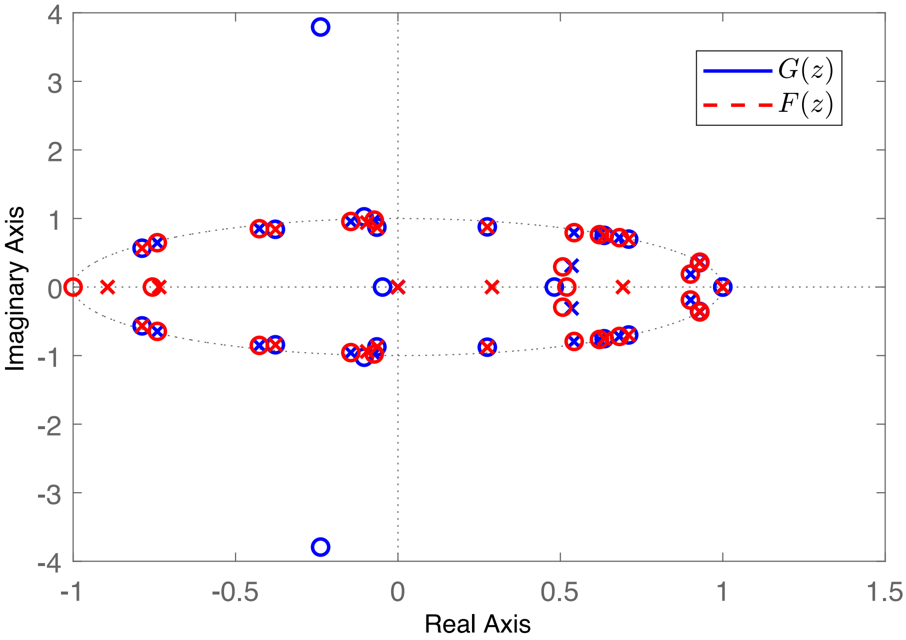

Figure 7.10: Pole-zero plot of the experimentally identified system model and its minimum-phase approximation of the active suspension system

This case study shows efficiency of the proposed algorithm for high-order NMP systems with complicated pole-zero distributions. We take for example the active suspension system in [125] that serves as a benchmark on adaptive regulation. The control goal there is to attenuate the vibrations transmitted to the base frame, and model inversion is critical for the best results achieved in the benchmark [126]. Although the system is open-loop stable, the existence of the NMP zeros challenges model inversion in general feedback and feedforward control.

Via standard system identification methods, the system model $G(z)$ is experimentally identified with a sampling rate of 800 Hz and has an order of 22. As shown in the pole-zero plot in Fig. 7.10, four NMP zeros show up in $G(z)$. Furthermore, with the two weighting functions designed as in Fig. 7.7, we solve the optimization principle in (7.14) and obtain the optimal inverse $F(z)$. After that, we reduce the order of $F(z)$ to 23 by applying the model-reduction function *reduce* in MATLAB. The pole-zero plot of the 23$^{\text{rd}}$-order $F(z)$ is also shown in Fig. 7.10. Then the minimum-phase system model is secured by $\hat{G}(z) = z^{-m}F^{-1}(z)$ $(m = 2)$.

As shown in Fig. 7.11, $\hat{G}(z)$ obtained from the proposed H_∞-based optimal inversion (red dashed line) matches well with the identified NMP $G(z)$ (blue solid line). Moreover, at high frequencies near the Nyquist frequency, $\hat{G}(z)$ from the proposed method (red dashed line) has higher magnitudes

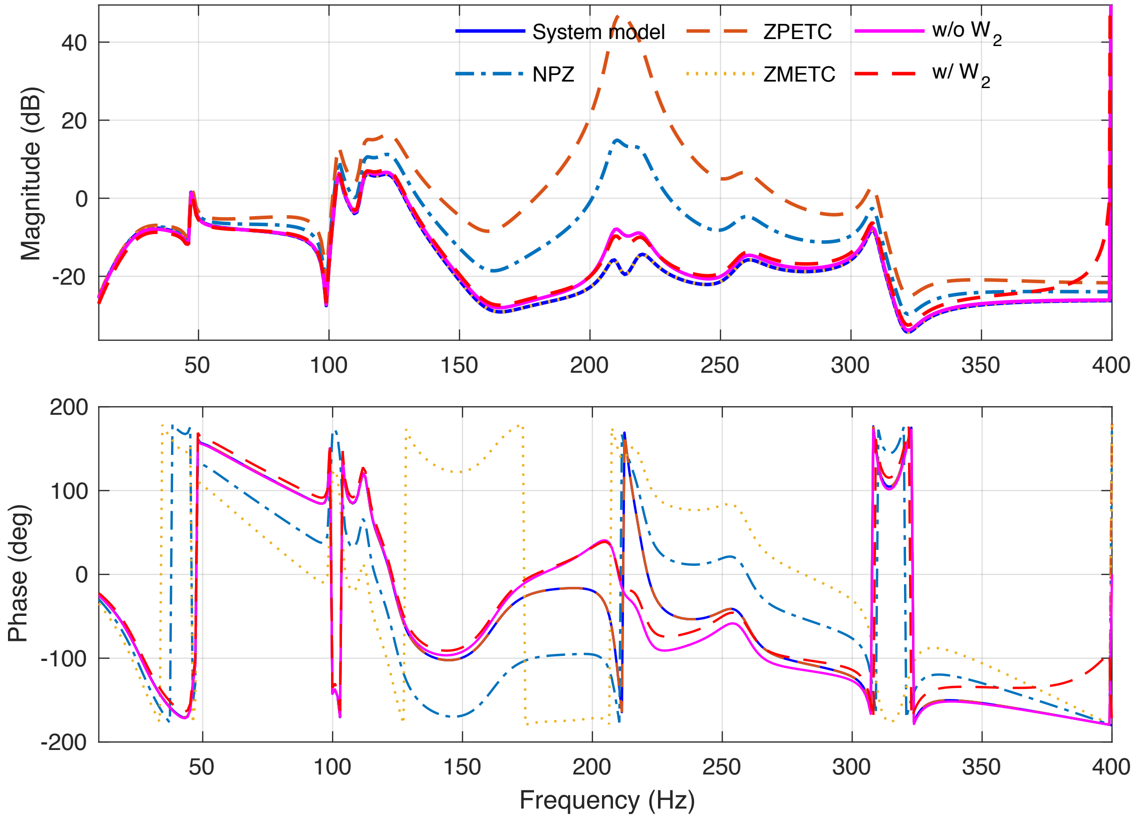

Figure 7.11: Frequency responses of the experimentally identified system model $G(z)$ and its minimum-phase approximations of the active suspension system. Models obtained from ZMETC and ZPETC, respectively, have the same magnitude and phase responses as the system model. Proposed H_∞-based optimal inversion: red dashed line. Previous H_∞-based method without gain constraint: magenta solid line.

than that from the existing H_∞-based method without the gain-constraint condition (magenta solid line). That is to say, the second weighting W_2 has served to limit the magnitudes of the inverse model $F(z)$, as it was designed to. Fig. 7.11 also brings the approximate methods (Section 7.2.2) into comparison. The minimum-phase model $\hat{G}(z)$ from ZMETC has the same magnitude response as the system model $G(z)$ but has large phase errors, whereas ZPETC yields a $\hat{G}(z)$ with no phase error but large magnitude mismatch. $\hat{G}(z)$ obtained from NPZ-ignore has large errors in both magnitude and phase. The proposed H_∞-based optimal inversion outperforms the other methods by not only striking a balance between magnitude and phase matches but also mitigating control efforts (i.e., magnitudes of $F(z)$) at high frequencies for system robustness.

7.4.2 H_∞-based Optimal Inversion for Unstable Systems

1) Algorithm

For unstable $G(z)$, Fig. 7.8 and (7.14) are ill conditioned, and the MATLAB function *hinfsyn* returns an empty solution of $F(z)$. The first intuition for applying the H_∞-based optimal inversion is perhaps to ignore the unstable poles of $G(z)$ and take the remaining part as a fictitious system model. However, ignoring the unstable poles alters the relative degree of the system and may generate a non-causal system. Furthermore, numerical issues may arise after changing the magnitudes of the system. To overcome these difficulties, this section introduces an approach by using an all-pass factorization.

We first factor out the unstable poles of $G(z)$:

$$G(z) = z^{-m} G_0(z) \prod_i \frac{1}{z + p_i}, \tag{7.17}$$

where $|p_i| > 1$ and $G_0(z)$ contains all the zeros and stable poles of $G(z)$.

Performing the all-pass factorization gives

$$G(z) = G_s(z) \prod_i \frac{\bar{p}_i z + 1}{z + p_i}, \tag{7.18}$$

$$G_s(z) = z^{-m} G_0(z) \prod_i \frac{1}{\bar{p}_i z + 1}, \tag{7.19}$$

where $\bar{p}_i$ is the complex conjugate of p_i. Here, the unstable poles in $G(z)$ are replaced by their reciprocals in $G_s(z)$. The product term $\prod_i (\bar{p}_i z + 1)/(z + p_i)$ in (7.18) has unity magnitude, that is, the stable $G_s(z)$ has the same magnitude response as the unstable $G(z)$. Then we can substitute $G(z)$ with $G_s(z)$ when implementing the procedure proposed in Section 7.4.1.

For unstable systems, the design steps of the H_∞-based optimal model inversion are modified as:

1. Write the pole-zero representation of $G(z)$, determine the relative degree m of $G(z)$, and then factor out the unstable poles as in (7.17);

2. Perform the all-pass factorization by transforming $G(z)$ in (7.17) to $G_s(z)$ in (7.19);

3. Substitute $G_s(z)$ into (7.14), and solve (7.14) to find $F_s(z) = z^{-m} \hat{G}_s^{-1}(z)$;

4. Take into account the effect of the unstable poles in (7.18) by $F(z) = F_s(z) \prod_i (z + p_i)/(\bar{p}_i z + 1)$. The minimum-phase system model is then $\hat{G}(z) = z^{-m} F^{-1}(z)$.

2) Case Study with Frequency-domain Analysis

In this case study, we show how to implement the H_∞-based optimal inversion in unstable systems.

Consider a discrete-time transfer function

$$G(z) = \frac{z^{-1}(z+1.5)}{z-1.2} \tag{7.20}$$

with a relative degree of $m = 1$ and a sampling rate of 26.4 kHz. $G(z)$ contains an unstable pole 1.2 at low frequency and an unstable zero -1.5 at high frequency. Following the aforementioned design steps for unstable systems, we first get

$$G_s(z) = \frac{z^{-1}(z+1.5)}{(1-1.2z)}. \tag{7.21}$$

Substituting the stable $G_s(z)$ into the *hinfsyn* function yields a nonempty solution of $F_s(z)$ that satisfies the optimization principle in (7.14): $F_s(z) = z^{-m}\hat{G_s}^{-1}(z)$. Here, we design the weighting functions as

$$W_1(z) = \frac{0.5138z+0.5137}{z+0.0264}, \quad W_2(z) = \frac{z-0.6423}{z-0.2846},$$

using the MATLAB function *makeweight*. The obtained $F_s(z)$ is further normalized to have the same magnitude as the unstable $G_s^{-1}(z)$ at 800 Hz. The inverse filter is thus given by $F(z) = F_s(z)(z-1.2)/(1-1.2z)$. Using *minreal* in MATLAB, we reduce the order of the inverse filter $F(z)$ from 6 to 3 and obtain

$$F(z) = \frac{0.7439z^3 - 1.086z^2 + 0.227z + 0.006236}{z^3 + 0.5056z^2 - 0.1335z - 0.003618}.$$

The minimum-phase system model is thereby $\hat{G}(z) = z^{-1}F^{-1}(z)$. As shown in Fig. 7.12, $\hat{G}(z)$ (dashed line) matches well with $G(z)$ (solid line) particularly at frequencies below 5000 Hz, which is large enough for general feedback designs. Besides, compared with the existing H_∞-based method (dotted line), near the Nyquist frequency, the high gain of $\hat{G}(z)$ from the proposed method (dashed line) indicates a small magnitude of $F(z)$, which matches with the gain-constraint design criterion in Section 7.4.1.

7.4.3 Feedback Applications of the Proposed Algorithms

Model inversion is fundamental to subsequent servo designs, such as YK parameterization and adaptive DOBs [99,106–109]. This section provides application examples that experimentally verify

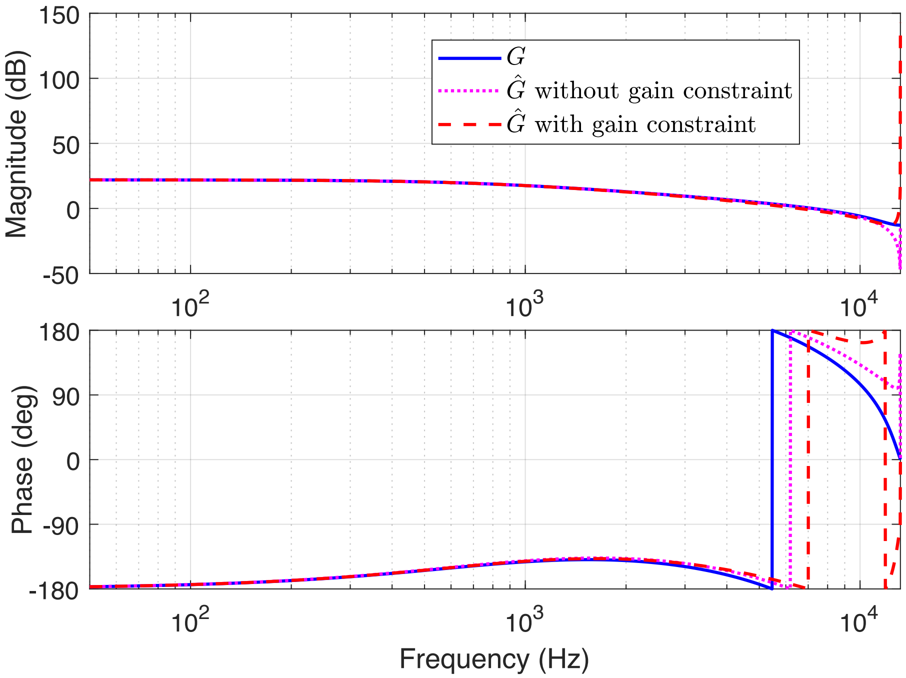

Figure 7.12: Frequency responses of the system model $G(z) = z^{-1}(z+1.5)/(z-1.2)$ and its minimum-phase approximations. Proposed H_∞-based approach: red dashed line. Previous H_∞-based method without gain constraint: magenta dotted line.

the preliminary NMP-zero modulation (Section 7.3) and the H_∞-based optimal inversion (Section 7.4).

1) Galvo Scanner System

Section 5.4 first identifies experimentally the NMP system model for the galvo scannner. After that, the minimum-phase model is obtained by moving the unstable zero from -4.419 to -0.6. Based on the minimum-phase model, an outer-loop inverse-based YK parameterization scheme is built to reject single-frequency narrow-band disturbances.

2) Single-stage HDD System

[108] studies the track-following problem in a single-stage HDD system. The system model in (7.9) has one NMP zero, which is shifted inside the unit circle to make the inverse model strictly stable, as shown in Fig. 7.6. Then with the stable inverse model, [108] designs an adaptive DOB based on the internal model principle to reject multiple narrow-band disturbances.

3) Active Suspension Benchmark

In the active suspension benchmark discussed in [126], the minimum-phase model (red dashed line in Fig. 7.11) is obtained by applying the proposed H_∞-based optimal inversion. The model is then used to build an adaptive DOB with an infinite impulse response structure to reject unknown or time-varying narrow-band vibrations.

Chapter 8

MULTIRATE SPECTRAL ANALYSIS NEAR AND BEYOND NYQUIST FREQUENCY

8.1 Introduction

Many modern manufacturing systems are increasingly subjected to the challenge of limited sensing in the design of control systems. For instance, in LPBF, infrared thermography cameras are expected to feedback more than 100,000 frames of data every second, which is currently unattainable in a real-time control framework [127, 128]. In HDD systems, the sampling speed of the closed loop is limited by the amount of physical servo sectors [129, 130]. Similar scenarios also appear in many other systems, such as vision-guided high-speed controls [131, 132] and chemical processes. This chapter studies performance of the control system in this important problem space.

The focused feedback system here is a sampled-data one with its fast continuous dynamics controlled by a slow-sampled data feedback. To better motivate the research, we briefly review the existing metrics of sampled-data performance. Let a plant $P_c(s)$ be controlled by a digital controller $C(z)$ under a sampling time T_s (in seconds). It is a standard result from digital control theory that single-rate high-gain control ($|C(\mathrm{e}^{j\Omega_o T_s})| = \infty$) can asymptotically reject disturbances at frequency Ω_o in the *sampled* output. However, for the actual continuous-time output, the situation is more involved. Based on sampled-data control [133–137], periodic sampling at T_s partitions the continuous-time frequency into infinite regions of $[2k\pi/T_s, 2(k+1)\pi/T_s)$ where $k = 0, \pm 1, \pm 2, \ldots$, and a continuous-time disturbance yields a fundamental mode plus an infinite number of shifted replicas in the partitioned regions. Due to the sampled-data architecture, the conventional concept of frequency responses does not apply to evaluate the full system performance here [133–138]. Three variations are introduced: (i) the fundamental transfer function (FTF) [137], (ii) the performance frequency gain (PFG) [139, 140], and (iii) the robust frequency gain (RFG) [133]. FTF reveals partial information of the full intersample behavior because it focuses only on the fundamental mode. PFG studies the overall sampled-data behavior within certain frequency regions by employing an input-to-output power gain function [141]. RFG forms a metric for robustness by maximizing the input-to-output power ratio over all possible combinations of the magnitudes and phases of the input [142].

Although a sizable literature has studied the generalized frequency responses in sampled-data control, analyses and evaluations for the case with beyond-Nyquist disturbances have not been sufficiently developed. For instance, under a beyond-Nyquist disturbance, PFG and RFG only provide a scalar value as an indicator of the regulation performance. The distribution and closed-loop impact of each sampling-induced alias mode remain not well understood. This can be problematic for control practitioners since it is hard to distinguish whether a spectral peak in the observed output comes from below- or beyond-Nyquist disturbance sources. As will be shown, the spectral effects of high-gain control on beyond-Nyquist disturbances differ greatly from those below π/T_s. This research uncovers the spectral details and, by doing so, reveals the infeasibility of sub-Nyquist high-gain servo design to reject beyond-Nyquist disturbances in mechatronic systems that have low-pass type of dynamics. In particular, we present and validate the existence of an upper frequency bound for rejecting disturbances even *below* the Nyquist frequency. This bound implies a fundamental limitation for high-gain feedback control of sampled-data systems. We provide tools to analyze the limitation and guidance to implement the tools in practical problems. Theoretical analyses in this chapter are verified by both simulation and experimentation on the galvo scanner platform in LPBF.

The main contributions of the chapter are:

- building a full spectral analysis method to evaluate the intersample behavior for beyond-Nyquist disturbances in sampled-data control;
- applying the proposed method to analyze single-rate high-gain control and discovering the existence of a principal sampled-data bandwidth B_p below the Nyquist frequency;
- verifying numerically and experimentally the theoretical results in LPBF.

In the remainder of this chapter, Section 8.2 reviews several basics of sampled-data control. The main spectral analysis method is provided in Section 8.3. Sections 8.4 and 8.5 provide the numerical and experimental verification of the algorithm, respectively.

Notations: $x[n]$ and $x_c(t)$ denote, respectively, a discrete sequence and a continuous-time signal. $X(\mathrm{e}^{j\omega})$ denotes the discrete-time Fourier transform (DTFT) of $x[n]$. $X_c(j\Omega)$ is the Fourier transform of $x_c(t)$. $\omega = \Omega T_s$, and Ω is in rad/s.

$\Re(c)$ denotes the real part of a complex number $c \in \mathbb{C}$. For a sampled-data system with measurements collected every T_s sec, single-rate control refers to digital control implemented at the same sampling time of T_s.

8.2 Preliminaries

Consider the sampled-data control system in Fig. 8.1, where the solid and the dashed lines represent, respectively, continuous- and discrete-time signal flows. The main elements in the block diagram include the continuous-time plant $P_c(s)$, the analog-to-digital converter (ADC) that samples the continuous output at T_s, the discrete-time controller $C(z)$, and the signal holder $\mathscr{H}$. In this chapter, we focus on the case where $\mathscr{H}$ is a ZOH. The developed tools and analytic framework can be applied to generalized sample hold functions.

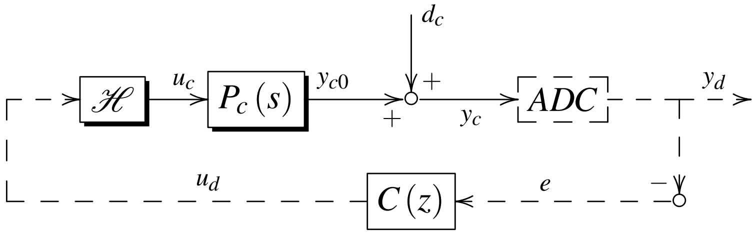

Figure 8.1: Block diagram of a sampled-data control system.

Some basic properties and assumptions of sampled-data control are reviewed first for setting up the problem.

It is assumed that 1) $P_c(s) = P_0(s)e^{-s\tau}$ where $\tau \geq 0$; $P_0(s)$ and $C(z)$ both are LTI, proper, and rational; 2) the coefficients of all transfer functions are real; 3) the closed loop satisfies the *non-pathological sampling condition* [143].

Under assumption 3), the closed-loop sampled-data system is stable if and only if the discrete-time closed loop, consisting of $C(z)$ and the ZOH equivalent of $P_c(s)$, is stable [144, 145].

Lemma 1. *[146] If $X_c(j\Omega)$ exists, the sampling process converting $x_c(t)$ to $x[n] = x_c(nT_s)$ gives*

$$X\left(e^{j\omega}\right) = \frac{1}{T_s}\sum_{k=-\infty}^{\infty} X_c\left(j\left(\frac{\omega}{T_s} - \frac{2\pi}{T_s}k\right)\right). \tag{8.1}$$

Following conventions, we refer to $X_c(j\omega/T_s)$ $(k = 0)$ as the fundamental mode and the other terms $(k \neq 0)$ in the right side of (8.1) as the shifted replicas.

Because of (8.1), after d_c passes the ADC and enters the feedback loop, $y_c(t)$ contains a fundamental mode plus an infinite number of aliases:

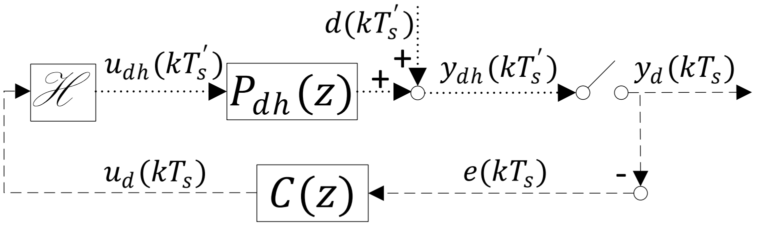

Figure 8.2: Block diagram of multirate sampled-data analysis.

Lemma 2. *[147] If $d_c(t) = \mathrm{e}^{j\Omega_o t}$ and the sampling time is T_s in Fig. 8.1, then the Fourier transform of the continuous-time plant output $y_c(t)$ is*

$$Y_c(j\Omega) = 2\pi\left[1 - \frac{1}{T_s}P_c(j\Omega)H(j\Omega)S_d(\mathrm{e}^{j\Omega T_s})C(\mathrm{e}^{j\Omega T_s})\right]\delta(\Omega-\Omega_o)$$
$$-\frac{2\pi}{T_s}P_c(j\Omega)H(j\Omega)S_d(\mathrm{e}^{j\Omega T_s})C(\mathrm{e}^{j\Omega T_s}) \sum_{k=-\infty,\ k\neq 0}^{\infty} \delta(\Omega-\Omega_o-\frac{2\pi}{T_s}k), \quad (8.2)$$

where $\delta(\Omega-\Omega_o)$ denotes a shifted Dirac delta impulse, $H(j\Omega) = (1-\mathrm{e}^{-j\Omega T_s})/(j\Omega)$ is the Fourier transform of the ZOH, and $S_d(\mathrm{e}^{j\Omega_o T_s})$ is the frequency response of the discrete-time sensitivity function $S_d(z) = 1/(1+P_d(z)C(z))$, where $P_d(z)$, the ZOH equivalent of $P_c(s)$, has the DTFT

$$P_d(\mathrm{e}^{j\Omega_o T_s}) = \frac{1}{T_s}\sum_{k=-\infty}^{\infty} P_c(j(\Omega_o+\frac{2\pi}{T_s}k))H(j(\Omega_o+\frac{2\pi}{T_s}k)). \quad (8.3)$$

In practice, the pure analog output $y_c(t)$ is infeasible to collect and store on digital computers. As an alternative, a fast signal sampled at $T_s^{'}$ is used to approximate the continuous-time output with $T_s^{'} = T_s/F$ ($F > 1$ and $F \in \mathbb{Z}$). The problem then reduces to a multirate sampled-data control one, as shown in Fig. 8.2, where the dotted and dashed lines represent the fast and slow signals sampled by $T_s^{'}$ and T_s, respectively.

To reveal the performance of the fast-sampled output y_{dh}, we adopt the PFG metric [139], which considers the power ratio between the input disturbance $d[k] = d(kT_s^{'})$ and the output $y_{dh}[k] = y_{dh}(kT_s^{'})$:

Definition 1. *Let $d[k] \in \left\{d[k] : d[k] = c\mathrm{e}^{j\Omega k T_s^{'}}, \|c\|_2 < \infty\right\}$ be applied to an multirate system in Fig. 8.2. The PFG $\mathscr{P}(e^{j\Omega T_s^{'}})$ is defined as*

$$\mathscr{P}(e^{j\Omega T_s^{'}}) \triangleq \sup_{d\neq 0}\frac{\|y_{dh}[k]\|_p}{\|d[k]\|_p}, \quad (8.4)$$

where $\|\cdot\|_p$ *represents the discrete-time signal power*

$$\|d[k]\|_p \triangleq \sqrt{\lim_{N\to\infty} \frac{1}{2N+1} \sum_{k=-N}^{N} \|d[k]\|^2}, \tag{8.5}$$

and $\|\cdot\|$ *denotes the Euclidean vector norm.*

8.3 Spectral Analysis of Beyond-Nyquist Regulation Problems

To better motivate the analysis, consider two fast-sampled outputs y_{dh} in Figs. 8.3 and 8.4 collected from experimentation on the galvo scanner system in Section 5.4. The outputs are fast sampled at $T_s^{'} = T_s/F$ with $F = 4$. The Nyquist frequency is $\Omega_N = 5\,\text{kHz}$. The disturbance frequencies are below Ω_N at 3 kHz and beyond Ω_N at 7 kHz, respectively. Under a classic PID control design, the two single-harmonic excitations generate aliased modes at multiple frequencies (bottom plots of Figs. 8.3 and 8.4). When classic single-rate high-gain control [49] is applied to the feedback system, distinct differences show in the output spectra (top plots of Figs. 8.3 and 8.4). Furthermore, all the spectral spikes are not fully attenuated despite the zero steady-state T_s-sampled output (Figs. 8.7a and 8.8a). How do the results happen? What is the governing mechanics of the beyond-Nyquist compensation? How would the spectral distribution change with respect to the excitation frequency?

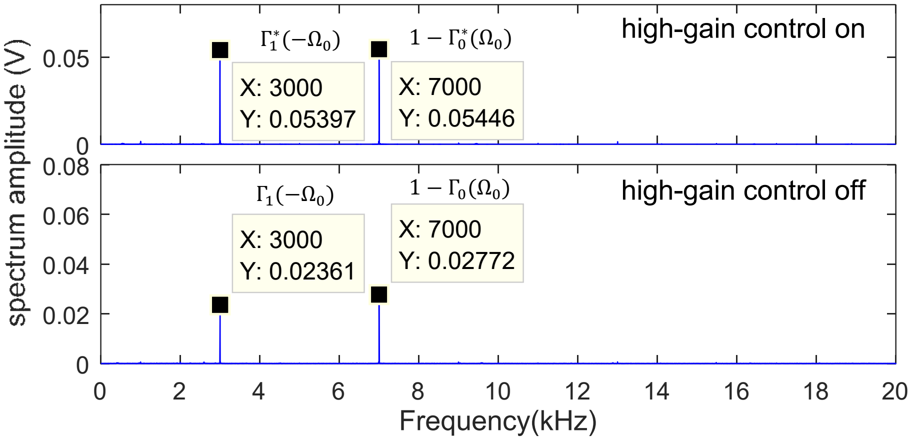

Figure 8.3: FFT of $y_{dh}(t)$ with input disturbance frequency at $1.4\Omega_N$.

To decipher the characteristics of the individual frequency spikes, we propose a spectral analysis method integrating the principles of loop shaping, the limiting conditions of high-gain control, and

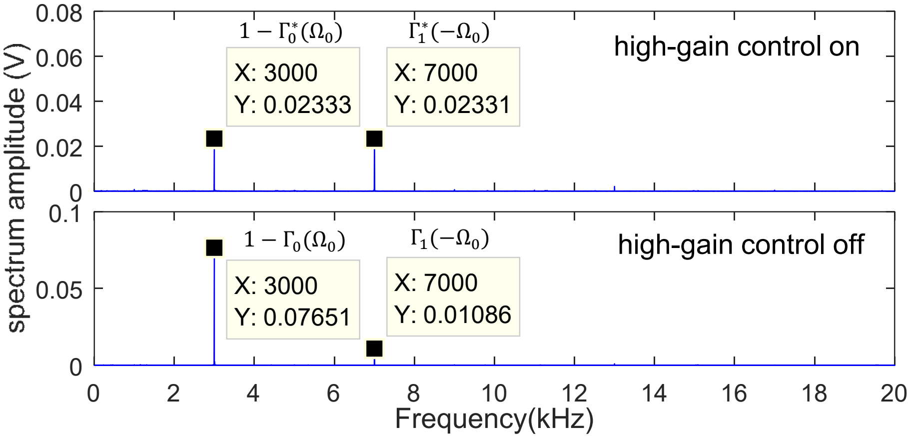

Figure 8.4: FFT of $y_{dh}(t)$ with input disturbance frequency at $0.6\Omega_N$.

the PFG. For a generalized sampled-data control system in Fig. 8.1, to determine the magnitudes of the individual spectral spikes, we define the *characteristic feedback loop gain*

$$\Gamma_k(\Omega_o) \triangleq \frac{P_c(j(\Omega_o+\frac{2\pi}{T_s}k))H(j(\Omega_o+\frac{2\pi}{T_s}k))}{T_sP_d(\mathrm{e}^{j\Omega_oT_s})}T_d(\mathrm{e}^{j\Omega_oT_s}), \tag{8.6}$$

$$T_d(\mathrm{e}^{j\Omega_oT_s}) \triangleq \frac{P_d(\mathrm{e}^{j\Omega_oT_s})C(\mathrm{e}^{j\Omega_oT_s})}{1+P_d(\mathrm{e}^{j\Omega_oT_s})C(\mathrm{e}^{j\Omega_oT_s})} = P_d(\mathrm{e}^{j\Omega_oT_s})C(\mathrm{e}^{j\Omega_oT_s})S_d(\mathrm{e}^{j\Omega_oT_s}). \tag{8.7}$$

After substituting (8.6) into (8.2) and recalling that $\mathscr{F}\left\{\mathrm{e}^{j\Omega_0t}\right\} = 2\pi\delta\left(\Omega-\Omega_0\right)$, the steady-state continuous-time output is simplified to

$$y_c(t) = [1-\Gamma_0(\Omega_0)]\mathrm{e}^{j\Omega_0t} - \sum_{k=-\infty,\ k\neq 0}^{\infty} \Gamma_k(\Omega_0)\mathrm{e}^{j\left(\Omega_0+\frac{2\pi}{T_s}k\right)t}. \tag{8.8}$$

Fact 1. *Based on (8.3) and (8.6), it is immediate that*

$$\sum_{k=-\infty}^{\infty}\Gamma_k(\Omega_o) = T_d(\mathrm{e}^{j\Omega_oT_s}). \tag{8.9}$$

For the case of real-valued disturbances in practice, let $d_c(t) = \cos(\Omega_ot+\phi)$. Recall $\cos(\Omega_0t+\phi) = \Re(\mathrm{e}^{j(\Omega_0t+\phi)})$, $\mathscr{F}\{\Re(x(t))\} = [\overline{X(-j\Omega)}+X(j\Omega)]/2$, and $\delta(-\Omega-\Omega_o) = \delta(\Omega+\Omega_o)$. Laplace transform to the real part of (8.8) gives

$$\begin{aligned} Y_c(j\Omega) = \pi \mathrm{e}^{j\phi}(1-\Gamma_0(\Omega_o))\delta(\Omega-\Omega_o) \\ +\pi \mathrm{e}^{-j\phi}(1-\Gamma_0(-\Omega_o))\delta(\Omega+\Omega_o) \\ -\pi \mathrm{e}^{j\phi}\sum_{k=-\infty,\ k\neq 0}^{\infty}\Gamma_k(\Omega_0)\delta(\Omega-\Omega_o-\frac{2\pi}{T_s}k) \\ -\pi \mathrm{e}^{-j\phi}\sum_{k=-\infty,\ k\neq 0}^{\infty}\Gamma_{-k}(-\Omega_0)\delta(\Omega+\Omega_o+\frac{2\pi}{T_s}k). \end{aligned} \tag{8.10}$$

By the definition in (8.6), $\Gamma_k(\Omega_o)$ is conjugate symmetric, namely, $\Gamma_{-k}(-\Omega_0) = \overline{\Gamma_k(\Omega_0)}$. Thus in (8.10), the gains for two fundamental modes, $|1-\Gamma_0(\Omega_0)|$ and $|1-\Gamma_0(-\Omega_0)|$ $\left(= \left|\overline{1-\Gamma_0(\Omega_0)}\right|\right)$, are equal, and the gains for their related aliased harmonics, $|\Gamma_k(\Omega_0)|$ and $|\Gamma_{-k}(-\Omega_0)|$, are also equal. The collective effect of these modes governs the dynamics of the output.

It is noteworthy that simultaneously rejecting all modes of $Y_c(j\Omega)$ in (8.10) is unattainable. Similar to the feedback limitation on simultaneously rejecting disturbances and sensor noises, the gains for the fundamental modes and the aliases cannot be reduced at the same time. For example, letting $C(\mathrm{e}^{j\Omega_o T_s}) = 0$ in (8.7) yields $\Gamma_k(\Omega_o) = 0$ for any k, namely, a zero gain for each harmonic $|\Gamma_k(\Omega_0)|$ and a unit gain for the fundamental mode $|1-\Gamma_0(\Omega_0)|$ in (8.10). Thus, perfect "rejection" of the aliased harmonics yields no attenuation of the fundamental disturbance.

To understand the differences in the top plots of Figs. 8.3 and 8.4, we explore the shape of the mode gain $\Gamma_k(\Omega_o)$ under high-gain control.

Definition 2. *Under ideal single-rate high-gain control, the new characteristic feedback loop gain is*

$$\Gamma_k^*(\Omega_o) \triangleq \lim_{|C(\mathrm{e}^{j\Omega_o T_s})|\to\infty}\Gamma_k(\Omega_o) = \frac{P_c(j(\Omega_o+\frac{2\pi}{T_s}k))H(j(\Omega_o+\frac{2\pi}{T_s}k))}{T_s P_d(\mathrm{e}^{j\Omega_o T_s})}. \tag{8.11}$$

Fact 2. *From the definition of* $P_d(\mathrm{e}^{j\Omega_o T_s})$ *in (8.3), it is immediate that the summation of* $\Gamma_k^*(\Omega_o)$ *over* k *is*

$$\sum_{k=-\infty}^{\infty}\Gamma_k^*(\Omega_0) = 1,\ \forall\Omega_0. \tag{8.12}$$

(8.12) will be revisited in Section 8.3.2. Similar to $\Gamma_k(\Omega_o)$, $\Gamma_k^*(\Omega_o)$ is also conjugate symmetric: $\left|1-\Gamma_0^*(\Omega_o)\right| = \left|1-\Gamma_0^*(-\Omega_o)\right|$; $\left|\Gamma_k^*(\Omega_o)\right| = \left|\Gamma_{-k}^*(-\Omega_0)\right|$.

8.3.1 Characteristic Feedback Loop Gains $\Gamma_k(\Omega_o)$ *and* $\Gamma_k^*(\Omega_o)$

In this subsection, the properties of the characteristic feedback loop gains are discussed. From (8.6) and (8.11), we obtain that $\Gamma_k(\Omega_o) = \Gamma_k^*(\Omega_o) T_d(\mathrm{e}^{j\Omega_o T_s})$. Since $T_d(z)$ is typically a low-pass filter whose bandwidth B_T is commonly 10%-20% of the Nyquist frequency [147], we have $|\Gamma_k^*(\Omega_o)| > |\Gamma_k(\Omega_o)|$ for most frequencies. Furthermore, we can obtain the following characteristics:

1. If $\underline{\Omega_o + 2k\pi/T_s \in [0, B_T)}$, then the low-pass $H(j(\Omega_o + 2k\pi/T_s))/T_s \approx 1$ in (8.11). For mechatronic systems where the plant usually has high gains at low frequencies, $P_c(j(\Omega_o + 2k\pi/T_s))H(j(\Omega_o + 2k\pi/T_s))/T_s \approx P_d(\mathrm{e}^{j(\Omega_o+2k\pi/T_s)T_s}) = P_d(\mathrm{e}^{j\Omega_o T_s})$, and $|T_d(\mathrm{e}^{j\Omega_o T_s})| \approx 1$, yielding both $\Gamma_k(\Omega_o)$ and $\Gamma_k^*(\Omega_o)$ to be approximately 1. Thus, $|1 - \Gamma_k(\Omega_o)|$ and $|1 - \Gamma_k^*(\Omega_o)|$ are both small. In particular, since $P_d(1) = P_c(0)$ [110] and $H(0)/T_s = 1$, we have $1 - \Gamma_0^*(0) = 0$.

2. If $\underline{\Omega_o + 2k\pi/T_s \in [B_T, \pi/T_s)}$, then $|T_d(\mathrm{e}^{j\Omega_o T_s})| < 1$, and thus $|\Gamma_k^*(\Omega_o)| > |\Gamma_k(\Omega_o)|$. For most frequencies in this region, $|\Gamma_k^*(\Omega_o)| \approx 1$, and $|1 - \Gamma_k^*(\Omega_o)| \ll 1$.

3. If $\underline{\Omega_o + 2k\pi/T_s \in [\pi/T_s, 2\pi/T_s)}$, the low-pass ZOH $|H(j(\Omega + 2k\pi/T_s))|$ reduces quickly outside its approximate bandwidth π/T_s. Although high-gain control still makes $|\Gamma_k^*(\Omega_o)| > |\Gamma_k(\Omega_o)|$, the overall magnitudes $|\Gamma_k^*(\Omega_o)|$ and $|\Gamma_k(\Omega_o)|$ are very small. Thereby, $\left|1 - \Gamma_k^*(\Omega_o)\right|$ and $|1 - \Gamma_k(\Omega_o)|$ both approximate 1.

Interestingly, $\Gamma_k^*(\Omega_o)$ has high gains at the Nyquist frequency and its odd multiplications. To see this point, we analyze the property of $|P_d(\mathrm{e}^{j\frac{\pi}{T_s}T_s})| = |P_d(-1)|$ in (8.11). It is well known that all continuous-time systems with relative degree larger than or equal to two have limiting nonminimum-phase zeros in their ZOH equivalent [110]. In particular, real unstable zeros appear in P_d at high frequencies for small values of T_s. As a result, $|P_d(-1)|$ in (8.11) is small or even zero, yielding a large $\left|\Gamma_k^*(\frac{\pi}{T_s})\right|$. More specifically, we have the following result:

Lemma 3. *If* $P_c(s) = 1/s^n$ *and* n *is a positive even integer, then* $\Gamma_k^*(\frac{\pi}{T_s}) = \infty$.

Proof. See Appendix A.3. □

Lemma 3 illustrates a danger of designing single-rate high-gain controllers near the Nyquist frequency. With the limiting case of $\Gamma_k^*(\frac{\pi}{T_s})$ and $1 - \Gamma_k^*(\frac{\pi}{T_s})$ both being infinity, a continuity analysis gives that $\Gamma_k^*(\Omega)$ and $1 - \Gamma_k^*(\Omega)$ have very high gains near the Nyquist frequency. Correspondingly, from (8.10), the continuous-time output is significantly amplified. It is also worth pointing out that the special case of $P_c(s) = 1/s^2$ is common in precision motion control (e.g., in HDDs [148] and in wafer scanners used in semiconductor manufacturing).

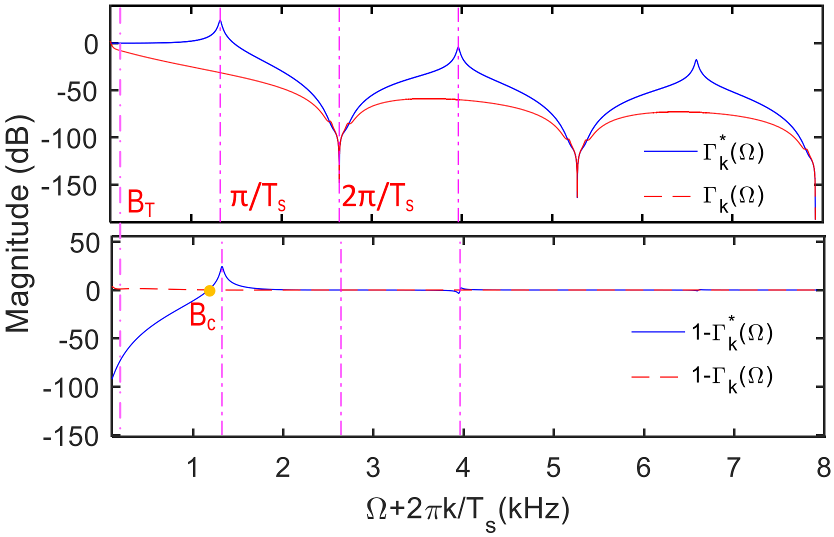

Figure 8.5: Magnitude responses of $\Gamma_k(\Omega)$, $\Gamma_k^*(\Omega)$, $1-\Gamma_k(\Omega)$ and $1-\Gamma_k^*(\Omega)$ as a function of $\Omega+2\pi k/T_s$, where $\Gamma_k^*(\Omega_o)$ and $\Gamma_k(\Omega_o)$ denote the characteristic feedback loop gain with and without high-gain control, respectively. The first three vertical lines indicate, respectively, the Nyquist frequency, the sampling frequency, and $^3/_{2T_s}$.

Figure 8.5 illustrates the magnitudes of $\Gamma_k^{(*)}$ and $1-\Gamma_k^{(*)}$ in a motion-control example in Section 8.4. The Nyquist frequency is indicated by the vertical line at π/T_s. The shapes of the curves match well with the above analysis. As an analysis tool, Fig. 8.5 reveals several fundamental performance limitations of single-rate high-gain control:

- *First*, based on the top plot in Fig. 8.5, unless at very low frequencies (below B_T) where $\Gamma_k(\Omega) \approx \Gamma_k^*(\Omega)$, the aliased harmonics are all amplified by single-rate high-gain control.

- *Second*, high-gain control in $C(z)$ only provides enhanced rejection of the *fundamental* disturbance mode below the intersection frequency of $|1-\Gamma_0^*(\Omega)|$ and $|1-\Gamma_0(\Omega)|$ (B_c in Fig. 8.5). In addition, the achievable maximum attenuation—indicated by the magnitude $|1-\Gamma_0^*(\Omega)|$—decreases with increasing frequency. For common servo design with low-pass type of complementary sensitivity functions T_d, the first two points suggest that single-rate high-gain control *cannot reject continuous-time disturbances near and above Nyquist frequency*.

- *Third*, for $\Omega_o \in (\pi/T_s, 2\pi/T_s)$, $|\Gamma_k^*(\Omega_o)| > |\Gamma_k(\Omega_o)|$, and $|1-\Gamma_0^*(\Omega_o)| \gtrsim |1-\Gamma_0(\Omega_o)| \approx 1$.

In this interval, under single-rate high-gain control, Ω_o being closer to π/T_s causes larger servo degradation, which is different from classic servo control where disturbances at lower frequencies are commonly easier to be attenuated.

Remark 2. *For implementation, it is noteworthy that with the low-pass dynamics in ZOH, the first few frequency modes in (8.10) are usually dominant in magnitude. In Fig. 8.5, after* $3 \cdot \frac{2\pi}{T_s}$*, the magnitudes of* $\Gamma_k(\Omega)$ *and* $\Gamma_k^*(\Omega)$ *are relatively insignificant, and* $\left|1-\Gamma_k^{(*)}(\Omega)\right|$ *is practically equal to 1.*

8.3.2 Typical Spectrum of $y_c(t)$ in Sampled-data Control

In this subsection, we extend the analysis and study the full beyond-Nyquist spectra of the output signals.

Let $\Omega_o \in (\pi/T_s, 2\pi/T_s)$ and $\Omega_o' = 2\pi/T_s - \Omega_o \in (0, \pi/T_s)$. Consider two different disturbances $d_c(t) \triangleq \cos(\Omega_o t)$ and $\tilde{d_c}(t) \triangleq \cos(\Omega_o' t)$, respectively, at above and below the Nyquist frequency. The Fourier transforms of the continuous-time disturbances are

$$\begin{aligned} D_c(j\Omega) &= \pi\delta(\Omega-\Omega_o)+\pi\delta(\Omega+\Omega_o), \\ \tilde{D_c}(j\Omega) &= \pi\delta(\Omega-\Omega_o-\frac{2\pi}{T_s})+\pi\delta(\Omega+\Omega_o-\frac{2\pi}{T_s}). \end{aligned}$$

From (8.1), the sampled disturbance spectra and hence $y_d[k]$ are the same. However, the spectra of $y_c(t)$ are fundamentally different for the two types of disturbances, as illustrated in Figs. 8.6a and 8.6c. One important difference is the location of the fundamental mode (Ω_o for d_c and $2\pi - \Omega_o$ for $d_c^{'}$). For Ω_o being above Nyquist frequency, the magnitude of the fundamental mode $|1-\Gamma_0(\Omega_o)|$ is close to 1 (cf. Fig. 8.5). The dominant aliased mode $\Gamma_1(-\Omega_o)$ occurs at $2\pi/T_s - \Omega_o$ below the Nyquist frequency (see Fig. 8.6a). With single-rate high-gain control at Ω_o, the magnitude of $\Gamma_k(\Omega_o)$ increases towards the limiting case $\Gamma_k^*(\Omega_o)$. In particular, $\Gamma_1(-\Omega_o)$ increases towards $\Gamma_1^*(-\Omega_o) \approx 1$ (Fig. 8.6b). Meanwhile, $|1-\Gamma_k(\Omega_o)|$ stays close to 1 or is even increased. Collectively, $d_c(t)$ is amplified by single-rate high-gain control.

On the other hand, for Ω_o' below the Nyquist frequency, the fundamental mode $1-\Gamma_0(\Omega_o^{'})$ can be effectively reduced (from the dashed line to the solid line in the bottom plot of Fig. 8.5). The aliased modes $\Gamma_k(\Omega_o')$ still increase to $\Gamma_k^*(\Omega_o')$. However, $|\Gamma_k^*(\Omega_o^{'})|$ remains small in the top plot of Fig. 8.5 since the lowest frequency of the alias is already beyond the Nyquist frequency (at $2\pi/T_s - \Omega_o^{'}$). Thus, $\tilde{d_c}(t)$ can be reduced by single-rate high-gain control.

The graphical tool is justified by the experimental results in Figs. 8.3 and 8.4. In Fig. 8.3, the fundamental mode occurs at 7000 Hz, and the amplified mode at 3000 Hz corresponds to the alias

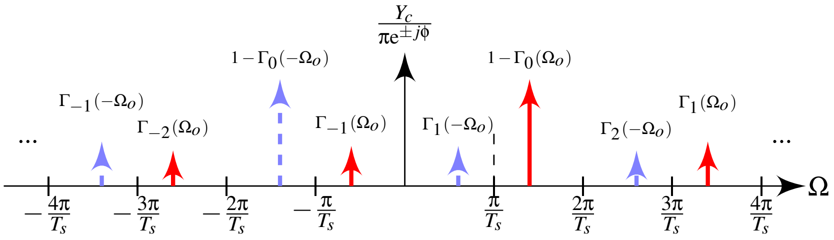

(a) $d_c(t) = \cos(\Omega_o t)$ with the baseline control

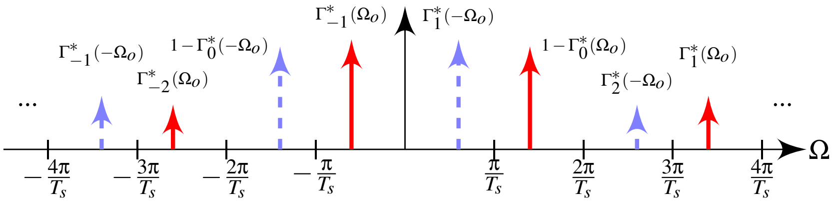

(b) $d_c(t) = \cos(\Omega_o t)$ with enhanced discrete-time high-gain control at Ω_o

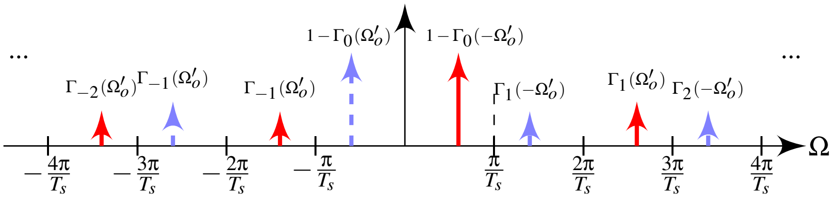

(c) $\tilde{d}_c(t) = \cos(\Omega'_o t) = \cos((2\pi/T_s - \Omega_o)t)$ with the baseline control

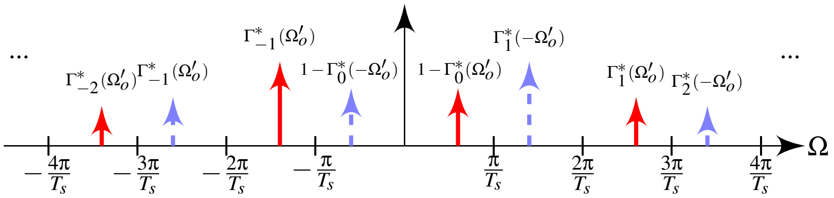

(d) $\tilde{d}_c(t) = \cos(\Omega'_o t)$ with enhanced discrete-time high-gain control at Ω_o

Figure 8.6: Illustration of the spectrum of $y_c(t)$ in sampled-data control when $\pi/T_s < \Omega_o < 2\pi/T_s$. Dashed spikes: $\delta(\Omega + \Omega_0)$ and its aliases; solid spikes: $\delta(\Omega - \Omega_0)$ and its aliases.

mode below the Nyquist frequency. In Fig. 8.4, the frequencies of the two modes are switched. We can now distinguish that Fig. 8.3 describes the trend of the case in Figs. 8.6a and 8.6b while Fig. 8.4 matches the results in Figs. 8.6c and 8.6d.

Next we show how to *connect the frequency-domain results with the time-domain observations*. With sub-Nyquist high-gain control, the T_s-sampled disturbances $d_c(t)$ and $\tilde{d}_c(t)$ can be perfectly rejected from the sampled output, as shown in the corresponding time-domain responses of Figs.

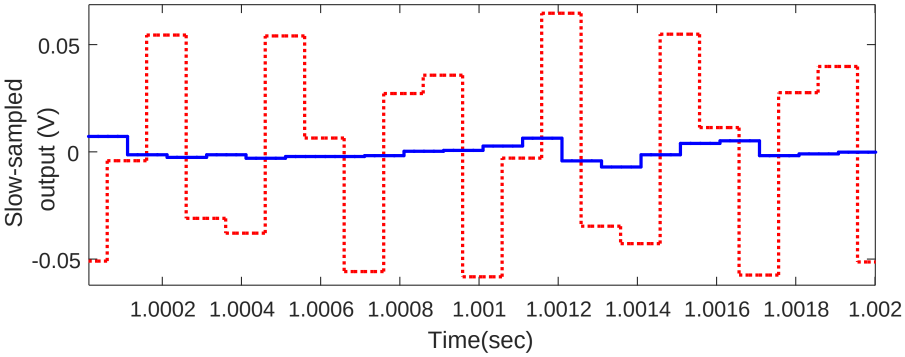

(a) $y_d(t)$ with the sampling time of T_s.

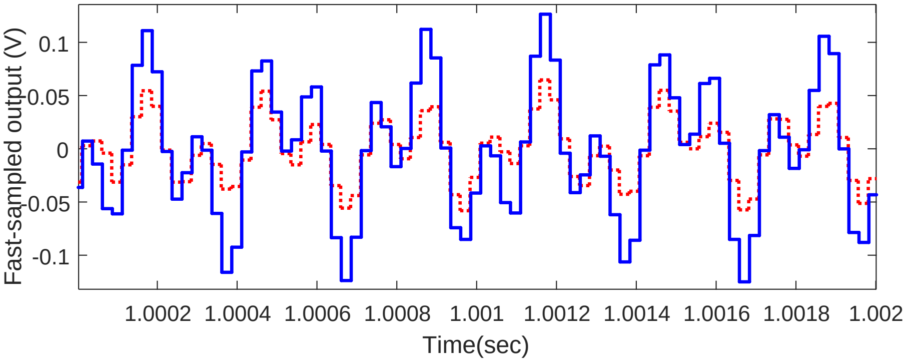

(b) $y_{dh}(t)$ with the sampling time of $T_s^{'}$.

Figure 8.7: Plant output with the input disturbance at $1.4\Omega_N$. (*The solid and dashed lines represent the cases with single-rate high-gain control on and off, respectively*.)

8.7a and 8.8a. The disturbance rejection may conventionally suggest null gains in the spectrum below the Nyquist frequency, which is, however, neither the case for $d_c(t)$ or $\tilde{d}_c(t)$. In fact, Fig. 8.6b contains significant components at $2\pi/T_s - \Omega_o$. And Fig. 8.7b shows the hidden amplification of the disturbances. To connect the spectral distribution with the zero steady-state T_s-sampled output, an important piece is the effect of the sampling operation in the frequency domain. Take the case of $d_c(t)$ as example. After $y_c(t)$ is sampled at T_s, each solid spike in Fig. 8.6b creates an alias at Ω_o (cf. Lemma 1). Based on (8.10), the magnitude of the discrete-time spectral peak at Ω_0 is a normalized version of $[1-\Gamma_o^*(\Omega_o)] - \Gamma_{-1}^*(\Omega_o) - \Gamma_1^*(\Omega_o) - \Gamma_{-2}^*(\Omega_o) - \Gamma_2^*(\Omega_o) - \dots$, which equals 0 from (8.12). For the case where the disturbance is beyond Nyquist frequency in Fig. 8.6b, because there is little control over $1-\Gamma_0(\Omega_o)$, and $\Gamma_{\pm k}(\Omega_o)$ $(k \neq 0)$ is amplified, the aliasing effect cancels the fundamental component after sampling. Fig. 8.6d, on the other hand, achieves zero T_s-sampled output by reducing the magnitude of $1-\Gamma_0(\Omega_o')$.

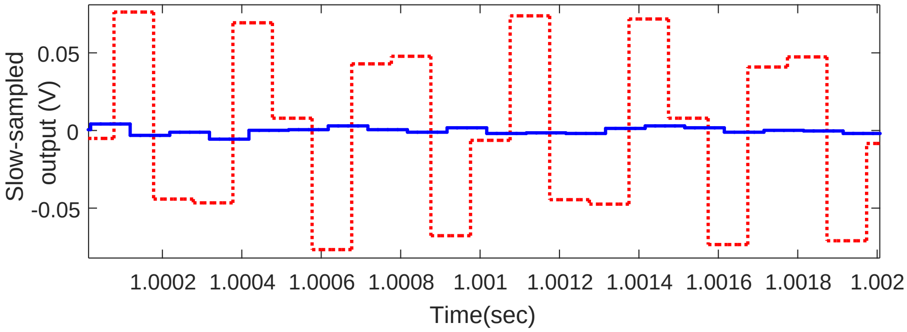

(a) $y_d(t)$ with the sampling time of T_s.

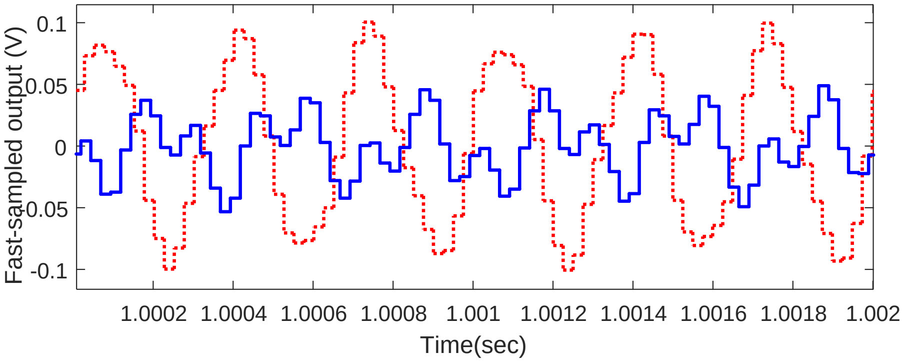

(b) $y_{dh}(t)$ with the sampling time of T_s'.

Figure 8.8: Plant output with the input disturbance at $0.6\Omega_N$. (*The solid and dashed lines represent the cases with single-rate high-gain control on and off, respectively*.)

8.3.3 Performance Frequency Gain and the Fundamental Mode

With the understanding of individual mode shapes, we can better relate the spectral responses to the time-domain data in sampled-data control and explain the beyond-Nyquist disturbance rejection. This section connects the analysis of the individual modes with the PFG metric. An important observation is that under single-rate high-gain control, PFG also has a high gain near the Nyquist frequency.

Recall the transformation of a sampled-data system into an multirate one by fast sampling in Fig. 8.2. The fast and slow signals are sampled by T_s' and $T_s = FT_s'$, respectively. Let $D(\mathrm{e}^{j\Omega T_s'})$ denote the DTFT of $d[k]$. Analogous to the derivation of (8.2), the DTFT of the fast-sampled output

$y_{dh}[k]$ [141] is

$$Y_{dh}(\mathrm{e}^{j\Omega T_s'}) = \left[1 - \frac{1}{F}P_{dh}(\mathrm{e}^{j\Omega T_s'})H(\mathrm{e}^{j\Omega T_s'})T_d(\mathrm{e}^{j\Omega T_s})/P_d(\mathrm{e}^{j\Omega T_s})\right] D(\mathrm{e}^{j\Omega T_s'})$$
$$+ \frac{1}{F}P_{dh}(\mathrm{e}^{j\Omega T_s'})H(\mathrm{e}^{j\Omega T_s'})T_d(\mathrm{e}^{j\Omega T_s})/P_d(\mathrm{e}^{j\Omega T_s}) \sum_{k=1}^{F-1} D(\mathrm{e}^{j(\Omega T_s' - \frac{2\pi k}{F})}), \quad (8.13)$$

where P_d and P_{dh} represent the ZOH plant models under the sampling time of T_s and T_s', respectively, and the transfer function of the ZOH interpolator is

$$H(z) = \sum_{k=0}^{F-1} z^{-k} = \begin{cases} F & z = 1 \\ \frac{1-z^{-F}}{1-z^{-1}} & z \neq 1 \end{cases}. \quad (8.14)$$

Based on (8.13), the multirate characteristic feedback loop gain is defined as

$$\Gamma_k(\Omega_o) = \frac{P_{dh}(\mathrm{e}^{j(\Omega_o T_s' + \frac{2\pi k}{F})})H(\mathrm{e}^{j(\Omega_o T_s' + \frac{2\pi k}{F})})T_d(\mathrm{e}^{j\Omega_0 T_s})}{FP_d(\mathrm{e}^{j\Omega_0 T_s})}, \quad (8.15)$$

and the limiting case with single-rate high-gain control is

$$\Gamma_k^*(\Omega_o) = \frac{P_{dh}(\mathrm{e}^{j(\Omega_o T_s' + \frac{2\pi k}{F})})H(\mathrm{e}^{j(\Omega_o T_s' + \frac{2\pi k}{F})})}{FP_d(\mathrm{e}^{j\Omega_0 T_s})}. \quad (8.16)$$

Lemma 4. *For the multirate system in Fig. 8.2, the modified PFG under single-rate high-gain control at* Ω_0 *is*

$$\mathscr{P}_h(\mathrm{e}^{j\Omega_0 T_s'}) = \sqrt{\left\|1 - \Gamma_0^*(\Omega_o)\right\|^2 + \sum_{k=1}^{F-1} \left\|\Gamma_k^*(\Omega_o)\right\|^2}. \quad (8.17)$$

The derivation is similar to the one introduced in [141] and is omitted here. Lemma 4 connects the input-output power ratio with the gains of the individual signal modes. PFG evaluates the overall effect of the intersample behavior and how a sampled-data control system attenuates or amplifies input disturbances in certain frequencies, whereas the characteristic feedback loop gains look into each individual mode in the spectra of the continuous-time (and fast-sampled) outputs.

Note that independent of the baseline controller, the modified PFG is a property of the plant itself since $\Gamma_k^*(\Omega_o)$ depends on P_{dh}, H, F, and P_d alone. In addition, the modified PFG is a pointwise quantity that focuses on the limiting case where ideal high-gain control is applied at one value of Ω_0, that is, $T_d(\mathrm{e}^{j\Omega_o T_s}) = 1$. This pointwise high-gain control can be achieved with tools such as special YK parameterizations, DOBs, and peak filters [46, 49, 149]. To introduce $T_d(\mathrm{e}^{j\Omega_o T_s}) = 1$ at different values of Ω_0, the high-gain controller would need to be retuned or be adaptive. When the customized high-gain control is turned off, the high-gain controller is replaced by a regular servo algorithm (e.g. PID and lead-lag compensation), and therefore $\Gamma_0^*(\Omega_o)$ and $\Gamma_k^*(\Omega_o)$ are replaced by $\Gamma_0(\Omega_o)$ and $\Gamma_k(\Omega_o)$ in (8.15). The modified PFG then describes the performance of a baseline LTI controller.

For a typical plant dynamic in Section 8.5, $\mathscr{P}_h(\mathrm{e}^{j\Omega T_s'})$ is calculated and plotted in Fig. 8.9.

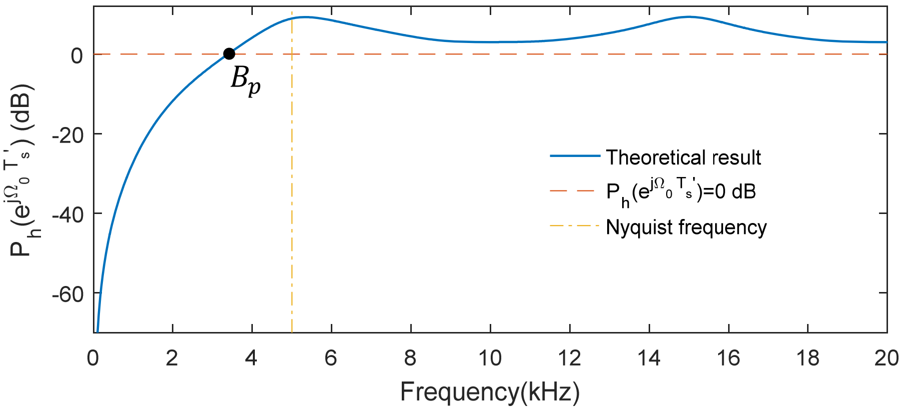

Figure 8.9: Performance frequency gain under high-gain control.

Definition 3. *The intersection frequency between the curve expressed by (8.17) and the line of* $\mathscr{P}_h(\mathrm{e}^{j\Omega T_s'}) = 0$ *dB is called the* principal sampled-data bandwidth B_p.

Lemma 5. *For general mechatronic systems,* B_p *is smaller than the Nyquist frequency.*

Proof. See Appendix A.4. □

Implications: Similar to the analyses of the discrete-time sensitivity function in digital control, the proposed PFG analysis gives an important threshold frequency B_p in sampled-data control. For disturbance frequencies below B_p, the power of the fast-sampled output signal is smaller than that of the input disturbance. In other words, sub-Nyquist high-gain control is efficient for rejecting disturbances with frequencies below B_p. However, for beyond-B_p disturbances with $\mathscr{P}_h > 0\,\mathrm{dB}$, single-rate high-gain control exacerbates the servo performance.

Remark 3. *In practice, disturbances can also enter from the input of the plant in Fig. 8.2. In this case, the input disturbance* d_i *is related to* d *in Fig. 8.2 by* $D(\mathrm{e}^{j\Omega T_s'}) = D_i(\mathrm{e}^{j\Omega T_s'})P_{dh}(\mathrm{e}^{j\Omega T_s'})$. *We* *can analogously define and compute the modified input PFGs*

$$\mathscr{P}_b^{'}(\mathrm{e}^{j\Omega_0 T_s^{'}}) = \sup_{d_i \neq 0} \frac{\|y_{dh}\|_p}{\|d_i\|_p} = \left|P_{dh}(\mathrm{e}^{j\Omega_0 T_s^{'}})\right| \sqrt{\|1-\Gamma_0(\Omega_o)\|^2 + \sum_{k=1}^{F-1} \|\Gamma_k(\Omega_o)\|^2}, \tag{8.18}$$

and

$$\mathscr{P}_h^{'}(\mathrm{e}^{j\Omega_0 T_s^{'}}) = \lim_{T_d(\mathrm{e}^{j\Omega_0 T_s^{'}}) \to 1} \mathscr{P}_b^{'}(\mathrm{e}^{j\Omega_0 T_s^{'}}) = |P_{dh}| \sqrt{\left\|1-\Gamma_0^*(\Omega_o)\right\|^2 + \sum_{k=1}^{F-1} \left\|\Gamma_k^*(\Omega_o)\right\|^2}. \tag{8.19}$$

The modified input PFG can be verified by the time-domain definition in (8.18), that is, dividing output signal power by input signal power. Dividing the modified input PFG $\mathscr{P}_h^{'}(\mathrm{e}^{j\Omega_0 T_s^{'}})$ by $\left|P_{dh}(\mathrm{e}^{j\Omega_0 T_s^{'}})\right|$, we can then generate the modified PFG $\mathscr{P}_h(\mathrm{e}^{j\Omega_0 T_s^{'}})$.

Before presenting the numerical and experimental results, we briefly summarize the application steps of the proposed spectral analysis method:

1. Determine $\Gamma_k(\Omega_o)$, the characteristic feedback loop gains, by (8.6) and (8.15). In addition, determine $\Gamma_k^*(\Omega_o)$, the limiting cases with single-rate high-gain control, by (8.11) and (8.16).

2. Plot the magnitude responses of $\Gamma_k(\Omega)$, $\Gamma_k^*(\Omega)$, $1-\Gamma_k(\Omega)$, and $1-\Gamma_k^*(\Omega)$ to look into individual spectral spikes. Note that these are hybrid functions of continuous- and discrete-time frequency responses.

3. Calculate and plot the modified PFG based on (8.17).

4. Identify the principal sampled-data bandwidth B_p, as shown in Fig. 8.9.

5. Run simulation and experimentation to get the time- and frequency-domain results with below- and beyond-B_p disturbance input. Numerically compute the modified PFG from the input-to-output power ratio in Definition 1. The results should verify the location of B_p and the trend of the individual spectral spikes.

8.4 Numerical Verification

Consider a plant $P_c(s) = 3.74488 \times 10^9/(s^2 + 565.5s + 319775.2)$ with an input delay of $10\,\mu$s. Let the sampling time be $T_s = 1/2640$ sec. The baseline controller is a PID controller $C(z) = k_p + k_i/(z-1) + k_d(z-1)/z$ with $k_p = 7.51 \times 10^{-5}$, $k_i = 3.00 \times 10^{-5}$, and $k_d = 3.60 \times 10^{-4}$. Such a design provides a bandwidth at 92 Hz that complies with the rule-of-thumb of around 10% of the Nyquist frequency. $y_c(t)$ is fast-sampled at $T_s^{'} = T_s/20$ to approximate the continuous-time output in Fig. 8.1. Single-frequency vibrations below and above the Nyquist frequency are introduced to the plant. The narrow-band DOB [49] is applied on top of the PID controller. Such a design provides perfect compensation of above- and below-Nyquist sinusoidal signals in the *sampled* output $y_d[k]$.

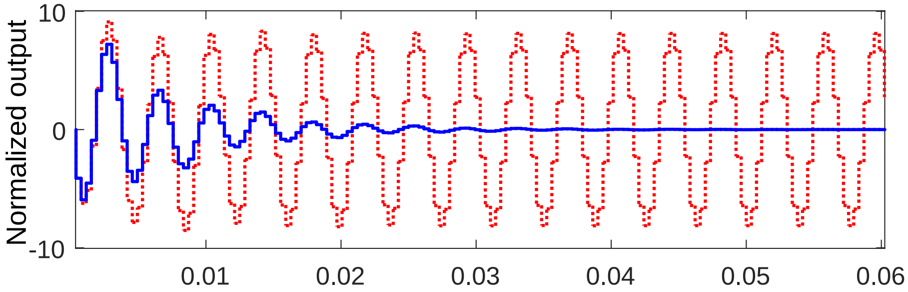

(a) $y_c(t)$ sampled at T_s.

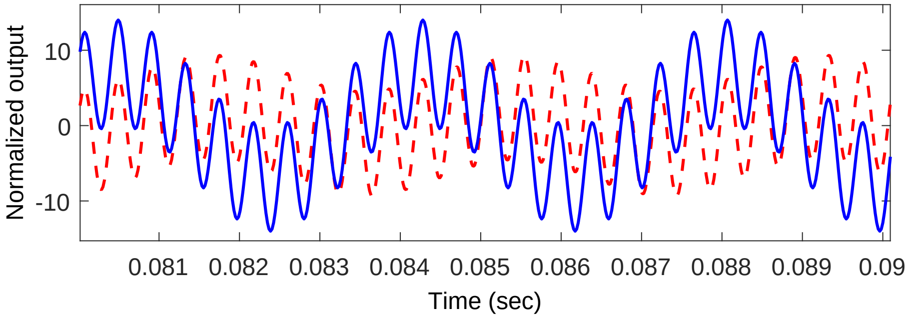

(b) $y_c(t)$ sampled at $T_s/20$.

Figure 8.10: Plant output with the input disturbance at $1.8\Omega_N$. (*The solid and dashed lines represent the cases with single-rate high-gain control on and off, respectively*.)

Figs. 8.10 and 8.11 present the time- and frequency-domain computation results, which verify the limitation of single-rate high-gain control for beyond-Nyquist disturbance rejection. The results match with the prediction in Fig. 8.6 that single-rate high-gain control amplifies beyond-Nyquist disturbances. When the disturbance occurs at 2376 Hz ($1.8\Omega_N$), the intersample signal is significantly amplified in Fig. 8.10b, although high-gain control yields zero sampled-output at steady state (Fig. 8.10a). The amplification is also evident in the frequency domain (Fig. 8.11). Single-rate high-gain control barely changes the fundamental component at 2376 Hz but greatly amplifies the aliased component at 264 Hz.

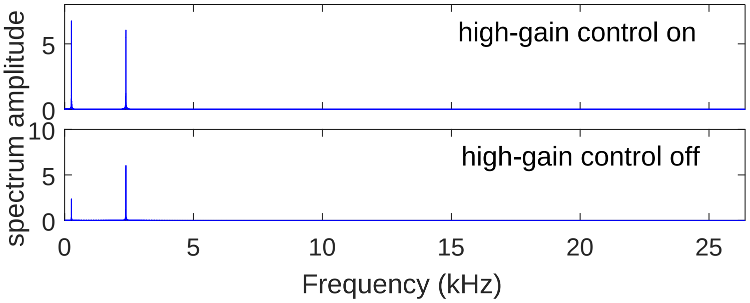

Figure 8.11: FFT of $y_c(t)$ sampled at $T_s/20$.

Fig. 8.12 verifies the case with regular below-Nyquist disturbances. The T_s-sampled output also reaches zero at steady state and is omitted here. With the fundamental mode at 924 Hz (below the Nyquist frequency), single-rate high-gain control can attenuate this spectral spike. As theoretically predicted by Fig. 8.6d, the aliased harmonics are, however, all amplified. Therefore, the actual continuous-time output contains intersample ripples.

8.5 Experimental Verification

Experiments are conducted on the galvo scanner platform (Fig. 5.9). To form a baseline servo system, a built-in PID-type controller $C_0(z)$ is embedded in the motor driver. $C_0(z)$ and the actual plant $P_0(z)$ are treated as the new plant $P_{dh}(z)$, as in Section 5.3. Fig. 5.14 shows the frequency response of the measured and identified $P_{dh}(z)$ (aka identified $\hat{L}(z)$ in Fig. 5.14). The DOB [49] with $C(z) = 1$ in Fig. 8.13 is implemented to enable high-gain control at selective frequencies. Transfer functions inside the DOB block are all implemented at a sampling time of $T_s = 0.1\,\text{ms}$. Thus the Nyquist frequency Ω_N equals 5 kHz. The fundamental sampling time used to measure y_{dh} is $T_s^{'} = 0.025\,\text{ms}$. That is, the fast sampling is conducted at $T_s^{'} = T/F$ with $F = 4$ for diagnosis of the beyond-Nyquist performance. A single-harmonic disturbance with magnitude 0.1V and frequency $\omega_o = 2\pi\Omega_o T_s^{'}$ (Ω_o in Hz) is introduced to the system. In addition, the system is subjected to broadband random disturbances at a magnitude of about 20 mV.

Fig. 8.14 illustrates the theoretically computed input PFGs using (8.18) for the baseline controller and (8.19) for the customized high-gain controller. Experimental data of $\mathscr{P}_h^{'}(e^{j\Omega_0 T_s^{'}})$ is obtained by following the time-domain definition in (8.18) for each value of Ω_o. From Fig. 8.14, the three experimental PFGs of $\mathscr{P}_h^{'}(e^{j\Omega_0 T_s^{'}})$ at 3 kHz ($0.6\Omega_N$), 4 kHz (0.8Ω), and 7 kHz ($1.4\Omega_N$) match the theoretical computations very well.

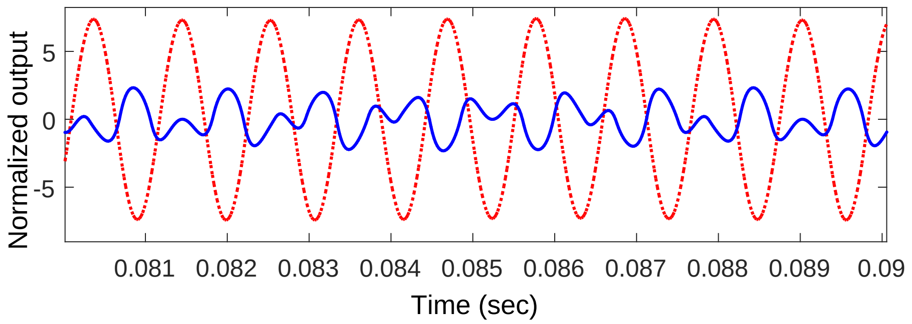

(a) $y_c(t)$ sampled at $T_s/20$. (*The solid and dashed lines represent the cases with single-rate high-gain control on and off, respectively.*)

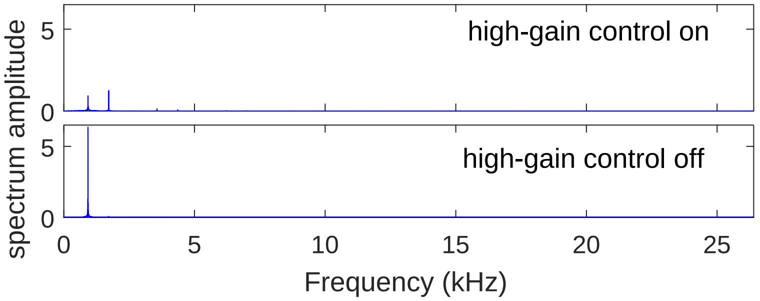

(b) FFT of $y_c(t)$ sampled at $T_s/20$.

Figure 8.12: Plant output with the input disturbance at $0.7\Omega_N$

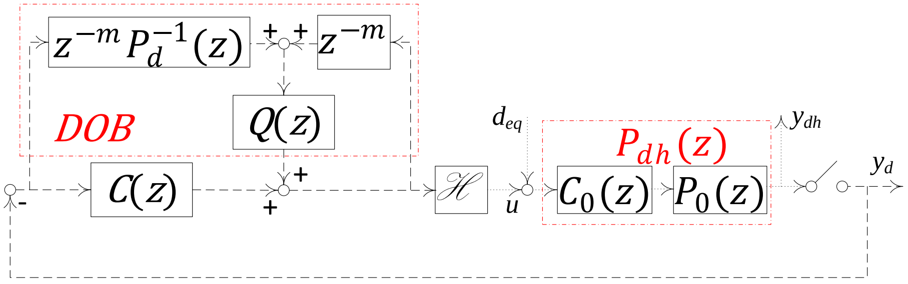

Figure 8.13: Block diagram with a DOB.

As stated in Remark 3, $\mathscr{P}_h(e^{j\Omega_0 T_s'})$ is obtained by means of dividing $\mathscr{P}_h'(e^{j\Omega_0 T_s'})$ by $\left|P_{dh}(e^{j\Omega_0 T_s'})\right|$. Three groups of validations for $\mathscr{P}_h(e^{j\Omega_0 T_s'})$ are shown in Table 8.1 and Fig. 8.15. The results show that the mismatch between the experimental and theoretical values is very small, and thus the modified PFG is an efficient tool for evaluating the intersample behavior. One principal reason

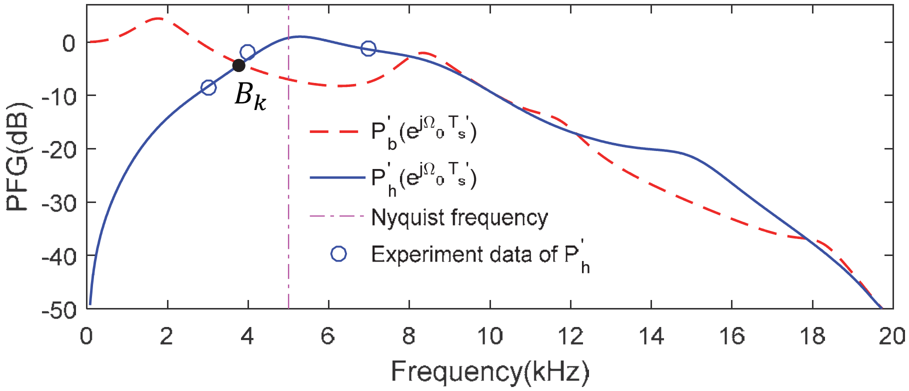

Figure 8.14: Input performance frequency gains (PFGs) with high-gain control on and off.

for the mismatch is that in Definition 1, PFG is evaluated according to $N \to \infty$, while only a finite duration of the signal can be reached in experiments.

Table 8.1: Experimental results of the modified PFG.

Disturbance frequency	Group	Experimental PFGs (dB)	Average	Theoretical PFGs
3 kHz	G1	-1.189	-1.033 dB	-2.847 dB
	G2	-0.961		
	G3	-0.949		
4 kHz	G1	5.481	5.913 dB	4.135 dB
	G2	5.999		
	G3	6.258		
7 kHz	G1	6.023	6.242 dB	6.374 dB
	G2	6.357		
	G3	6.345		

We have already seen the different cases of time-domain responses in Figs. 8.7 and 8.8. Additionally, Fig. 8.16 verifies the performance limitation for disturbances even below the Nyquist frequency. From the slow-sampled data in Figs. 8.7a, 8.8a, and 8.16a, the single-rate DOB is successful in “compensating” the sampled output. However, similar as the case in the

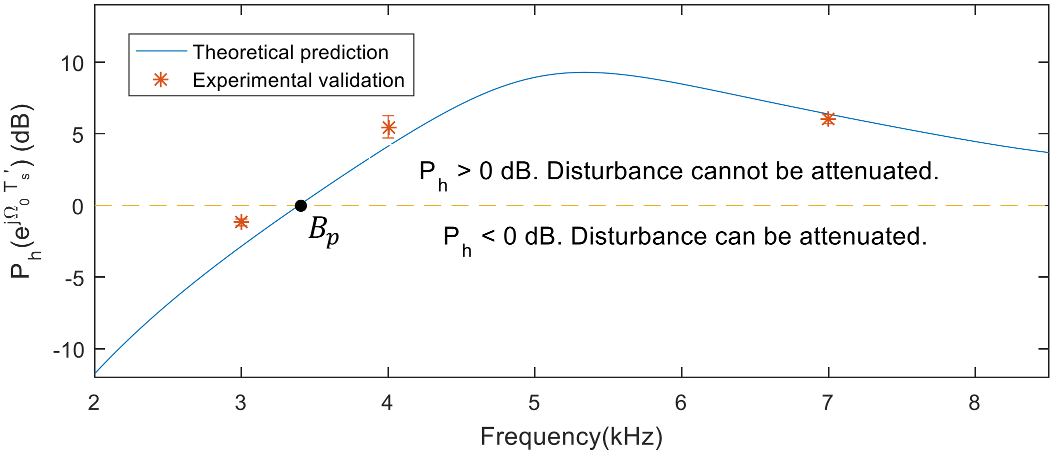

Figure 8.15: Theoretical and experimental PFGs.

previous numerical study, the hidden performance loss for the case with beyond- and *near*-Nyquist disturbances is obvious from Figs. 8.7b and 8.16b.

Fortunately, these performance differences can be predicted by the modified PFG in Fig. 8.15 and the characteristic feedback loop gains in Fig. 8.17. The PFG plots predict that high-gain control results in decreased output power for the disturbance at 3 kHz and increased output energy for the disturbances at 4 kHz and 7 kHz. Fig. 8.17 additionally reveals that both the fundamental and aliased mode gains are increased when disturbances occur at 4 kHz and 7 kHz.

The experimental result in Fig. 8.3 verifies that for the input disturbance with $\Omega_o = 1.4\Omega_N = 7$ kHz, the fundamental component at 7 kHz and the aliased harmonic at 3 kHz are amplified when customized single-rate high-gain control is turned on. For the case with $\Omega_o = 0.8\Omega_N = 4$ kHz, the magnitude of the fundamental mode at 4 kHz barely changes, but the aliased harmonic at 6 kHz is amplified by sub-Nyquist high-gain control, resulting in the overall amplification. For $\Omega_o = 0.6\Omega_N = 3$ kHz, $\left|1-\Gamma_0^*(\Omega_o)\right| < |1-\Gamma_0(\Omega_o)|$, and $|\Gamma_1^*(-\Omega_o)| > |\Gamma_1(-\Omega_o)|$; although the aliased mode at 7 kHz is slightly amplified, the attenuation of the fundamental mode at 3 kHz is significant (Fig. 8.4), resulting in the overall attenuation.

In summary, we experimentally verified that the characteristic feedback loop gains, along with the modified PFG, are reliable tools for analyzing servo performance in sampled-data control. Single-rate high-gain control is observed to amplify all beyond-Nyquist and even some below-Nyquist disturbances.

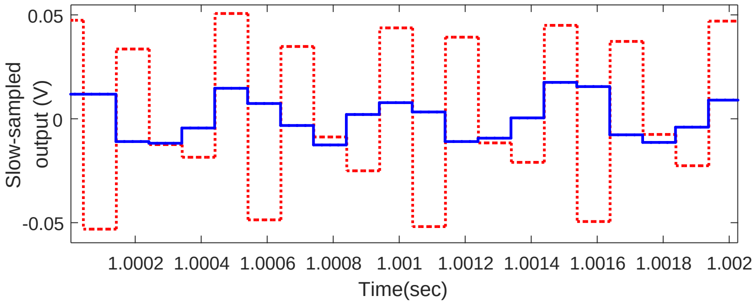

(a) $y_d(t)$ with the sampling time of T_s.

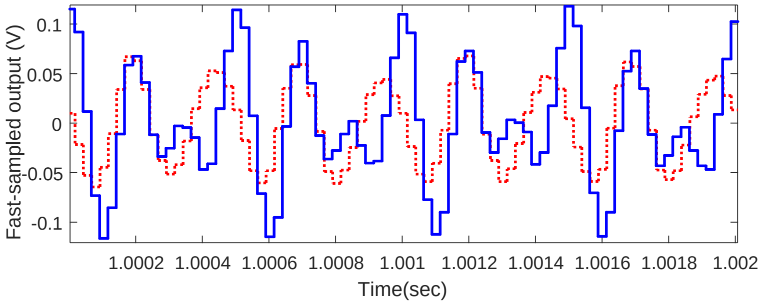

(b) $y_{dh}(t)$ with the sampling time of $T_s^{'}$.

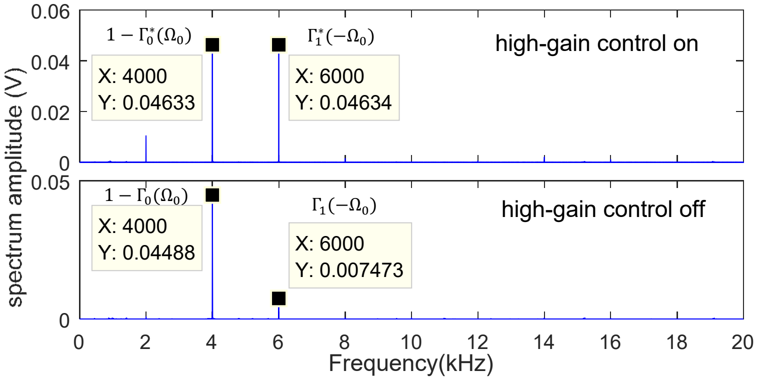

(c) FFT of $y_{dh}(t)$.

Figure 8.16: Plant output with the input disturbance at $0.8\Omega_N$. (*For (a) and (b), the solid and dashed lines represent the cases with single-rate high-gain control on and off, respectively*.)

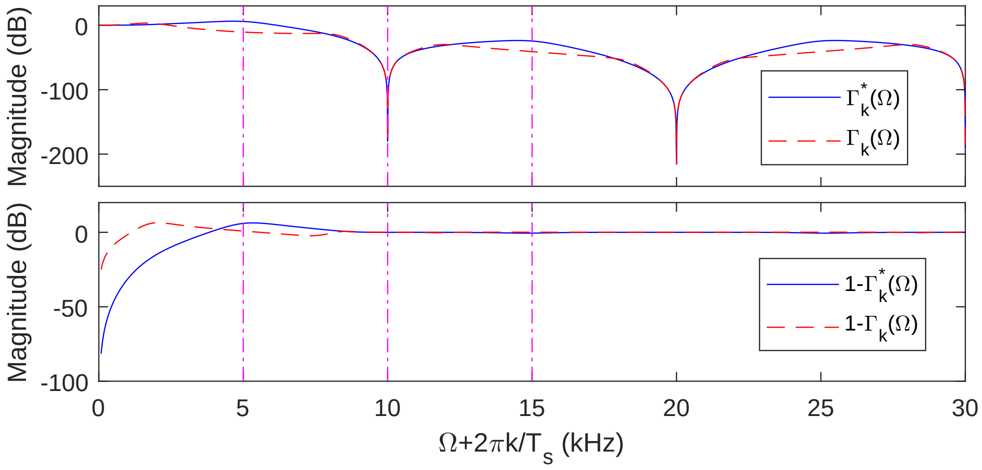

Figure 8.17: Magnitude responses of $\Gamma_k(\Omega)$, $\Gamma_k^*(\Omega)$, $1-\Gamma_k(\Omega)$ and $1-\Gamma_k^*(\Omega)$ as a function of $\Omega+2\pi k/T_s$. The first three vertical lines indicate, respectively, the Nyquist frequency (5 kHz), the sampling frequency, and $^3/_{2T_s}$.

Part III

INTEGRATION

Chapter 9

CASE STUDY: REPETITIVE CONTROL IN CLOSED-LOOP SIMULATION

Under the infrastructure of the closed-loop simulation in Chapter 2, we integrate control-oriented modeling in Part I with feedback control in Part II and evaluate the performance of RC in attenuating the periodic in-layer variations of the melt pool width.

First, we identify the plant model of the FEM in Chapter 3 from the laser power to the melt pool width as $P(s) = 0.001671/(s + 1055)$. The input signals used for system identification include a pseudorandom binary sequence (PRBS) signal and multiple sinusoidal signals (10∼300 Hz), with magnitudes of 20 W and add-on DC components of 60 W. The frequency responses of the measured and identified systems match well with each other, as shown in Fig. 9.1.

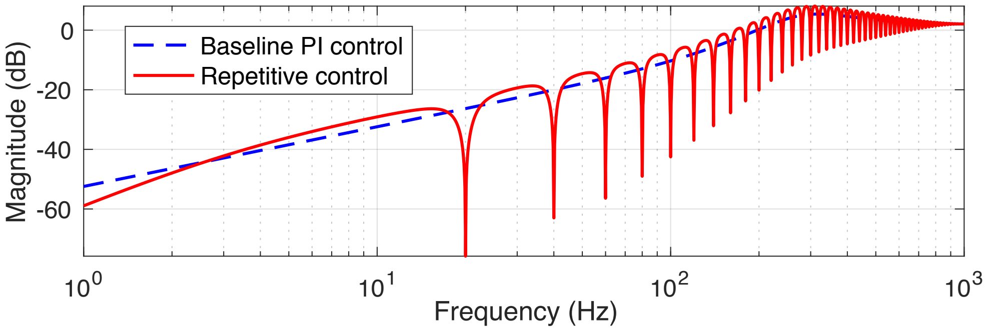

Figure 9.1: Magnitude responses of sensitivity functions $S(z)$ in baseline control and $S_0(z)$ in RC.

After that, we design a PI controller as $C(s) = K_p + K_i/s$ with $K_p = 9.38 \times 10^5$ and $K_i = 1.66 \times 10^9$. Under the sampling time T_s of 0.5 ms (i.e., $f_s = 2\,\text{kHz}$), the ZOH equivalents of the plant and controller models respectively are $P(z) = 6.493 \times 10^{-7}/(z - 0.5901)$ and $C(z) = (9.38z - 1.08) \times 10^5/(z - 1)$. The dashed line in Fig. 9.1 shows the magnitude response of the sensitivity function $S(z)$ in the baseline feedback loop that comprises $P(z)$ and $C(z)$. Such a design provides a bandwidth at 197 Hz, which approximates the limit of 20% of the Nyquist frequency (1 kHz) and indicates that the PI controller is well tuned. The closed-loop simulations are designed according to Chapter 2 integrating FEM with baseline control and RC in Section 6.2, respectively.

In this disturbance-rejection example, $r(k) = 0$ in Fig. 5.3, and $d(k)$ comes from the in-layer melt-pool-width variations (Section 3.3.2). From Fig. 9.2b, we can tell that the baseline PI control can attenuate the frequency spikes below the closed-loop bandwidth but not the other high-frequency spikes. Compared to the case without control, the baseline feedback loop decreases the 3σ value of the melt-pool-width changes ($y(k)$ in Fig. 5.3 with mean removed) by 21.57%, where σ denotes the standard deviation.

To enhance the disturbance-attenuation performance, we bring the plug-in RC compensator in Section 6.2 into the closed-loop high-fidelity simulation. In the Q-filter design in (6.2), the relative degree m of $\hat{P}(z)$ is 1 with $\hat{P}(z)$ being equal to $P(z)$ in this simulation example; the disturbance period $N = f_s/f_0 = 2000/20 = 100$; we choose $\alpha = 0.99$. Also, we attach a low-pass filter with $n_0 = 1$ to $Q(z)$ as in (6.2). As shown in the solid line of Fig. 9.1, the plug-in RC with the Q-filter generates high-gain control efforts exactly at $20\,\text{Hz}$ and its harmonics. Fig. 9.2c illustrates the control signals $u(k)$ of the baseline control, the RC, and the case without control. As shown in Fig. 9.2b, compared with the baseline control, RC further lowers the periodic frequency spikes, especially at high frequencies beyond the closed-loop bandwidth, and decreases the 3σ value by 35.97%. Similarly, in the time domain, the increased control efforts of RC at the harmonic frequencies yield a further-attenuated output $y(k)$, as shown in Fig. 9.2a.

Remark 4. *Practical feedback design has an effective servo bandwidth, above which the control efforts are required to be small for robustness. The baseline PI control and the Q-filter with* $q_0(z^{-1})q_0(z)$ *are designed to account for this constraint. As shown in Fig. 9.1, above approximately 650 Hz, the magnitudes of the sensitivity functions of baseline PI control and RC are close to zero, leaving the corresponding frequency components unchanged.*

Remark 5. *To compute the closed-loop simulation with the FEM in Chapter 3, it takes approximately 19 seconds for one time step of* $0.5\,ms$*, 32 minutes for a track of length 5 mm, and 4.5 hours for ten tracks of length 5 mm using two Intel Xeon Gold 6146 CPUs at 3.20 GHz with 24 cores in total.*

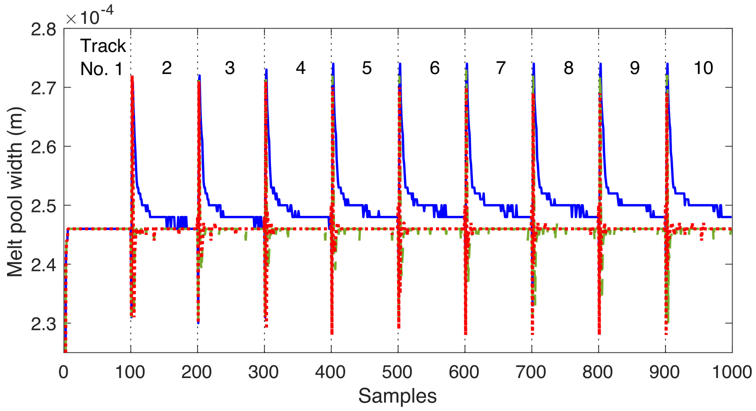

(a) Evolution of melt pool width (time-domain)

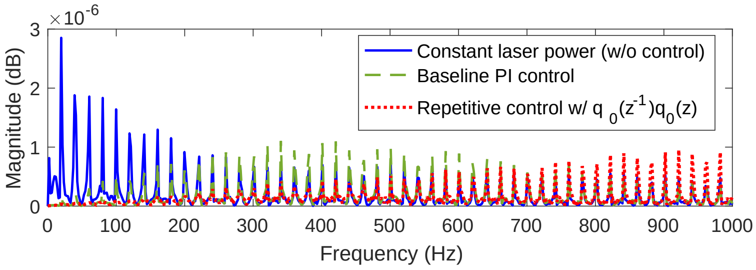

(b) FFT of melt-pool-width evolution (frequency-domain)

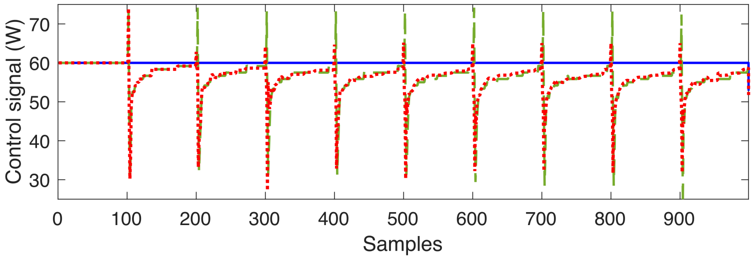

(c) Laser power (control signals $u(k)$ in Fig. 5.3)

Figure 9.2: In-layer thermal disturbance. The three plots share the same legend. The 3σ-values of the melt pool width respectively are $15.219\,\mu\text{m}$ for constant laser power, $11.937\,\mu\text{m}$ (21.6% decrease) for baseline PI control, and $9.744\,\mu\text{m}$ (35.97% decrease) for RC. σ denotes the standard deviation. The earlier results in Fig. 3.6 are superimposed in Figs. 9.2a and 9.2b for clarity.

Chapter 10

CONCLUSIONS AND FUTURE WORK

In this dissertation, we develop a first-instance closed-loop high-fidelity simulation architecture by integrating finite element model (FEM) with feedback controls to reduce the in-process variations and advance the part quality in laser powder bed fusion (LPBF) additive manufacturing. Under the infrastructure of the closed-loop simulation, we investigate the control-oriented modeling and multirate feedback control, respectively. We draw the following conclusions from our study and present some potential avenues for future work.

Finite Element Modeling

We build an FEM to simulate the temperature response in LPBF and then validate the FEM by comparing its results with the experimental and analytical solutions. Employing the FEM, we justify the existence of the periodic disturbances in the evolution of the melt pool width.

New Hammerstein Mixed-fidelity Modeling

Using the FEM data, we identify around the equilibrium point the linear system model from the laser power to the melt pool width. In addition, deriving from the Rosenthal equation, we reach a nonlinear closed-form expression of the steady-state melt pool width. Concatenating the nonlinear expression to the identified linear model, we develop the main Hammerstein model that captures more of the convoluted thermomechanical dynamics of LPBF. We prove that the Hammerstein mode gives a better approximation (e.g., 41% increasing at 10 Hz) of the FEM result than the linear model. From there, we analyze the stability and robustness properties of the models and present a generic control scheme for the Hammerstein Model.

Loop-shaping Control

In this dissertation, the control methodologies for precision positioning systems have been studied. The central concept is that flexible loop shaping is a convenient tool for addressing various servo problems. Multiple simulation and experimental results on actual engineering problems (e.g., the galvo scanner platform in LPBF) are used to validate the presented designs. Besides the examples given in this dissertation, the control structure has also been tested under other systems, such as electrical power steering in automotive vehicles [59] and active suspension systems [40, 51].

Fractional-order Repetitive Control

Based on the loop-shaping control methodologies, we build three specific repetitive control (RC) algorithms to overcome the intrinsic limitation of the RC internal model $1/(1-z^{-N})$ under fractional-order situations that arise in LPBF. To apply repetitive error rejection when the fundamental disturbance frequency does not divide the sampling frequency, the wide-band RC scheme widens the attenuation widths to include the desired frequencies of the periodic disturbance. The quasi RC method, on the other hand, creates an integer N by selecting the greatest common divisor of the sampling and fundamental disturbance frequencies as the fictitious fundamental frequency. The multirate RC applies a new fast sampling frequency that allows for exact attenuation at the desired repetitive frequencies. Numerical and experimental results verify the effectiveness of all three algorithms, and the multirate RC algorithm outperforms the wide-band and quasi ones by providing more systematic, precise servo enhancement, particularly at high frequencies.

H_∞-based Model Inversion

Model inversion is fundamental to subsequent servo designs, such as the RC design. We discuss new frequency-domain analysis and design approaches to invert a nonminimum-phase (NMP) linear time-invariant system, with a focus on robustness and needed design constraints in feedback implementations. We reveal that among existing model inversion techniques, the H_∞-based method stands out by automatically identifying the inverse model without knowing the exact NMP zeros. Furthermore, we illustrated that modulating the location of the NMP zero only changes the system response at selective frequency regions. Leveraging this fact, for general NMP systems, we propose a discrete-time H_∞-based optimal inversion to automatically design the inverse model for selective frequency regions defined by two weighting functions. Verification in complex high-order systems and unstable systems shows the strengths of the proposed algorithm.

Multirate Spectral Analysis near and Beyond Nyquist Frequency

We analyze the problem of sampled-data regulation control against structured disturbances around and beyond the Nyquist frequency. It is shown that the conventional sub-Nyquist single-rate high-gain control is infeasible to attenuate disturbances near and beyond the Nyquist frequency.

We discover an intersection frequency defined as the principal sampled-data bandwidth B_p. Only for below-B_p disturbances can single-rate high-gain control be effective in disturbance rejection. A spectral analysis is further proposed to look into individual spectral modes. The proposed characteristic feedback loop gains are combined with the performance frequency gain to evaluate the overall sampled-data performance. The results imply that the rejection of beyond-Nyquist vibration disturbances must rely on tools that can facilitate the intersample attenuation, such as customized multirate control [150], sampled-data internal model principle [151], sampled-data LQG [152], sampled-data all-stabilizing control [153], and sampled-data H_∞ theory (see [154] and the references therein). For potential future work, the proposed study may have synergy with the analysis and design of nonlinear systems in the frequency domain (e.g., [155–157]).

Case Study: Repetitive Control in Closed-loop Simulation

Implementing the proposed closed-loop simulation, we validate that the RC algorithm attenuates the in-layer periodic thermal disturbances in LPBF more substantially by 35.97% than the PI control. One avenue for future work is to expand the proposed closed-loop simulation to be used in multi-layer printing when macroscopic features begin to form. The proposed architecture enables simulating in the FEM the development of the macroscopic temperature history and the melt pool geometries under the influence of feedback controls. To relieve the computation burden incurred by the high-fidelity simulation of multiple layers, we can start with a thin-wall build with small numbers of tracks (say one or two) within one layer. Another avenue for future work is to bring the closed-loop simulation to experiments and experimentally verify the effectiveness of RC.

BIBLIOGRAPHY

[1] D. Wang and X. Chen, "A multirate fractional-order repetitive control for laser-based additive manufacturing," *Control Engineering Practice*, vol. 77, pp. 41–51, 2018.

[2] J.-P. Kruth, P. Mercelis, J. Van Vaerenbergh, and T. Craeghs, "Feedback control of selective laser melting," in *Proceedings of the 3rd international conference on advanced research in virtual and rapid prototyping*, pp. 521–527, 2007.

[3] V. Seyda, N. Kaufmann, and C. Emmelmann, "Investigation of aging processes of ti-6al-4 v powder material in laser melting," *Physics Procedia*, vol. 39, pp. 425–431, 2012.

[4] M. Masoomi, S. M. Thompson, and N. Shamsaei, "Laser powder bed fusion of ti-6al-4v parts: Thermal modeling and mechanical implications," *International Journal of Machine Tools and Manufacture*, vol. 118, pp. 73–90, 2017.

[5] A. Hussein, L. Hao, C. Yan, and R. Everson, "Finite element simulation of the temperature and stress fields in single layers built without-support in selective laser melting," *Materials & Design (1980-2015)*, vol. 52, pp. 638–647, 2013.

[6] A. Foroozmehr, M. Badrossamay, E. Foroozmehr, and S. Golabi, "Finite element simulation of selective laser melting process considering optical penetration depth of laser in powder bed," *Materials & Design*, vol. 89, pp. 255–263, 2016.

[7] S. A. Khairallah, A. T. Anderson, A. Rubenchik, and W. E. King, "Laser powder-bed fusion additive manufacturing: Physics of complex melt flow and formation mechanisms of pores, spatter, and denudation zones," *Acta Materialia*, vol. 108, pp. 36–45, 2016.

[8] T. Debroy, W. Zhang, J. Turner, and S. S. Babu, "Building digital twins of 3d printing machines," *Scripta Materialia*, vol. 135, pp. 119–124, 2017.

[9] T. Craeghs, F. Bechmann, S. Berumen, and J.-P. Kruth, "Feedback control of layerwise laser melting using optical sensors," *Physics Procedia*, vol. 5, pp. 505–514, 2010.

[10] C. Zheng, J. T. Wen, and M. Diagne, "Distributed temperature control in laser-based manufacturing," *Journal of Dynamic Systems, Measurement, and Control*, vol. 142, no. 6, 2020.

[11] L. Song and J. Mazumder, "Feedback control of melt pool temperature during laser cladding process," *IEEE Transactions on Control Systems Technology*, vol. 19, no. 6, pp. 1349–1356, 2011.

[12] X. Cao and B. Ayalew, "Control-oriented mimo modeling of laser-aided powder deposition processes," in *American Control Conference (ACC), 2015*, pp. 3637–3642, IEEE, 2015.

[13] P. M. Sammons, D. A. Bristow, and R. G. Landers, "Repetitive process control of laser metal deposition," in *ASME 2014 Dynamic Systems and Control Conference*, pp. V002T35A004–V002T35A004, American Society of Mechanical Engineers, 2014.

[14] A. Fathi, A. Khajepour, M. Durali, and E. Toyserkani, "Geometry control of the deposited layer in a nonplanar laser cladding process using a variable structure controller," *Journal of manufacturing science and engineering*, vol. 130, no. 3, p. 031003, 2008.

[15] M. L. Vlasea, B. Lane, F. Lopez, S. Mekhontsev, and A. Donmez, "Development of powder bed fusion additive manufacturing test bed for enhanced real-time process control," in *Proceedings of the international solid freeform fabrication symposium, Austin, TX, USA*, pp. 13–15, 2015.

[16] T. G. Fleming, S. G. Nestor, T. R. Allen, M. A. Boukhaled, N. J. Smith, and J. M. Fraser, "Tracking and controlling the morphology evolution of 3d powder-bed fusion in situ using inline coherent imaging," *Additive Manufacturing*, vol. 32, p. 100978, 2020.

[17] J. Hofman, B. Pathiraj, J. Van Dijk, D. de Lange, and J. Meijer, "A camera based feedback control strategy for the laser cladding process," *Journal of Materials Processing Technology*, vol. 212, no. 11, pp. 2455–2462, 2012.

[18] D. Salehi and M. Brandt, "Melt pool temperature control using labview in nd: Yag laser blown powder cladding process," *The international journal of advanced manufacturing technology*, vol. 29, no. 3, pp. 273–278, 2006.

[19] A. Fathi, A. Khajepour, E. Toyserkani, and M. Durali, "Clad height control in laser solid freeform fabrication using a feedforward pid controller," *The International Journal of Advanced Manufacturing Technology*, vol. 35, no. 3, pp. 280–292, 2007.

[20] L. Tang and R. G. Landers, "Layer-to-layer height control for laser metal deposition process," *Journal of Manufacturing Science and Engineering*, vol. 133, no. 2, p. 021009, 2011.

[21] Z. Luo and Y. Zhao, "A survey of finite element analysis of temperature and thermal stress fields in powder bed fusion additive manufacturing," *Additive Manufacturing*, vol. 21, pp. 318–332, 2018.

[22] T. Mukherjee, H. Wei, A. De, and T. DebRoy, "Heat and fluid flow in additive manufacturing—part i: Modeling of powder bed fusion," *Computational Materials Science*, vol. 150, pp. 304–313, 2018.

[23] E. Kannatey-Asibu Jr, *Principles of laser materials processing*, vol. 4. John Wiley & Sons, 2009.

[24] I. Yadroitsev, P. Krakhmalev, and I. Yadroitsava, "Selective laser melting of ti6al4v alloy for biomedical applications: Temperature monitoring and microstructural evolution," *Journal of Alloys and Compounds*, vol. 583, pp. 404–409, 2014.

[25] A. N. Arce, *Thermal modeling and simulation of electron beam melting for rapid prototyping on Ti6Al4V alloys*. North Carolina State University, 2012.

[26] K. C. Mills, *Recommended values of thermophysical properties for selected commercial alloys*. Woodhead Publishing, 2002.

[27] K. Karayagiz, A. Elwany, G. Tapia, B. Franco, L. Johnson, J. Ma, I. Karaman, and R. Arróyave, "Numerical and experimental analysis of heat distribution in the laser powder bed fusion of ti-6al-4v," *IISE Transactions*, vol. 51, no. 2, pp. 136–152, 2019.

[28] J. Yin, H. Zhu, L. Ke, W. Lei, C. Dai, and D. Zuo, "Simulation of temperature distribution in single metallic powder layer for laser micro-sintering," *Computational Materials Science*, vol. 53, no. 1, pp. 333–339, 2012.

[29] I. Yadroitsev, *Selective laser melting: Direct manufacturing of 3D-objects by selective laser melting of metal powders*. LAP LAMBERT Academic Publishing, 09 2009.

[30] C. Cepeda-Jiménez, F. Potenza, E. Magalini, V. Luchin, A. Molinari, and M. Pérez-Prado, "Effect of energy density on the microstructure and texture evolution of ti-6al-4v manufactured by laser powder bed fusion," *Materials Characterization*, p. 110238, 2020.

[31] L. Thijs, F. Verhaeghe, T. Craeghs, J. Van Humbeeck, and J.-P. Kruth, "A study of the microstructural evolution during selective laser melting of ti–6al–4v," *Acta materialia*, vol. 58, no. 9, pp. 3303–3312, 2010.

[32] T. Majumdar, T. Bazin, E. Massahud Carvalho Ribeiro, J. E. Frith, and N. Birbilis, "Understanding the effects of pbf process parameter interplay on ti-6al-4v surface properties," *PloS one*, vol. 14, no. 8, p. e0221198, 2019.

[33] A. J. Dunbar, E. R. Denlinger, M. F. Gouge, T. W. Simpson, and P. Michaleris, "Comparisons of laser powder bed fusion additive manufacturing builds through experimental in situ distortion and temperature measurements," *Additive Manufacturing*, vol. 15, pp. 57–65, 2017.

[34] X. Chen and M. Tomizuka, “New repetitive control with improved steady-state performance and accelerated transient,” *IEEE Transactions on Control Systems Technology*, vol. 22, no. 2, pp. 664–675, 2014.

[35] S. Liu and Y. C. Shin, “Additive manufacturing of ti6al4v alloy: A review,” *Materials & Design*, vol. 164, p. 107552, 2019.

[36] Z. Rayouf, C. Ghorbel, and N. B. Braiek, “A new hammerstein model control strategy: feedback stabilization and stability analysis,” *International Journal of Dynamics and Control*, vol. 7, no. 4, pp. 1453–1461, 2019.

[37] F. J. Doyle, R. K. Pearson, and B. A. Ogunnaike, *Identification and control using Volterra models*. Springer, 2002.

[38] X. Ren and X. Lv, “Identification of extended hammerstein systems using dynamic self-optimizing neural networks,” *IEEE Transactions on Neural Networks*, vol. 22, no. 8, pp. 1169–1179, 2011.

[39] M. Tang, P. C. Pistorius, and J. L. Beuth, “Prediction of lack-of-fusion porosity for powder bed fusion,” *Additive Manufacturing*, vol. 14, pp. 39–48, 2017.

[40] X. Chen and M. Tomizuka, “Selective model inversion and adaptive disturbance observer for rejection of time-varying vibrations on an active suspension,” in *Control Conference (ECC), 2013 European*, pp. 2897–2903, IEEE, 2013.

[41] J. C. Doyle, B. A. Francis, and A. R. Tannenbaum, *Feedback control theory*. Courier Corporation, 2013.

[42] D. Wang, M. Tomizuka, and X. Chen, “Spectral distribution and implications of feedback regulation beyond nyquist frequency,” in *Flexible Automation (ISFA), International Symposium on*, pp. 23–30, IEEE, 2016.

[43] T. Atsumi and W. C. Messner, “Compensating for zoh-induced residual vibrations in head-positioning control of hard disk drives,” *IEEE/ASME Transactions on Mechatronics*, vol. 19, no. 1, pp. 258–268, 2014.

[44] T. Oomen, R. van Herpen, S. Quist, M. van de Wal, O. Bosgra, and M. Steinbuch, “Connecting system identification and robust control for next-generation motion control of a wafer stage,” *IEEE Transactions on Control Systems Technology*, vol. 22, no. 1, pp. 102–118, 2014.

[45] Y. Li, G. Guo, and Y. Wang, “Reset control for midfrequency narrowband disturbance rejection with an application in hard disk drives,” *IEEE Transactions on Control Systems Technology*, vol. 19, no. 6, pp. 1339–1348, 2011.

[46] L. Sievers and A. von Flotow, “Comparison and extensions of control methods for narrow-band disturbance rejection,” *IEEE Transactions on Signal Processing*, vol. 40, no. 10, pp. 2377–2391, 1992.

[47] M. Bodson, “Adaptive algorithms for the rejection of sinusoidal disturbances with unknown frequency,” *Automatica*, vol. 33, pp. 2213–2221, Dec. 1997.

[48] X. Chen and H. Xiao, “Multirate forward-model disturbance observer for feedback regulation beyond nyquist frequency,” *Systems & Control Letters*, vol. 94, pp. 181–188, 2016.

[49] X. Chen and M. Tomizuka, “A minimum parameter adaptive approach for rejecting multiple narrow-band disturbances with application to hard disk drives,” *IEEE Transactions on Control Systems Technology*, vol. 20, pp. 408–415, Mar. 2012.

[50] M. Zheng, C. Wang, L. Sun, and M. Tomizuka, “Design of arbitrary-order robust iterative learning control based on robust control theory,” *Mechatronics*, vol. 47, pp. 67–76, 2017.

[51] I. D. Landau, A. Constantinescu, and D. Rey, “Adaptive narrow band disturbance rejection applied to an active suspension–an internal model principle approach,” *Automatica*, vol. 41, no. 4, pp. 563–574, 2005.

[52] I. D. Landau, A. C. Silva, T.-B. Airimitoaie, G. Buche, and M. Noe, “Benchmark on adaptive regulation–rejection of unknown/time-varying multiple narrow band disturbances,” *European Journal of Control*, vol. 19, no. 4, pp. 237–252, 2013.

[53] D. Youla, J. Bongiorno Jr, and H. Jabr, “Modern wiener–hopf design of optimal controllers part i: the single-input-output case,” *IEEE Transactions on Automatic Control*, vol. 21, no. 1, pp. 3–13, 1976.

[54] V. Kucera, “Stability of discrete linear feedback systems,” in *Proc. 6th IFAC World Congress, paper 44.1*, vol. 1, 1975.

[55] M. Steinbuch, S. Weiland, and T. Singh, “Design of noise and period-time robust high-order repetitive control, with application to optical storage,” *Automatica*, vol. 43, no. 12, pp. 2086–2095, 2007.

[56] R. A. de Callafon and H. Fang, “Adaptive regulation via weighted robust estimation and automatic controller tuning,” *European Journal of Control*, vol. 19, no. 4, pp. 266–278, 2013.

[57] B. Widrow, J. R. Glover, J. M. McCool, J. Kaunitz, C. S. Williams, R. H. Hearn, J. R. Zeidler, J. E. Dong, and R. C. Goodlin, “Adaptive noise cancelling: Principles and applications,” *Proceedings of the IEEE*, vol. 63, no. 12, pp. 1692–1716, 1975.

[58] L. Sun, X. Chen, and M. Tomizuka, “Enhanced wide-spectrum vibration suppression based on adaptive loop shaping,” in *American Control Conference (ACC), 2016*, pp. 6189–6194, IEEE, 2016.

[59] X. Chen, A. Oshima, and M. Tomizuka, “Inverse-based local loop shaping and iir-filter design for precision motion control,” *IFAC Proceedings Volumes*, vol. 46, no. 5, pp. 490–497, 2013.

[60] X. Chen and M. Tomizuka, “Optimal decoupled disturbance observers for dual-input single-output systems,” *Journal of Dynamic Systems, Measurement, and Control*, vol. 136, no. 5, p. 051018, 2014.

[61] J. Keane, *Full state feedback control of galvanometer scanning system*. PhD thesis, Dublin City University, 1994.

[62] T. Mirtchev, R. Weeks, and S. Minko, “Optimizing the feedback control of galvo scanners for laser manufacturing systems,” in *Proc. of SPIE Vol*, vol. 7750, pp. 77500T–1, 2010.

[63] J. G. Ziegler and N. B. Nichols, “Optimum settings for automatic controllers,” *trans. ASME*, vol. 64, no. 11, 1942.

[64] X. Chen and M. Tomizuka, “Unknown multiple narrow-band disturbance rejection in hard disk drives: An adaptive notch filter and perfect disturbance observer approach,” in *ASME 2010 Dynamic Systems and Control Conference*, pp. 963–970, American Society of Mechanical Engineers, 2010.

[65] B. D. Anderson, “From youla kucera to identification, adaptive and nonlinear control,” *Automatica*, vol. 34, no. 12, pp. 1485–1506, 1998.

[66] B. Widrow and E. Walach, *Adaptive Inverse Control, Reissue Edition: A Signal Processing Approach*. Wiley-IEEE Press, Nov. 2007.

[67] T. Inoue, M. Nakano, T. Kubo, S. Matsumoto, and H. Baba, “High accuracy control of a proton synchrotron magnet power supply,” *IFAC Proceedings Volumes*, vol. 14, no. 2, pp. 3137–3142, 1981.

[68] K. K. Chew and M. Tomizuka, “Digital control of repetitive errors in disk drive systems,” in *American Control Conf., 1989*, pp. 540–548, IEEE, 1989.

[69] T.-Y. Doh, J. Ryoo, and M. Chung, “Design of a repetitive controller: an application to the track-following servo system of optical disk drives,” *IEE Proceedings-Control Theory and Applications*, vol. 153, no. 3, pp. 323–330, 2006.

[70] X. Chen and M. Tomizuka, "New repetitive control with improved steady-state performance and accelerated transient," *IEEE Transactions on Control Systems Technology*, vol. 22, pp. 664–675, Mar. 2014.

[71] C. Cosner, G. Anwar, and M. Tomizuka, "Plug in repetitive control for industrial robotic manipulators," in *Robotics and Automation, 1990. Proceedings., 1990 IEEE Int. Conf. on*, pp. 1970–1975, IEEE, 1990.

[72] W. Meng, S. Q. Xie, Q. Liu, C. Z. Lu, and Q. Ai, "Robust iterative feedback tuning control of a compliant rehabilitation robot for repetitive ankle training," *IEEE/ASME Trans. Mechatronics*, vol. 22, no. 1, pp. 173–184, 2017.

[73] S. Navalkar, J. Van Wingerden, E. Van Solingen, T. Oomen, E. Pasterkamp, and G. Van Kuik, "Subspace predictive repetitive control to mitigate periodic loads on large scale wind turbines," *Mechatronics*, vol. 24, no. 8, pp. 916–925, 2014.

[74] R. S. Castro, A. T. Salton, J. V. Flores, M. Kinnaert, and D. F. Coutinho, "Variable frequency resonant controller for load reduction in wind turbines," *Control Eng. Pract.*, vol. 66, pp. 76–88, 2017.

[75] R. Nazir, K. Zhou, N. Watson, and A. Wood, "Analysis and synthesis of fractional order repetitive control for power converters," *Electr. Power Syst. Res.*, vol. 124, pp. 110–119, 2015.

[76] X. He, D. Guo, and K. K. Leang, "Repetitive control design and implementation for periodic motion tracking in aerial robots," in *American Control Conf., 2017*, pp. 5101–5108, IEEE, 2017.

[77] L. N. Carter, C. Martin, P. J. Withers, and M. M. Attallah, "The influence of the laser scan strategy on grain structure and cracking behaviour in slm powder-bed fabricated nickel superalloy," *J. Alloys Compd.*, vol. 615, pp. 338–347, 2014.

[78] J.-P. Kruth, L. Froyen, J. Van Vaerenbergh, P. Mercelis, M. Rombouts, and B. Lauwers, "Selective laser melting of iron-based powder," *J. Mater. Process. Technol.*, vol. 149, no. 1, pp. 616–622, 2004.

[79] A. Simchi and H. Pohl, "Effects of laser sintering processing parameters on the microstructure and densification of iron powder," *Mater. Science and Eng.: A*, vol. 359, no. 1, pp. 119–128, 2003.

[80] D. J. Hoelzle and K. L. Barton, "On spatial iterative learning control via 2-d convolution: Stability analysis and computational efficiency," *IEEE Trans. Control Syst. Technol.*, vol. 24, no. 4, pp. 1504–1512, 2016.

[81] I. Lim, D. J. Hoelzle, and K. L. Barton, “A multi-objective iterative learning control approach for additive manufacturing applications,” *Control Eng. Pract.*, vol. 64, pp. 74–87, 2017.

[82] A. Heralić, A.-K. Christiansson, and B. Lennartson, “Height control of laser metal-wire deposition based on iterative learning control and 3d scanning,” *Opt. Lasers Eng.*, vol. 50, no. 9, pp. 1230–1241, 2012.

[83] B. A. Francis and W. M. Wonham, “The internal model principle for linear multivariable regulators,” *Appl. Math. Optim.*, vol. 2, no. 2, pp. 170–194, 1975.

[84] S. Hara, Y. Yamamoto, T. Omata, and M. Nakano, “Repetitive control system: A new type servo system for periodic exogenous signals,” *IEEE Trans. Autom. Control*, vol. 33, no. 7, pp. 659–668, 1988.

[85] G. A. Ramos and R. Costa-Castelló, “Power factor correction and harmonic compensation using second-order odd-harmonic repetitive control,” *IET control theory & applications*, vol. 6, no. 11, pp. 1633–1644, 2012.

[86] M. Nakano, J.-H. She, Y. Mastuo, and T. Hino, “Elimination of position-dependent disturbances in constant-speed-rotation control systems,” *Control Eng. Pract.*, vol. 4, no. 9, pp. 1241–1248, 1996.

[87] W.-S. Yao, M.-C. Tsai, and Y. Yamamoto, “Implementation of repetitive controller for rejection of position-based periodic disturbances,” *Control Eng. Pract.*, vol. 21, no. 9, pp. 1226–1237, 2013.

[88] Z. Chen, K. Yamada, T. Sakanushi, and Y. Zhao, “Linear matrix inequality-based repetitive controller design for linear systems with time-varying uncertainties to reject position-dependent disturbances,” *Int. J. Innovative Comput. Inf. Control*, vol. 9, no. 8, pp. 3241–3256, 2013.

[89] Z. Cao and G. F. Ledwich, “Adaptive repetitive control to track variable periodic signals with fixed sampling rate,” *IEEE/ASME Trans. Mechatronics*, vol. 7, no. 3, pp. 378–384, 2002.

[90] E. Kurniawan, Z. Cao, and Z. Man, “Adaptive repetitive control of system subject to periodic disturbance with time-varying frequency,” in *Informatics and Computational Intelligence (ICI), 2011 First Int. Conf. on*, pp. 185–190, IEEE, 2011.

[91] R. J. Merry, D. Kessels, W. Heemels, M. Van De Molengraft, and M. Steinbuch, “Delay-varying repetitive control with application to a walking piezo actuator,” *Automatica*, vol. 47, no. 8, pp. 1737–1743, 2011.

[92] Z. Liu, B. Zhang, and K. Zhou, “Universal fractional-order design of linear phase lead compensation multirate repetitive control for pwm inverters,” *IEEE Transactions on Industrial Electronics*, vol. 64, no. 9, pp. 7132–7140, 2017.

[93] Z.-X. Zou, K. Zhou, Z. Wang, and M. Cheng, “Frequency-adaptive fractional-order repetitive control of shunt active power filters,” *IEEE Trans. Ind. Electron.*, vol. 62, no. 3, pp. 1659–1668, 2015.

[94] T. Liu, D. Wang, and K. Zhou, “High-performance grid simulator using parallel structure fractional repetitive control,” *IEEE Trans. Power Electron.*, vol. 31, no. 3, pp. 2669–2679, 2016.

[95] W. G. Jung, *Op Amp applications handbook.* Newnes, 2005.

[96] I. Cambridge Technologies, *MicroMax 671 Series broad level single axis driver electronics*, 2008.

[97] H. W. Bode, *Network Analysis and Feedback Amplifier Design.* Princeton, NJ, USA: Van Nostrand, 1945.

[98] X. Chen and M. Tomizuka, “Control methodologies for precision positioning systems,” in *Proceedings of American Control Conference*, pp. 3710–3717, June 2013.

[99] D. Wang and X. Chen, “A tutorial on loop-shaping control methodologies for precision positioning systems,” *Advances in Mechanical Engineering*, vol. 9, no. 12, p. 1687814017742824, 2017.

[100] D. Bristow, M. Tharayil, and A. G. Alleyne, “A survey of iterative learning control,” *IEEE Control Systems Magazine*, vol. 26, no. 3, pp. 96–114, 2006.

[101] D. Shen, “Iterative learning control with incomplete information: A survey,” *IEEE/CAA Journal of Automatica Sinica*, vol. 5, no. 5, pp. 885–901, 2018.

[102] R. de Rozario and T. Oomen, “Data-driven iterative inversion-based control: Achieving robustness through nonlinear learning,” *Automatica*, vol. 107, pp. 342–352, 2019.

[103] S. Zhu, X. Wang, and H. Liu, “Observer-based iterative and repetitive learning control for a class of nonlinear systems,” *IEEE/CAA Journal of Automatica Sinica*, vol. 5, no. 5, pp. 990–998, 2017.

[104] Y. Li and M. Tomizuka, “Two-degree-of-freedom control with robust feedback control for hard disk servo systems,” *IEEE/ASME Transactions on Mechatronics*, vol. 4, pp. 17–24, Mar. 1999.

[105] C. Wang, M. Zheng, Z. Wang, and M. Tomizuka, “Robust two-degree-of-freedom iterative learning control for flexibility compensation of industrial robot manipulators,” in *2016 IEEE International Conference on Robotics and Automation (ICRA)*, pp. 2381–2386, IEEE, 2016.

[106] T. Jiang, H. Xiao, J. Tang, L. Sun, and X. Chen, “Local loop shaping for rejecting band-limited disturbances in nonminimum-phase systems with application to laser beam steering for additive manufacturing,” *IEEE Transactions on Control Systems Technology*, 2019.

[107] K. Ohnishi, “Robust motion control by disturbance observer,” *Journal of the Robotics Society of Japan*, vol. 11, no. 4, pp. 486–493, 1993.

[108] X. Chen and M. Tomizuka, “A minimum parameter adaptive approach for rejecting multiple narrow-band disturbances with application to hard disk drives,” *IEEE Transactions on Control Systems Technology*, vol. 20, no. 2, pp. 408–415, 2011.

[109] A. Apte, U. Thakar, and V. Joshi, “Disturbance observer based speed control of pmsm using fractional order pi controller,” *IEEE/CAA Journal of Automatica Sinica*, vol. 6, no. 1, pp. 316–326, 2019.

[110] K. Astrom, P. Hagander, and J. Sternby, “Zeros of sampled systems,” *Automatica*, vol. 20, no. 1, pp. 31–38, 1984.

[111] M. Tomizuka, “Zero phase error tracking algorithm for digital control,” *ASME Journal of Dynamic Systems, Measurement, and Control*, vol. 109, no. 1, pp. 65–68, 1987.

[112] L. Dai, X. Li, Y. Zhu, and M. Zhang, “Quantitative analysis on tracking error under different control architectures and feedforward methods,” in *2019 American Control Conference (ACC)*, pp. 5680–5686, IEEE, 2019.

[113] J. A. Butterworth, L. Y. Pao, and D. Y. Abramovitch, “Analysis and comparison of three discrete-time feedforward model-inverse control techniques for nonminimum-phase systems,” *Mechatronics*, vol. 22, no. 5, pp. 577–587, 2012.

[114] J. a. Butterworth, L. Y. Pao, and D. Y. Abramovitch, “The effect of nonminimum-phase zero locations on the performance of feedforward model-inverse control techniques in discrete-time systems,” *Proceedings of American Control Conference*, pp. 2696–2702, June 2008.

[115] S. Devasia, “Iterative machine learning for output tracking,” *IEEE Transactions on Control Systems Technology*, vol. 27, no. 2, pp. 516–526, 2017.

[116] K.-S. Kim and Q. Zou, “A Modeling-Free Inversion-Based Iterative Feedforward Control for Precision Output Tracking of Linear Time-Invariant Systems,” *IEEE/ASME Transactions on Mechatronics*, vol. 18, no. 6, pp. 1767–1777, 2013.

[117] C.-W. Chen and T.-C. Tsao, "Data-based feedforward controller reconstruction from iterative learning control algorithm," in *2016 IEEE International Conference on Advanced Intelligent Mechatronics (AIM)*, pp. 683–688, IEEE, 2016.

[118] M. Zheng, F. Zhang, and X. Liang, "A systematic design framework for iterative learning control with current feedback," *IFAC Journal of Systems and Control*, vol. 5, pp. 1–10, 2018.

[119] B. Francis and G. Zames, "On h_∞-optimal sensitivity theory for SISO feedback systems," *IEEE Transactions on Automatic Control*, vol. 29, no. 1, pp. 9–16, 1984.

[120] R. de Rozario, A. J. Fleming, and T. Oomen, "Finite-time learning control using frequency response data with application to a nanopositioning stage," *IEEE/ASME Transactions on Mechatronics*, 2019.

[121] J. Dewey, K. Leang, and S. Devasia, "Experimental and theoretical results in output-trajectory redesign for flexible structures," *Journal of dynamic systems, measurement, and control*, vol. 120, no. 4, pp. 456–461, 1998.

[122] K. S. Ramani, M. Duan, C. E. Okwudire, and A. Galip Ulsoy, "Tracking Control of Linear Time-Invariant Nonminimum Phase Systems Using Filtered Basis Functions," *Journal of Dynamic Systems, Measurement, and Control*, vol. 139, no. 1, pp. 011001:1–11, 2017.

[123] J. van Zundert and T. Oomen, "On inversion-based approaches for feedforward and ILC," *Mechatronics*, vol. 50, pp. 282–291, 2018.

[124] S. Skogestad and I. Postlethwaite, *Multivariable feedback control: analysis and design*, vol. 2. Wiley New York, 2007.

[125] I. D. Landau, A. C. Silva, T.-B. Airimitoaie, G. Buche, and M. Noe, "An active vibration control system as a benchmark on adaptive regulation," in *2013 European Control Conference (ECC)*, pp. 2873–2878, IEEE, 2013.

[126] X. Chen and M. Tomizuka, "Selective model inversion and adaptive disturbance observer for time-varying vibration rejection on an active-suspension benchmark," *European Journal of Control*, vol. 19, no. 4, pp. 300–312, 2013.

[127] S. Berumen, F. Bechmann, S. Lindner, J.-P. Kruth, and T. Craeghs, "Quality control of laser- and powder bed-based Additive Manufacturing (AM) technologies," *Physics Procedia*, 2010.

[128] W. E. Frazier, "Metal additive manufacturing: A review," *J. Mater. Eng. Perform.*, vol. 23, no. 6, pp. 1917–1928, 2014.

[129] T. Atsumi and W. C. Messner, “Compensating for zoh-induced residual vibrations in head-positioning control of hard disk drives,” *IEEE/ASME Transactions on Mechatronics*, vol. 19, pp. 258–268, Feb. 2014.

[130] Q.-W. Jia, “Intersample ripple-free multirate control with application to a hard disk drive servo,” *IEEE/ASME Transactions on Mechatronics*, vol. 10, pp. 341–345, June 2005.

[131] J. Tani, S. Mishra, and J. T. Wen, “Identification of fast-rate systems using slow-rate image sensor measurements,” *IEEE/ASME Transactions on Mechatronics*, vol. 19, pp. 1343–1351, Aug. 2014.

[132] Y. C. Chang, B. Berry-Pusey, R. Yasin, N. Vu, B. Maraglia, A. X. Chatziioannou, and T. C. Tsao, “An automated mouse tail vascular access system by vision and pressure feedback,” *IEEE/ASME Transactions on Mechatronics*, vol. 20, pp. 1616–1623, Aug. 2015.

[133] Y. Yamamoto and P. Khargonekar, “Frequency response of sampled-data systems,” *IEEE Transactions on Automatic Control*, vol. 41, no. 2, pp. 166–176, 1996.

[134] M. Araki, Y. Ito, and T. Hagiwara, “Frequency response of sampled-data systems,” *Automatica*, vol. 32, no. 4, pp. 483–497, 1996.

[135] T. Hagiwara, M. Suyama, and M. Araki, “Upper and lower bounds of the frequency response gain of sampled-data systems,” *Automatica*, vol. 37, no. 9, pp. 1363–1370, 2001.

[136] Y. Yamamoto and M. Araki, “Frequency responses for sampled-data systems – their equivalence and relationships,” *Linear Algebra and its Applications*, vol. 205-206, pp. 1319–1339, 1994.

[137] G. C. Goodwin and M. Salgado, “Frequency domain sensitivity functions for continuous time systems under sampled data control,” *Automatica*, vol. 30, no. 8, pp. 1263–1270, 1994.

[138] J. S. Freudenberg, R. H. Middleton, and J. H. Braslavsky, “Inherent design limitations for linear sampled-data feedback systems,” *International Journal of Control*, vol. 61, no. 6, pp. 1387–1421, 1995.

[139] O. Lindgarde and B. Lennartson, “Performance and robust frequency response for multirate sampled-data systems,” in *American Control Conference, 1997. Proceedings of the 1997*, vol. 6, pp. 3877–3881, IEEE, 1997.

[140] M. W. Cantoni and K. Glover, “Frequency-domain analysis of linear periodic operators with application to sampled-data control design,” *Proceedings of IEEE Conference on Decision and Control*, vol. 5, pp. 4318–4323 vol.5, 1997.

[141] T. Oomen, M. van de Wal, and O. Bosgra, “Design framework for high-performance optimal sampled-data control with application to a wafer stage,” *International Journal of Control*, vol. 80, no. 6, pp. 919–934, 2007.

[142] O. Lindgärde, *Frequency analysis of sampled-data systems applied to a lime slaking process*. Chalmers University of Technology,, 1999.

[143] R. E. Kalman, Y. C. Ho, and K. S. Narendra, “Controllability of linear dynamical systems,” *Contributions to differential equations*, vol. 1, no. 2, pp. 189–213, 1963.

[144] B. A. Francis and T. Georgiou, “Stability theory for linear time-invariant plants with periodic digital controllers,” *IEEE Transactions on Automatic Control*, vol. 33, no. 9, pp. 820–832, 1988.

[145] R. Middleton and J. Freudenberg, “Non-pathological sampling for generalized sampled-data hold functions,” *Automatica*, vol. 31, no. 2, pp. 315–319, 1995.

[146] M. Hayes, *Statistical digital signal processing and modeling*. Wiley-India, 2009.

[147] K. J. Astrom and B. Wittenmark, *Computer-Controlled Systems: Theory and Design*. Upper Saddle River, N.J: Prentice Hall, 3 edition ed., Nov. 1996.

[148] A. Al Mamun, G. Guo, and C. Bi, *Hard disk drive: mechatronics and control*. CRC Press, Taylor & Francis Group, London, 2007.

[149] I. D. Landau, A. C. Silva, T.-B. Airimitoaie, G. Buche, and M. Noe, “Benchmark on adaptive regulation–rejection of unknown/time-varying multiple narrow band disturbances,” *European Journal of Control*, vol. 19, no. 4, pp. 237–252, 2013.

[150] X. Chen and H. Xiao, “Multirate forward-model disturbance observer for feedback regulation beyond Nyquist frequency,” *Systems & Control Letters*, vol. 94, pp. 181–188, Aug. 2016. Submitted.

[151] H. Fujioka and S. Hara, “Output regulation for sampled-data feedback control systems: Internal model principle and H_∞ servo controller synthesis,” *Journal of the Chinese Institute of Engineers*, vol. 33, pp. 335–346, Mar. 2011.

[152] T. Chen and B. A. Francis, “H_2-optimal sampled-data control,” *IEEE Transactions on Automatic Control*, vol. 36, pp. 387–397, Apr. 1991.

[153] R. Ravi, P. P. Khargonekar, K. D. Minto, and C. N. Nett, “Controller parametrization for time-varying multirate plants,” *Automatic Control, IEEE Transactions on*, vol. 35, pp. 1259–1262, Nov. 1990.

[154] S. Lall and G. Dullerud, “An LMI solution to the robust synthesis problem for multi-rate sampled-data systems,” *Automatica*, vol. 37, pp. 1909–1922, Dec. 2001.

[155] X. Jing and Z. Lang, *Frequency domain analysis and design of nonlinear systems based on Volterra series expansion: a parametric characteristic approach*. Springer, 2015.

[156] Z. Q. Lang, S. A. Billings, R. Yue, and J. Li, “Output frequency response function of nonlinear volterra systems,” *Automatica*, vol. 43, no. 5, pp. 805–816, 2007.

[157] Z. Xiao and X. Jing, “Frequency-domain analysis and design of linear feedback of nonlinear systems and applications in vehicle suspensions,” *IEEE/ASME transactions on mechatronics*, vol. 21, no. 1, pp. 506–517, 2016.

[158] I. S. Gradshtein, *Table of Integrals, Series, and Products*, vol. 1. Academic Press, Jan. 1980.

[159] E. C. Titchmarsh and D. R. Heath-Brown, *The theory of the Riemann zeta-function*. Oxford University Press, 1986.

[160] H. Edwards, *Riemann’s zeta function*. Pure and Applied Mathematics, Elsevier Science, 1974.

[161] J. Sondow and E. W. Weisstein, “Riemann zeta function.” From MathWorld–A Wolfram Web Resource.

Appendix A

A.1 Main MATLAB Commands in the Proposed Closed-loop Simulation

```
% Importing the COMSOL classes
import com.comsol.model.*
import com.comsol.model.util.*

% Open COMSOL mph file
model = mphopen('FEM_file_with_one_time_step');
ht = model.physics('ht');

% Compute FEM
model.study('std1').run;

% Get the whole temperature distribution
[x0, y0, T, tt] = mphinterp(model, {'x',…
   'y', 'T', 't'}, 'coord', coord, 't', t);

% Set tf to t0
time = mphglobal(model,'t','solnum','end');
model.param.set('t0', time);

% Set T(tf) to T(t0)
ht.feature('init1').set('T', 'T');
v1 = model.sol('sol1').feature('v1');
v1.set('initsol', 'sol1');

% Set q(tf) to q
model.param.set('laserpower', q);
```

A.2 Multirate Signal Processing

The downsampling operation in Fig. 6.7 gives

$$U_d(\mathrm{e}^{j\Omega T_s}) = \frac{1}{F}\sum_{k=0}^{F-1} U_{dh}(\mathrm{e}^{j(\Omega T_s' - \frac{2\pi k}{F})}). \tag{A.1}$$

From the upsampling operation, the Fourier transforms of y_d and y_{dh} are related by

$$Y_d(\mathrm{e}^{j\Omega T_s}) = Y_{dh}(\mathrm{e}^{j\Omega T_s'}). \tag{A.2}$$

Note that

$$C(\mathrm{e}^{j\Omega T_s}) = \frac{U_d(\mathrm{e}^{j\Omega T_s})}{Y_d(\mathrm{e}^{j\Omega T_s})},\ C_{dh}(\mathrm{e}^{j\Omega T_s'}) = \frac{U_{dh}(\mathrm{e}^{j\Omega T_s'})}{Y_{dh}(\mathrm{e}^{j\Omega T_s'})}, \tag{A.3}$$

and thus

$$\sum_{k=0}^{F-1} C_{dh}(\mathrm{e}^{j(\Omega T_s' - \frac{2\pi k}{F})}) = \sum_{k=0}^{F-1} \frac{U_{dh}(\mathrm{e}^{j(\Omega T_s' - \frac{2\pi k}{F})})}{Y_{dh}(\mathrm{e}^{j(\Omega T_s' - \frac{2\pi k}{F})})}. \tag{A.4}$$

The denominators of the terms on the right side of (A.4) satisfy

$$\begin{aligned} Y_{dh}(\mathrm{e}^{j(\Omega T_s' - \frac{2\pi k}{F})}) &= Y_{dh}(\mathrm{e}^{j(\Omega - \frac{2\pi k}{T_s})T_s'}) \\ = Y_d(\mathrm{e}^{j(\Omega - \frac{2\pi k}{T_s})T_s}) &= Y_d(\mathrm{e}^{j\Omega T_s}), \end{aligned} \tag{A.5}$$

where the second equal sign is due to the upsampling of (A.2). Substituting (A.5) and (A.1) into (A.4) gives

$$\begin{aligned} \sum_{k=0}^{F-1} C_{dh}(\mathrm{e}^{j(\Omega T_s' - \frac{2\pi k}{F})}) &= \frac{\sum_{k=0}^{F-1} U_{dh}(\mathrm{e}^{j(\Omega T_s' - \frac{2\pi k}{F})})}{Y_d(\mathrm{e}^{j\Omega T_s})} \\ &= \frac{F U_d(\mathrm{e}^{j\Omega T_s})}{Y_d(\mathrm{e}^{j\Omega T_s})}. \end{aligned} \tag{A.6}$$

Hence, according to (A.3),

$$\sum_{k=0}^{F-1} C_{dh}(\mathrm{e}^{j(\Omega T_s' - \frac{2\pi k}{F})}) = F C(\mathrm{e}^{j\Omega T_s}), \tag{A.7}$$

which is equivalent to (6.5).

A.3 Proof of Lemma 3 in Section 8.3.1

Proof. Recall $\mathscr{L}^{-1}\{P_c(s)/s\} = t^n/(n!)$ by the inverse Laplace transform. Thus, the ZOH equivalent of $P_c(s)$ is

$$P_d(z) = (1 - z^{-1})\mathscr{Z}\left\{\frac{(kT_s)^n}{n!}\right\} = \frac{T_s^n(1 - z^{-1})}{n!}\sum_{k=0}^{\infty} k^n z^{-k}. \tag{A.8}$$

We adopt two fundamental functions in number theory to evaluate $P_d(z)$ at $z = -1$. Notice that $\sum_{k=0}^{\infty} k^n(-1)^{-k} = -\eta(-n) = -(1 - 2^{1+n})\zeta(-n)$, where $\eta(n)$ is the Dirichlet Eta Function and $\zeta(n)$ is the Riemann Zeta Function [158] defined by

$$\zeta(n) \triangleq \begin{cases} \sum_{k=1}^{\infty} \frac{1}{k^n}, & \Re\{n\} > 1 \\ (1 - 2^{1-n})^{-1}\sum_{k=1}^{\infty} \frac{(-1)^{k-1}}{k^n}, & \Re\{n\} > 0 \end{cases}.$$

$\zeta(n)$ is furthermore extended to the whole complex plane by analytic continuation and satisfies the functional equation [159, 160, Chapter 2]

$$\zeta(-n) = 2^{-n}\pi^{-n-1}\sin\left(-\frac{\pi n}{2}\right)\overline{\Gamma}(1+n)\zeta(1+n), \tag{A.9}$$

where $\overline{\Gamma}(n)$ is the Gamma function and $n \in \mathbb{C}$. From the factor $\sin\left(-\frac{\pi n}{2}\right)$, $\zeta(-n)$ has zeros at all positive even integers of n (called the "trivial zeros"). Hence after substitution into (A.8), $P_d(-1) = 0$ when n is a positive even integer. By definition,

$$P_c(j(\Omega_o + \frac{2\pi}{T_s}k))H(j(\Omega_o + \frac{2\pi}{T_s}k)) = \frac{1 - \mathrm{e}^{-j(\Omega_o + \frac{2\pi}{T_s}k)T_s}}{j^{n+1}(\Omega_o + \frac{2\pi}{T_s}k)^{n+1}},$$

which is finite when $\Omega_o = \pi/T_s$. Hence Lemma 3 holds. □

Remark 6. *A numerical evaluation of the zeta function is available at [161]. The ZOH equivalents of* $1/s^n$ *for n up to 8 are numerically evaluated in [110]. There, a zero at* -1 *is evident for* $n = 2, 4, 6, 8$.

A.4 Proof of Lemma 5 in Section 8.3.3

Proof. Take an inertia system $P_c(s) = 1/s^2$ in motion control as example.[1] We show that $\mathscr{P}_h(\mathrm{e}^{j\cdot 0\cdot T_s'}) < 1$ and $\mathscr{P}_h(\mathrm{e}^{j\Omega_N T_s'}) > 1$. If PFG is a continuous function of Ω_o for $\Omega_o \in (0, \Omega_N)$, $\mathscr{P}_h(\mathrm{e}^{j\Omega_0 T_s'})$ then must cross over the 0 dB line at least once below the Nyquist frequency Ω_N. In other words, under the metric of PFG, it is inevitable that some band-limited disturbances below the Nyquist frequency are amplified by single-rate high-gain control.

With $P_c(s) = 1/s^2$, we have $P_d(z) = T_s^2(z+1)/\left[2(z-1)^2\right]$ and $P_{dh}(z) = T_s'^2(z+1)/\left[2(z-1)^2\right]$. When $\Omega_0 = 0$, (8.17) yields $\mathscr{P}_h(\mathrm{e}^{j\cdot 0\cdot T_s'}) = \sqrt{\left\|1 - \Gamma_0^*(0)\right\|^2 + \sum_{k=1}^{F-1}\left\|\Gamma_k^*(0)\right\|^2}$. Based on the definition in (8.16) as well as the expressions of $P_d(z)$ and $P_{dh}(z)$, we get $\Gamma_k^*(0) = 1$ when $k = 0$ (by applying L'Hospital's Rule twice), and $\Gamma_k^*(0) = 0$ when $k \neq 0$. Therefore, $\mathscr{P}_h(\mathrm{e}^{j\cdot 0\cdot T_s'}) = 0 (< 1)$.

Next consider the case of $\Omega_o = \Omega_N = \pi/T_s$. Evaluating the frequency responses of $P_d(z)$, $P_{dh}(z)$, and $H(z)$ in (8.14) yields

$$\Gamma_0^*(\Omega_N) = \frac{8\mathrm{e}^{j\pi/F}(\mathrm{e}^{j\pi/F} + 1)}{F^3[\mathrm{e}^{j\pi/F} - 1]^3(\mathrm{e}^{j\pi} + 1)}. \tag{A.10}$$

For $F \geqslant 2$, $\Gamma_0^*(\Omega_N) \to \infty$ since $\mathrm{e}^{j\pi} + 1 = 0$. Hence, in (8.17), $\mathscr{P}_h(\mathrm{e}^{j\Omega_N T_s'}) \to \infty > 1$.

---

[1] Without loss of generality, the gain of $P_c(s)$ is normalized to unity. Non-unity gains are canceled in the computation of $\Gamma_k(\Omega_o)$ and $\Gamma_k^*(\Omega_o)$ in (8.16).

With $\mathscr{P}_h(\mathrm{e}^{j\cdot 0\cdot T_s^{'}}) < 1$ and $\mathscr{P}_h(\mathrm{e}^{j\Omega_N T_s^{'}}) > 1$, we thus have $B_p < \Omega_N$ based on a continuity analysis. $\square$